Astronomy Letters, Vol. 26, No. 8, 2000, pp. 485–493. Translated from Pis'ma v Astronomicheskiĭ Zhurnal, Vol. 26, No. 8, 2000, pp. 563–573.

On the Large-Scale Structure of Galactic Disks

V. P. Reshetnikov*

Astronomical Institute, St. Petersburg State University, Bibliotechnaya pl. 2, Petrodvorets, 198904 Russia

Received December 23, 1999

Abstract—The disk positions for galaxies of various morphological and nuclear-activity types (normal galaxies, QSO, Sy, E/S0, low-surface-brightness galaxies, etc.) on the μ_0–h (central surface brightness–exponential disk scale) plane are considered. The stellar disks are shown to form a single sequence on this plane ($SB_0 = 10^{-0.4\mu_0} \propto h^{-1}$) over a wide range of surface brightnesses ($\mu_0(I) \approx 12$–25) and sizes ($h \approx 10$–100 kpc). The existence of this observed sequence can probably be explained by a combination of three factors: a disk-stability requirement, a limited total disk luminosity, and observational selection. The model by Mo *et al.* (1998) for disk formation in the CDM hierarchical-clustering scenario is shown to satisfactorily reproduce the salient features of the galaxy disk distribution on the μ_0–h plane. © *2000 MAIK "Nauka/Interperiodica".*

Key words: *galaxies, morphological types, active galactic nuclei, star formation*

1. INTRODUCTION

In recent years, semianalytical theories of galaxy formation have developed to a point where it has become possible to perform detailed computations of the main parameters of galaxies of various types (e.g., Kauffmann 1996; Dalcanton *et al.* 1997; Mo *et al.* 1998; Jimenez *et al.* 1998; Boissier and Prantzos 1999). Of special interest is the model suggested by Mo *et al.* (1998) (hereafter MMW). This model allows simple analytical formulas to be obtained for the main parameters of galaxy disks and their evolution with z to be estimated.

In this paper, we sum up the observational data on the integrated parameters of the disks of the galaxies of various types (normal galaxies, SyG, QSO, etc.) and compare them with the predictions of the MMW model.

2. DISK GALAXIES IN THE MMW MODEL

Mo *et al.* (1998) use the approach that is based on the CDM (Cold Dark Matter) scenario of galaxy formation (see, e.g., the review by Silk and Wyse, 1993). According to this scenario, nonbaryonic halos form from primordial fluctuations at the first stage. At the next stage, gas cools and condenses in these halos to form the disks of the galaxies that surround us.

Here are the main assumptions of the MMW model:

(1) The mass of the galaxy disk (M_d) is equal to a fixed fraction (m_d) of that of the surrounding dark halo (M), i.e., $M_d = m_d M$.

(2) The angular momentum of the disk (J_d) is also equal to a fixed fraction (j_d) of that of the halo: $(J) - J_d = j_d J$.

(3) Galaxy disks are thin, rotationally supported, and have exponential density distribution $\Sigma(r) = \Sigma_0 \exp(-r/h)$, where Σ_0 and h are the central disk surface density and exponential disk scale length, respectively.

(4) The disks of real galaxies are stable.

We can show, neglecting self-gravitation of the disk and assuming that the halo is an isothermal sphere, that (see MMW)

$$h = \frac{1}{10\sqrt{2}} \lambda V_c \frac{j_d}{m_d} \left(\frac{H(z)}{H_0}\right)^{-1}, \quad (1)$$

$$\Sigma_0 = \frac{10}{\pi G} m_d \lambda^{-2} V_c \left(\frac{m_d}{j_d}\right)^2 \frac{H(z)}{H_0}, \quad (2)$$

and

$$M_d = \frac{1}{10G} m_d V_c^3 \left(\frac{H(z)}{H_0}\right)^{-1}. \quad (3)$$

In formulas (1)–(3), λ is the dimensionless spin parameter defined in the standard way as $\lambda = JE^{1/2}G^{-1}M^{-5/2}$ (E is the total energy; G, the gravitational constant); V_c, the disk rotational velocity; H_0, the current Hubble constant; and $H(z)$, the Hubble constant at redshift z corresponding to the formation epoch of the dark matter of the halo where the disk was born. Naturally, $H(z)$ depends on the adopted cosmological model. Hereafter, all computations are made in terms of the flat cosmological model ($\Omega = 1$ and $\Omega_\Lambda = 0$) with $H_0 = 75$ km s^{-1} Mpc^{-1}. The result of the allowance for disk self-gravitation and the use of more realistic dark halo mass distributions is

* E-mail address for contacts: resh@astro.spbu.ru

a factor on the order of unity in the above formulas (MMW). Hereafter, we neglect this factor.

It follows from formulas (1) and (2) that the total disk luminosity is $L_d \propto \Sigma_0 h^2 \propto V_c^3$. The MMW model thus has a Tully–Fisher relation already incorporated into it [see a discussion in Mo *et al.* (1998) and Boissier and Prantzos (1999)].

According to Mo *et al.* (1998), the main properties of disk galaxies are fully determined by parameters λ, m_d, j_d, V_c, and $H(z)$. $H(z)$ increases with z, and, therefore, as is evident from formulas (1) and (2), the disks that formed at large z should be denser and more compact, other parameters being fixed. Higher λ must correspond to more extended and relatively more rarefied disks.

Other authors also have given analytical formulas for the parameters of disk galaxies. Thus, for example, Dalcanton *et al.* (1997) found that $h \propto \lambda M^{1/3}$ and $\Sigma_0 \propto \lambda^{-2(1+3F)} M^{1/3}$, where F is the baryonic mass fraction of the galaxy. For small F, the model of Dalcanton *et al.* (1997) implies a dependence of disk parameters on λ and M that is close to that implied by MMW. Similar relations were found even earlier by van der Kruit (1987). However, Mo *et al.* (1998) wrote these relations in a form that is more convenient to use in the analyses. Furthermore, the relations given by the latter authors include explicit dependence of disk parameters on the disk formation time.

We now analyze how the data on real galaxies of various types agree qualitatively and quantitatively with predictions of the model of Mo *et al.* (1998).

3. GALAXIES OF VARIOUS TYPES ON THE μ_0–h PLANE

3.1. Normal Galaxies

In his dissertation, Byun (1992) gives the results of a two-dimensional decomposition of the surface-brightness distributions for 1163 Southern-sky Sb–Sd spiral galaxies in the Kron–Cousins I band. Small circles in Fig. 1 show the distribution of the disks of these galaxies on the $\mu_0(I)$–h plane (here $\mu_0(I)$ is the central disk surface brightness of the disk in magnitudes per square arcsecond; and h, the exponential scale length in kpc assuming $H_0 = 75$ km s^{-1} Mpc^{-1}). Filled circles indicate the galaxy disks located within 15 Mpc from us. The latter subsample contains a larger fraction of galaxies with relatively small h, which can be naturally explained by observational selection (the sample of Byun (1992) is angular diameter-limited, because it contains only the galaxies with $d \geq 1\farcm7$).

The mean parameters of the galaxy sample considered are $\langle\mu_0(I)\rangle = 19.43 \pm 0.83(\sigma)$ (uncorrected for internal extinction within sample objects) and $\langle h\rangle = 3.9 \pm 1.8(\sigma)$ kpc. Adopting $B - I = +1.70$ for galaxy disks (de Jong 1996b), we obtain $\langle\mu_0(B)\rangle \approx 21.1$, which is somewhat brighter than the standard value of 21.65 (Freeman 1970) due to observational selection. Byun (1992) showed the galaxy distances in his sample to correlate with central disk brightness, i.e., the galaxies with higher μ_0 were selected predominantly among more distant objects. The mean $\mu_0(I)$ for the objects within 30 Mpc is 19.60 ± 1.00 (261 galaxies) and thus becomes closer to the standard Freedman's value.

Note also that the parameters of our own Galaxy, the Milky Way, are close to the corresponding mean values for Byun's (1992) sample of spiral galaxies. According to Sackett (1997), $h^{MW} = 3 \pm 1$ kpc. This result, combined with modern estimates of the surface brightness of the Milky Way in the solar vicinity (van der Kruit 1986; Kimeswenger *et al.* 1993), yields $\mu_0^{MW}(B) \approx 21$.

Evstigneeva and Reshetnikov (1999) suggested that the observed parameters of the disks of spiral galaxies obey the relation $SB_0 \propto h^{-1}$, where $SB_0 = 10^{-0.4\mu_0}$. The disk parameters from Byun (1992) do not show such a correlation. The linear correlation coefficient between $\mu_0(I)$ and $\log h$ for the entire sample (1163 galaxies) is equal to 0.06. However, if we restrict the sample to the objects located within 30 Mpc, the correlation coefficient increases to $\rho = 0.20$. Note also that the range of galaxy disk parameters in the sample by Byun (1992) is not too large (see Fig. 1). The dashed line in Fig. 1 shows the $SB_0 \propto h^{-1}$ relation for the data points corresponding to the mean parameters of the galaxies from Byun (1992). As is evident from Fig. 1, extremely compact nuclear stellar disks of elliptical galaxies, the disks of E/S0 galaxies, and very extended disks of giant low-surface brightness galaxies lie more or less along the relation mentioned above (see below).

The observed distribution of normal-galaxy disks on the μ_0–h plane can be explained in terms of simple hypotheses of observational selection and physical disk stability (see e.g., McGaugh 1998; van den Bosch 1998). The galaxy luminosity function falls off abruptly at high absolute luminosities: very luminous galaxies are extremely rare. Therefore, the upper limit of the total galaxy disk luminosity is the most natural constraint in Fig. 1. The thick solid line in Fig. 1 shows the locus of constant exponential disk luminosity provided that the total luminosity is $L_I = 10 L_I^*$. Here, L_I^* corresponds to the characteristic absolute magnitude of $M_I^* = -21.8$ in the galaxy luminosity function according to Marzke *et al.* (1998). It is evident from Fig. 1 that this straight line sets a reasonable upper limit for galaxy disks from Byun (1992).

The second natural constraint for galaxy disks in Fig. 1 is the angular diameter limitation. For exponential disks, we have $\mu(r) = \mu_0 + 1.086 r/h$ and, consequently, the limitation on diameters can be rewritten as $d \geq d_{lim} = 2r_{lim} = 1.842h\,(\mu_{lim} - \mu_0)$. The dotted curve in Fig. 1 shows the observational selection relation for a galaxy with $d_{lim} = 5$ kpc and $\mu_{lim}(I) = 23.3$ (this limiting

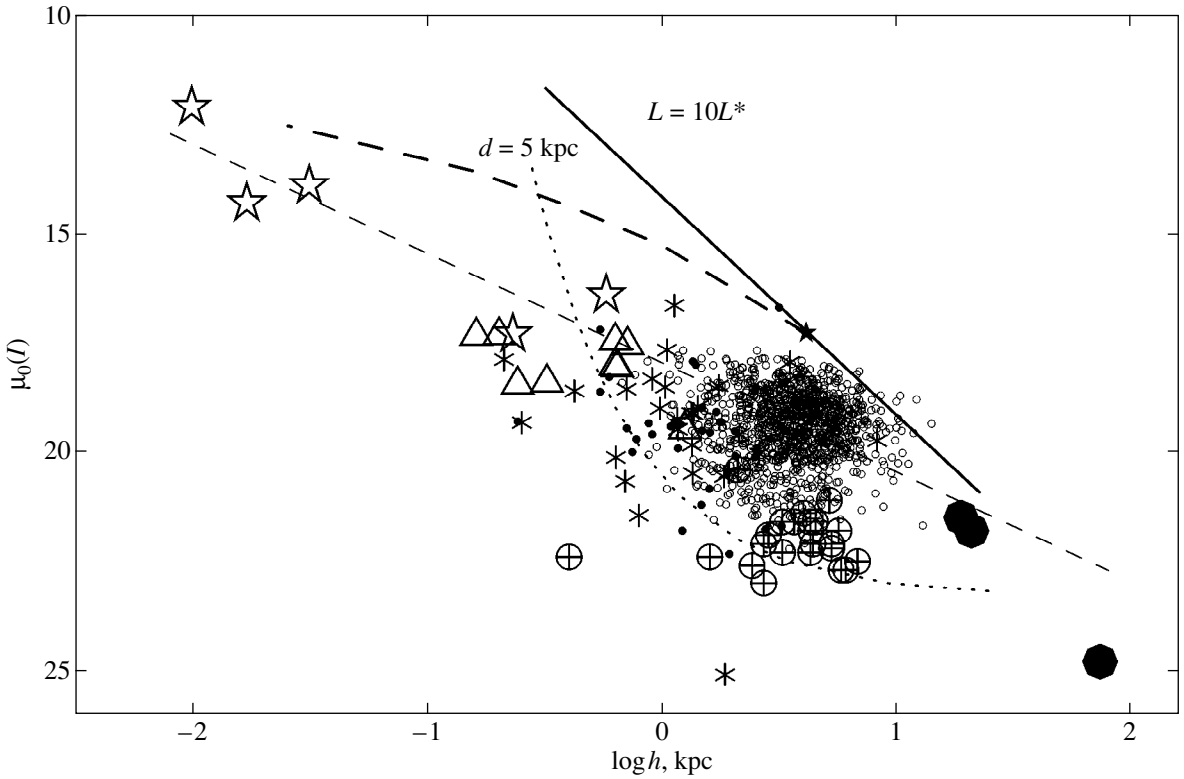

Fig. 1. The distribution of the exponential disks of galaxies of various types on the $\mu_0(I)$–h plane. Small circles show the data from Byun's (1992) thesis (filled circles are the galaxies with distances <15 Mpc); stars are compact nuclear disks of E/S0 galaxies; triangles and small asterisks are stellar disks in E/S0 galaxies; circles with crosses, low surface brightness galaxies; and big filled circles, giant low surface brightness galaxies (see text). The thick solid line shows the constant disk luminosity curve (provided that $L_d = 10L^*$); dotted line, the selection line for galaxies with a diameter of 5 kpc; dashed curve, the disk stability condition for the galaxies with a total luminosity of $10L^*$; and dashed line, the $SB_0 \propto h^{-1}$ relation (see text).

I-band isophote corresponds to $\mu_{lim}(B) = 25.0$ for $B - I = +1.70$). As is evident from Fig. 1, the galaxies from Byun (1992) are located in the $L_d \le 10L^*$ and $d \ge 5$ kpc domain on the μ_0–h plane. [An apparent magnitude selection produces a relation that is similar to that resulting from angular diameter selection (McGaugh, 1998).]

Another constraint for galaxy parameters in Fig. 1 follows from the bar instability of the disks of galaxies with spins below certain critical value λ_{crit}. (See a discussion in Mo *et al.* (1998) and van den Bosch (1998).) Following the approach suggested by van den Bosch (1998), we show on the constant-luminosity line in Fig. 1 the parameters of a disk with $L_d = 10L^*$ and $\lambda = \lambda_{crit} = 0.05$ (MMW) (asterisk). To be stable, more compact disks require a bulge. The thick dashed line in Fig. 1 is the locus where the conditions $L_d + L_b = 10L^*$ (here L_b is the luminosity of the galaxy bulge) and $\lambda = \lambda_{crit}$ are satisfied. The bulge-to-disk luminosity ratio varies along this curve from 0 (asterisk) to $+\infty$. (Note that the exact position of this dashed line depends on the adopted cosmological model and the galaxy formation redshift, z_f. We adopt $z_f = 0$ in our illustrative calculations).

It can be easily seen from Fig. 1 that the stability condition combined with luminosity constraint ($L_d \le 10L^*$) determines a domain with an upper limit given approximately by straight line $SB_0 \propto h^{-1}$ on the μ_0–h plane.

3.2. Galaxies with Active Nuclei and Starburst Galaxies

The thick cross in Fig. 2 marked by letter Q shows the mean disk parameters for 10 relatively nearby quasars (with redshifts $z \approx 0.2$) as inferred from the data published by Bahcall *et al.* (1997)[1]. (We considered only the quasars whose two-dimensional surface brightness distributions can be better fitted by the exponential rather than the deVaucouleurs law.) The central disk surface brightness of the QSO sample objects is somewhat higher (by $\approx 0^m.6$–$0^m.7$) than that of normal galaxies from Byun (1992). However, as is evident from Fig. 2, this discrepancy is within the scatter of disk parameters for normal galaxies.

Crosses S and SS in Fig. 2 show the mean parameters for the Seyfert galaxy sample according to Afanas'ev *et al.* (1997) and for the sample of galaxies with Seyfert and starburst nuclei according to Hunt

[1] Hereafter we assume $B - I = +1.7$ and $V - I = +1.0$ in all transformations between photometric bands

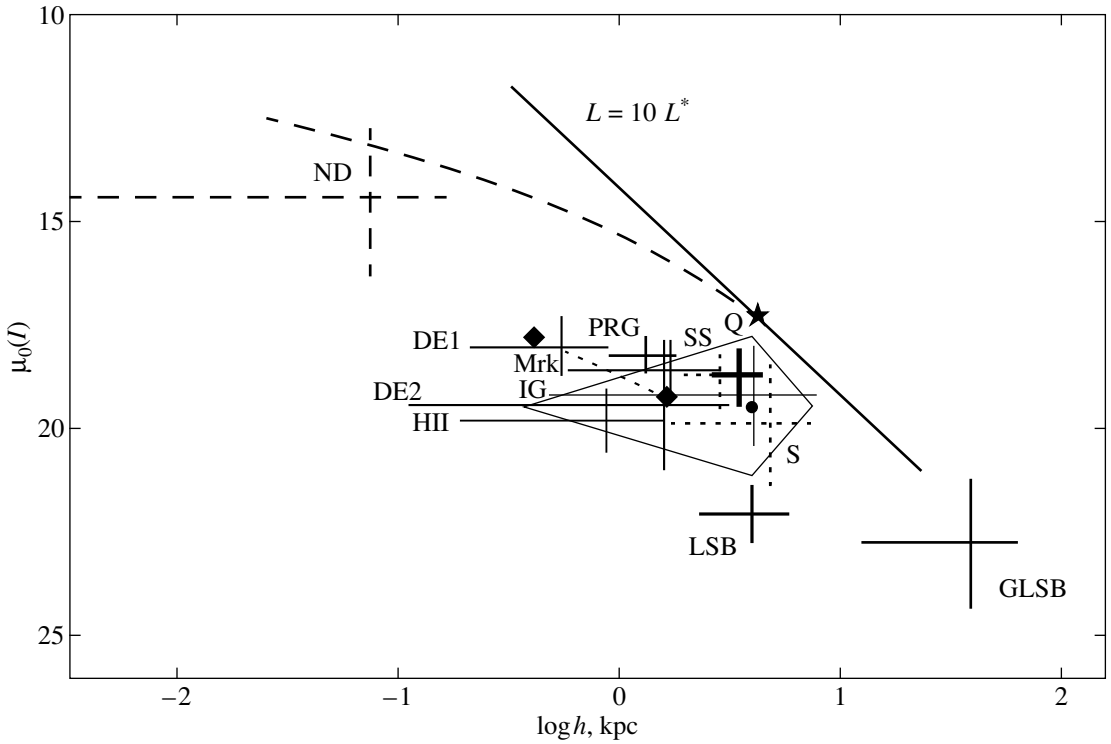

Fig. 2. Stellar disks of galaxies of various types on the $\mu_0(I)$–h plane (see text). The dark dot indicates the mean parameters of spiral galaxies from Byun's (1992) thesis, and the quadrangle of the segments of solid lines shows the $\pm 2\sigma$ box of the mean values. The curves have the same meaning as in Fig. 1.

et al. (1999), respectively. (We transformed the data taken from Hunt *et al.* (1999) into the *I* band assuming $I - K = +1.8$.) The mean disk parameters for both samples resemble those of normal galaxies, although, as was pointed out by Hunt *et al.* (1999), the disks of Seyfert-I galaxies are relatively compact and have abnormally high μ_0.

The starburst galaxies from Chitre and Joshi (1999) (all 10 objects are Markarian galaxies; therefore, their parameters are marked by Mrk in Fig. 2) have more compact and brighter disks compared to the common Sb–Sd galaxies. However, the objects from Chitre and Joshi (1999) are mainly early-type galaxies whose disk parameters are known to be shifted in just this direction (see, e.g., de Jong 1996a).

Dwarf starburst galaxies (HII in Fig. 2) from Telles and Terlevich (1997) have relatively low central surface brightness compared to other galaxies of similar size. This corroborates the conclusion by Telles and Terlevich (1997) that HII galaxies are similar to low-surface-brightness galaxies (see Section 3.6).

3.3. Interacting Galaxies

The parameters of interacting galaxies from Evstigneeva and Reshetnikov (1999) (IG in Fig. 2) resemble very much those of normal galaxies as inferred by Byun (1992). However, the mean *B*-band μ_0 for the disks of interacting galaxies is about 1^m brighter than that of isolated objects (Evstigneeva and Reshetnikov, 1999). The absence of such a large difference between the μ_0 values in the *I* band is consistent with the assumption that high surface brightness of interacting disks is due to enhanced star formation. On the other hand, as was shown in Section 3.1, the sample of Byun (1992) is distorted by observational selection, which somewhat shifts the mean μ_0 toward higher values. Observational selection taken into account, the central disk surface brightness of normal galaxies differs from that of interacting galaxies by $\Delta\mu_0(I) \approx 0\overset{m}{.}5$.

Polar-ring galaxies (PRG) from Reshetnikov *et al.* (1994) have relatively compact and bright stellar disks. This can be due both to the real mass redistribution in strong interaction, accompanied by the formation of a polar structure, and to observational selection. (A polar ring lives much longer around a short disk than around an extended one.)

In Fig. 2, diamond signs connected by a dashed line show the parameters of two stellar disks of the Sa-type galaxy NGC 3593 (Bertola *et al.* 1996). The smaller of these disks rotates in the direction opposite that of the larger disks and of the galaxy as a whole. The counter-rotating disk must have formed as a result of slow gas accretion from the intergalactic space onto the gas-free spiral galaxy (Bertola *et al.* 1996). The subsequent star formation in the captured gas must have resulted in the

formation of a counterrotating stellar disk. Interestingly, the parameters of this "secondary" disk are close to those of the disks in E/S0 galaxies from Scorza and Bender (1995).

3.4. Elliptical Galaxies and Galaxies with Stellar Disks

In Figs. 1 and 2, stellar disks of nine E/S0 galaxies from Scorza and Bender (1995) (DE1, triangles) and 28 E/S0 galaxies from Scorza *et al.* (1998) (asterisk) lie approximately along the $SB_0 \propto h^{-1}$ relation slightly shifted toward lower surface brightness values (or lower h).

Large asterisks in Fig. 1 and the dashed cross (ND) in Fig. 2 show the parameters of compact stellar disks in the nuclei of E/S0 galaxies according to Scorza and Bender (1990), Kormendy *et al.* (1996), and Scorza and van den Bosch (1998). As is evident from Figs. 1 and 2, compact nuclear disks lie along the same continuous sequence on the μ_0–h plane as stellar disks of early-type galaxies and those of spiral galaxies. The location of these disks on the plane considered agrees with the constraint implied by stability considerations—see Section 3.1 (dotted line). It can be assumed that early-type galaxies may contain disks with high μ_0 (they must fill the lower left corner in Figs. 1 and 2); however, they are difficult to identify against the bright E/S0 galaxy background.

3.5. Low Surface Brightness Galaxies

Low-surface-brightness galaxies from de Blok and McGaugh (1997) (crossed circles and LSB-marked cross in Figs. 1 and 2, respectively) have substantially lower surface brightnesses and the sizes that are comparable to those of normal galaxies. Giant low surface brightness galaxies (large filled circles in Fig. 1 and GLSB in Fig. 2) have colossal sizes with exponential disk scale lengths on the order of several tens of kpc (Bothun *et al.* 1987, 1990; Sprayberry *et al.* 1993). "Extreme" stellar disks (ultracompact nuclear stellar disks and GSLB galaxies) approximately follow the $SB_0 \propto h^{-1}$ relation.

Low surface brightness galaxies usually cannot be found in common galaxy catalogs. Such galaxies are usually searched for using special observing equipment, and many such objects still remain undiscovered even in the part of the nearby part of the Universe (see, e.g., Sprayberry *et al.* 1997). Future surveys are expected to yield new LSB galaxies to fill the lower right corners in Figs. 1 and 2.

3.6. Main Observational Conclusions

The disks of real galaxies of various types span a very large range of surface brightnesses ($\mu_0(I) \approx 12$–25) and sizes ($h \approx 10$ pc–100 kpc) in the μ_0–h plane, where they form a continuous sequence. The bulge to disk luminosity ratio (B/D) varies systematically along this sequence from $\gg 10$ for ellipticals located at the top left corner in Figs. 1 and 2 to ~0 for spiral galaxies located at the bottom right corner in the same figures. The effective bulge radius, r_e, to the disk scale length, h, ratio varies from $r_e/h \sim 0.1$ for giant low surface brightness galaxies at the bottom right corner in Figs. 1 and 2 to $r_e/h \geq 5$–10 for stellar disks in E/S0 galaxies. μ_0 and h also vary along the same sequence: the disks of galaxies with higher B/D ratios are, on the average, brighter and more compact.

The disks of quasars, Seyfert galaxies, and galaxies in interacting systems might have somewhat higher-than-average μ_0 values, due possibly to an increased star-formation rate and real mass redistribution in such galaxies. Note, however, that one should be very careful when concluding that the parameters of the disks of the galaxies of a certain type differ from those of "normal" galaxies because of selection effects that are difficult to assess. (The samples compared must satisfy similar apparent magnitude and angular size limitations and have similar B/D.) Furthermore, the structure of the disks can differ systematically in the regions with different space density of galaxies (Moore *et al.* 1998). On the whole, as is evident from Figs. 2 and 3, the parameters of the disks of galaxies of various morphological and activity types agree with those of the disks of normal galaxies, which are here represented by the objects from Byun's (1992) thesis. The compact stellar disks in the nuclei of E/S0 galaxies and low surface brightness galaxies have parameters that differ most from those of normal galaxies.

The observed positions of galaxies on the μ_0–h plane are determined by the disk stability condition, the total disk luminosity constraint ($L_d \leq 10L^*$), and observational selection. A combination of these three conditions (and, perhaps, other unknown factors) results in the alignment of galaxy-disk parameters along the empirical $SB_0 \propto h^{-1}$ relation (see Figs. 1–3). Deeper (in terms of surface brightness) stellar disk surveys are likely to "blur" this observational relation (see, e.g., Fig. 4 in Dalcanton *et al.* 1997), which, however, should survive in the form of the upper envelope of galaxy parameter distribution.

4. THE MO *et al.* (1998) MODEL AND REAL GALAXIES

4.1. The Milky Way

The integrated properties of disk galaxies in the Mo *et al.* (1998) model depend on a number of parameters (see Section 2)—λ, m_d, j_d, V_c, and redshift, z_f,—of the dark halo (disk) formation. We now estimate the time scale of the Milky Way disk formation in terms of the model of Mo *et al.* (1998) using realistic parameter values. We adopt $\lambda = 0.05$ and $m_d = j_d = 0.05$ (MMW) as standard values. Then, assuming for the Milky Way disk $h^{MW} = 3$ kpc; $\mu_0^{MW}(B) \approx 21$, $V_c^{MW} = 200$ km s^{-1}, and

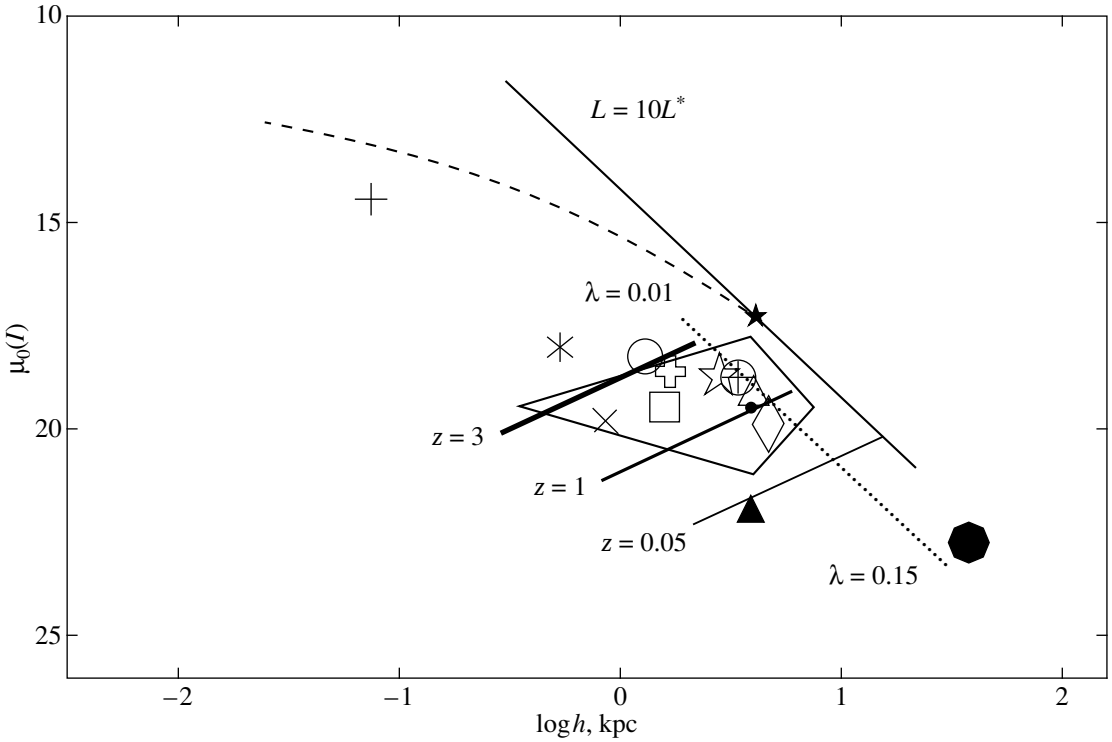

Fig. 3. Stellar disks of galaxies of various types on the $\mu_0(I)$–h plane. The line segments of different thickness show disks loci implied by MMW models (Mo *et al.* 1998) with different formation redshifts (0.05, 1, and 3). Different symbols show the mean parameters of galaxies of various types (see Fig. 2 and text). The curves and the quadrangle have the same meaning as in Figs. 1 and 2.

$M_d^{MW} = 6 \times 10^{10} M_\odot$ (see Section 3.1; Reshetnikov 2000), we obtain from formulas (1)–(3) that $H(z)/H_0 \approx 3$ (adopting a $M_d/L_d(I) = 1.7$ mass-luminosity ratio for the disk). It follows from this that $z_f \approx 1$ for $\Omega = 1$ and $\Omega_\Lambda = 0$ (see Fig. 1 in Mo *et al.* 1998). The model of Mo *et al.* (1998) therefore yields self-consistent parameter estimates for the Milky Way disk and its formation epoch ($z_f \approx 1$). Note also that the $m_d = 0.05$ value adopted above yields a plausible dark halo mass estimate for the Milky Way, $M = M_d/m_d = 1.2 \times 10^{12} M_\odot$ (see, e.g., the review by Zaritsky 1998). Note, however, that the dynamical analysis of the Galactic companions, the Galaxy + M31 system, etc, imply a larger size (~200 kpc) and dark-halo mass ($>10^{12} M_\odot$) for our Galaxy. Local observations provide no evidence for considerable dark mass within the optical disk of the Milky Way (e.g., Kuijken and Gilmore 1991; Creze *et al.* 1998).

The formation epoch of the Milky Way disk is by no means a very well defined quantity, because the process spanned a long time interval comparable to the Hubble time (see, e.g., Chiappini *et al.* 1997). Therefore, the epoch implied by z_f should be considered only a characteristic formation age. Redshift $z_f \approx 1$ approximately corresponds to the maximum star formation rate in the Universe (Baugh *et al.* 1998).

4.2. Normal Galaxies

Different symbols in Fig. 3 show the mean parameters of the galaxy samples described in Section 3 (errors are not shown in order not to encumber the figure). Stellar disks can be seen to concentrate conspicuously to the $SB_0 \propto h^{-1}$ relation. Furthermore, the mean parameters of stellar disks of galaxies of various types are mainly concentrated on the μ_0–h plane inside or in the vicinity of the rectangular box corresponding to normal galaxies (except compact nuclear disks and GLSB galaxies).

In Fig. 3, straight-line segments of various thickness show the parameters of stellar galaxy disks in the model of Mo *et al.* (1998) for three formation redshifts z_f = 0.05, 1, and 3. We adopted $\lambda = 0.05$ and $m_d = j_d = 0.05$. The adopted spin parameter approximately corresponds to the peak of λ distribution obtained in numerical simulations (e.g., Warren *et al.* 1992) and is close to the critical value that separates stable disks from unstable ones (Mo *et al.* 1998; van den Bosch 1998). Adopting $m_d = 0.05$ yields reasonable dark halo mass estimates in galaxies (see Section 4.1). We assumed the j_d/m_d ratio to be equal to unity, which is a standard, albeit not entirely substantiated, assumption in galaxy formation models (MMW). The disk rotation velocity varies along each segment from $V_c = 50$ km s^{-1} (left end) to $V_c = 350$ km s^{-1} (right end).

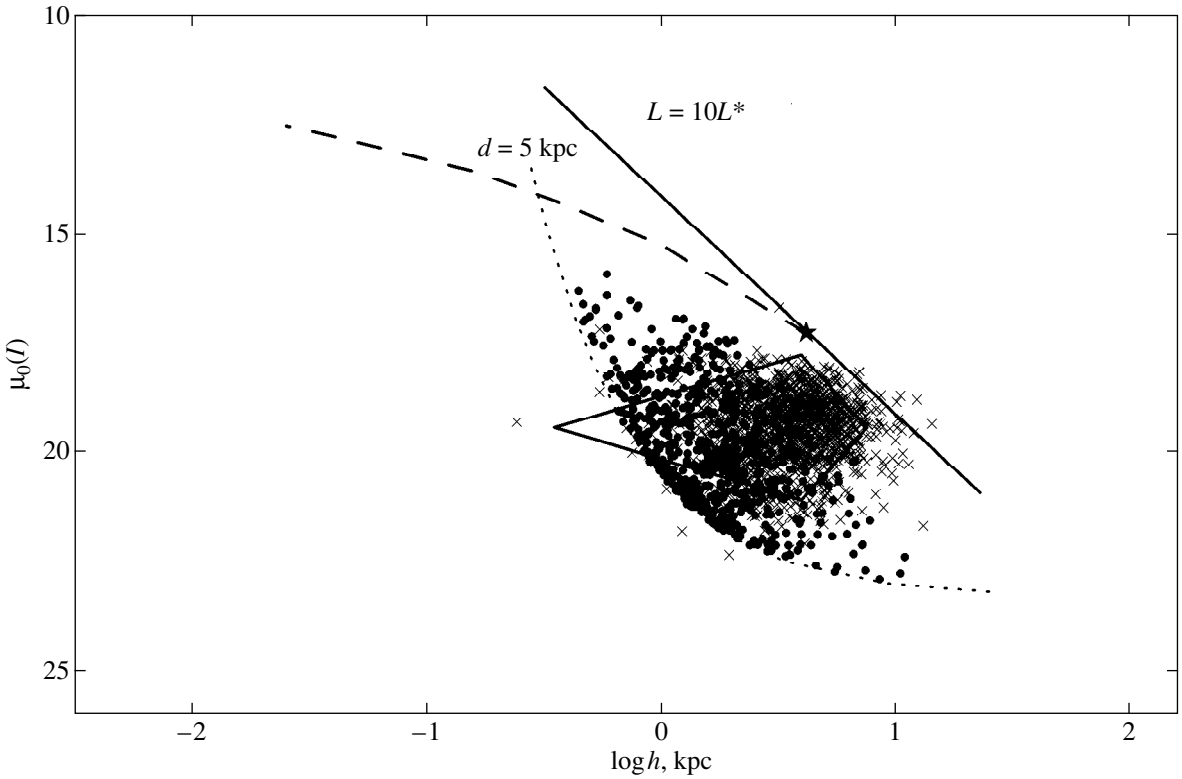

Fig. 4. Stellar disks of galaxies of various types on the $\mu_0(I)$–h plane. Crosses show the data for galaxies from Byun's (1992) thesis; dark dots, the parameters of simulated galaxies based on the MMW model (Mo *et al.* 1998). The curves and the rectangle have the same meaning as in Figs. 1 and 2.

As is evident from Fig. 3, the MMW model explains satisfactorily both the position and scatter of observed galaxy disks on the μ_0–h plane. The data on normal spiral galaxies similar to the Milky Way are consistent with $z_f \sim 1$. The disks of earlier-type galaxies (*c*) have larger formation times ($z_f > 1$). The parameters of low-surface-brightness galaxies are consistent with $z_f < 1$.These estimates seem to be quite plausible if z_f is considered to be the redshift of the last global star formation burst in the disk.

The dotted line in Fig. 3 shows how the parameters of the disks with $m_d = j_d = 0.05$; $V_c = 200$ km s^{-1}, and $z_f = 0$ vary as spin parameter λ changes from 0.01 to 0.15. It is evident from Fig. 3 that the MMW model implies that the disks of low surface brightness galaxies are relatively "young" (i.e., unevolved) and have larger λ. This conclusion is consistent with modern theories of the objects of the type considered (e.g., Dalcanton *et al.* 1997; Jimenez *et al.* 1998).

As is evident from formulas (1)–(2), the galaxy disks must approximately obey relations $\mu_0 \propto -2.5 \log V_c$ and $\log h \propto \log V_c$ (with fixed λ, m_d, j_d, and z_f). The data for spiral galaxies from Byun (1992) yield similar empirical relations: $\mu_0 \propto -2.72 \log V_c$ ($\rho = -0.58$) and $\log h \propto 0.70 \log V_c$ ($\rho = +0.59$). It was shown in Section 2 that the MMW model implies a Tully–Fisher relation in the form $L_d \propto V_c^3$. Spiral galaxies from the thesis by Byun (1992) follow relation $L_I \propto V_c^{2.72 \pm 0.04}$ ($\rho = 0.90$).

In order to compare graphically the model with observational data, we generated a catalog of 1200 "fictitious" galaxies based on formulas (1)–(2). In our computations, we assumed that the spin parameter λ has a log-normal distribution with $\langle\lambda\rangle = 0.05$ and $\sigma_\lambda = 0.7$ [obtained by analytically fitting the results of numerical simulations by Warren *et al.* (1992)], V_c follows a generalized Schechter distribution function with $n = 3$; $\beta = -1.0$, and $V_* = 250$ km s^{-1} (see Gonzalez *et al.* 1999). We further assumed that z_f follows a Gaussian distribution function with $\langle z_f\rangle = 1$, $\sigma_{z_f} = 0.3$, and $m_d = j_d = 1$. In Fig. 4, we compare the parameter distributions of 705 simulated galaxies (we left only the objects with $d \geq 5$ kpc) with the corresponding distributions for the galaxies from Byun (1992). As is evident from the figure, both distributions occupy approximately the same domain on the μ_0–h plane. Note only a somewhat larger fractions of simulated galaxies with high and low central surface brightness μ_0 compared to the corresponding fractions for real galaxies. This effect can be easily interpreted in terms of observational selection—the sample of Byun (1992) contains few low-surface brightness galaxies (they are searched for using special

observational techniques) and no galaxies of early morphological subtypes. The mean parameters of the simulated galaxy sample shown in Fig. 4 ($\mu_0 = 19.9 \pm 1.3$ and $\langle h \rangle = 2.0 \pm 1.3$ kpc) agree, within the error limits, with those of the real galaxy sample from Byun *et al.* (1992). Note also that simulated galaxies follow the Freeman law (Freeman 1970) very closely.

The properties of compact stellar disks in early-type galaxies can be reproduced with small spin parameter $\lambda \sim 0.01$ and large formation times $z_f \geq 3$. However, in the galaxies with the bulge-dominated mass contribution, the disk formation mechanism is likely to differ from the standard MMW scenario. The formation of disks in such galaxies can be due, e.g., to external accretion or merging, mass loss by bulge stars, and minibar disruption, etc. (Scorza and van den Bosch, 1998; van den Bosch, 1998).

4.3. Distant Galaxies

We have shown above that the global disk parameters of local spiral galaxies of various types are consistent with the predictions of the MMW model. The disks of distant galaxies that have formed long ago must be more compact and have higher surface brightnesses (MMW). Modern observational data on the photometric structure of extremely distant galaxies are, on the whole, consistent with this hypothesis.

The disks of three galaxies with $z > 5$ [HDF 4–473.0 at $z = 5.60$ according to Weymann *et al.* (1998) and the double galaxy HDF 3–951.1/2 at $z = 5.34$ according to Spinrad *et al.* (1998)] have a mean exponential scale length of $\langle h \rangle = 0.8 \pm 0.3$ kpc. The MMW model with $\lambda = 0.05$, $m_d = j_d = 0.05$, $V_c = 200$ km s^{-1}, and $z_f = 5$ implies $h \sim 0.6$ kpc.

The mean scale length for six galaxies located at $z \approx 3$ (Steidel *et al.* 1996; Giavalisco *et al.* 1996) is equal to 1.5 ± 0.8 kpc, which is comparable to the estimate implied by MMW (~1.2 kpc). The galaxies located at $z \approx 3$ have very high central surface brightnesses (in the rest frame) of $\mu_0(B) \sim 17.7$–18.7 (Steidel *et al.* 1996), which are about $\Delta\mu_0 = 2^m$ higher than those implied by the MMW model. This discrepancy might be due to the fact that, in the studies of distant objects, the galaxies with relatively high surface brightnesses (e.g., as a result of the ongoing star formation) are identified predominantly.

We can conclude that the MMW model is consistent with observational data on the structure of galaxies at $z \geq 3$. According to Mao *et al.* (1998), the model is also consistent with the data on the evolution of the exponential scale length h at $z \leq 1 : h \propto (1 + z)^{-1}$.

5. CONCLUSION

We have analyzed the parameters of stellar disks in galaxies of various types and their distribution on the μ_0–h plane. Simple scale considerations in the CDM scenario-based disk formation model (non-self-gravitating disks embedded in isothermal dark halos—Mo *et al.* 1998) proved to satisfactorily describe both qualitatively and quantitatively the disk parameters of real galaxies and their scatter on the μ_0–h diagram.

In recent times, this model has often served as the basis to study various aspects of the disk galaxy formation and evolution (see, e.g., Jimenez *et al.* 1998; Boissier and Prantzos 1999; van den Bosch 1999). The fact that the estimates given by this model are consistent with observational data is really remarkable, because the approach used by Mo *et al.* (1998) ignores such important processes affecting galaxy parameters as star formation and feedback, external accretion and mergers.[2] It spite of its simplicity, the model of Mo *et al.* (1998) must reflect (statistically, i.e., in the average) some of the important factors affecting the integrated properties of the spiral galaxies in the Milky Way vicinity (see Section 2).

A serious problem of the model of Mo *et al.* (1998) (and of the CDM scenario in general) is that it overestimates the dark matter contribution inside galaxies. The mass distributions of MMW models are dark halos dominated even in the inner parts of the galaxies (Springel and White 1999), which is inconsistent with observational data for normal spirals (e.g., for the Milky Way, see Section 4.1) and agrees only with observations of low-surface-brightness galaxies. Because of the too high dark mass fraction, the CDM scenario fails to explain the zero point of the Tully–Fisher relation (see a discussion in Steinmetz and Navarro 1999). These problems must eventually result in a modification of the model of Mo *et al.* (1998).

ACKNOWLEDGMENTS

I am grateful to N.Ya. Sotnikova (St. Petersburg State University) for her valuable comments. The work was supported by the Integration Program (project no. 578), the Competitive Center for Fundamental Science of the Ministry of General and Professional Education, and the Russian Foundation for Basic Research (project no. 98-02-18178).

REFERENCES

1. V. L. Afanas'ev, A. N. Burenkov, V. P. Mikhaĭlov, and A. I. Shapovalova, Preprint No. 130, Spets. Astrofiz. Obs. (Special Astrophysical Observatory, Russian Academy of Sciences, 1997).
2. J. N. Bahcall, S. Kirhakos, D. H. Saxe, and D. P. Schneider, Astrophys. J. **479**, 642 (1997).
3. C. M. Baugh, S. Cole, C. S. Frenk, and C. G. Lacey, Astrophys. J. **498**, 504 (1998).
4. F. Bertola, P. Cinzano, E. M. Corsini, *et al.*, Astrophys. J. Lett. **458**, L67 (1996).

[2] The effect of interactions and mergers on the structure of galaxy disks becomes considerably weaker if a later disk formation epoch of $z_f \leq 1$ is assumed (Weil *et al.* 1998)

5. S. Boissier and N. Prantzos, astro-ph/9909120 (1999).
6. G. D. Bothun, C. D. Impey, D. F. Malin, and J. R. Mould, Astron. J. **94**, 23 (1987).
7. G. D. Bothun, J. M. Schombert, C. D. Impey, and S. E. Schneider, Astrophys. J. **360**, 427 (1990).
8. Y.-I. Byun, *Dust Opacity and Structure of Spiral Galaxies*, PhD Thesis (Austral. Nation. Univers., Canberra, 1992).
9. C. Chiappini, F. Matteucci, and R. Gratton, Astrophys. J. **477**, 765 (1997).
10. A. Chitre and U. C. Joshi, astro-ph/9907253 (1999).
11. M. Creze, E. Chereul, O. Bienayme, and C. Pichon, Astron. Astrophys. **329**, 920 (1998).
12. J. J. Dalcanton, D. N. Spergel, and F. J. Summers, Astrophys. J. **482**, 659 (1997).
13. W. J. G. de Blok and S. S. McGaugh, Mon. Not. R. Astron. Soc. **290**, 533 (1997).
14. R. S. de Jong, Astron. Astrophys. **313**, 45 (1996a).
15. R. S. de Jong, Astron. Astrophys. **313**, 377 (1996b).
16. E. A. Evstigneeva and V. P. Reshetnikov, Pis'ma Astron. Zh. **25**, 673 (1999) [Astron. Lett. **25**, 582 (1999)].
17. K. C. Freeman, Astrophys. J. **160**, 811 (1970).
18. M. Giavalisco, C. C. Steidel, and F. D. Macchetto, Astrophys. J. **470**, 189 (1996).
19. A. H. González, K. A. Williams, J. S. Bullock, *et al.*, astro-ph/9908075 (1999).
20. L. K. Hunt, M. A. Malkan, G. Moriondo, and M. Salvati, Astrophys. J. **510**, 637 (1999).
21. R. Jiménez, P. Radoan, F. Matteucci, and A. F. Heavens, Mon. Not. R. Astron. Soc. **299**, 123 (1998).
22. G. Kauffmann, Mon. Not. R. Astron. Soc. **281**, 475 (1996).
23. S. Kimeswenger, B. Hoffman, W. Schlosser, and Th. Schmidt-Kaler, Astron. Astrophys., Suppl. Ser. **97**, 517 (1993).
24. J. Kormendy, Astrophys. J. Lett. **459**, L57 (1996).
25. K. Kuijken and G. Gilmore, Astrophys. J. Lett. **367**, L9 (1991).
26. S. Mao, H. J. Mo, and S. D. M. White, Mon. Not. R. Astron. Soc. **297**, L71 (1998).
27. R. O. Marzke, L. N. da Costa, P. S. Pellegrini, *et al.*, Astrophys. J. **503**, 617 (1998).
28. S. McGaugh, astro-ph/9810363 (1998).
29. H. J. Mo, S. Mao, and S. D. M. White, Mon. Not. R. Astron. Soc. **295**, 319 (1998).
30. B. Moore, G. Lake, and N. Katz, Astrophys. J. **495**, 139 (1998).
31. V. P. Reshetnikov, Astrofizika (2000) (in press).
32. V. P. Reshetnikov, V. A. Hagen-Thorn, and V. A. Yakovleva, Astron. Astrophys. **290**, 693 (1994).
33. P. D. Sackett, Astrophys. J. **483**, 103 (1997).
34. C. Scorza and R. Bender, Astron. Astrophys. **235**, 49 (1990).
35. C. Scorza and R. Bender, Astron. Astrophys. **293**, 20 (1995).
36. C. Scorza, R. Bender, C. Winkelmann, *et al.*, Astron. Astrophys., Suppl. Ser. **131**, 265 (1998).
37. C. Scorza and F. C. van den Bosch, Mon. Not. R. Astron. Soc. **300**, 469 (1998).
38. J. Silk and R. F. G. Wyse, Phys. Rep. **231**, 294 (1993).
39. H. Spinrad, D. Stern, A. Bunker, *et al.*, Astron. J. **116**, 2617 (1998).
40. D. Sprayberry, C. D. Impey, M. J. Irwin, *et al.*, Astrophys. J. **417**, 114 (1993).
41. D. Sprayberry, C. D. Impey, M. J. Irwin, and G. D. Bothun, Astrophys. J. **481**, 104 (1997).
42. V. Springel and S. D. M. White, Mon. Not. R. Astron. Soc. **307**, 162 (1999).
43. C. C. Steidel, M. Giavalisco, M. Dickinson, and K. L. Adelberger, Astron. J. **112**, 352 (1996).
44. M. Steinmetz and J. Navarro, astro-ph/9910573 (1999).
45. E. Telles and R. Terlevich, Mon. Not. R. Astron. Soc. **286**, 183 (1997).
46. F. C. van den Bosch, Astrophys. J. **507**, 601 (1998).
47. F. C. van den Bosch, astro-ph/9909298 (1999).
48. P. C. van der Kruit, Astron. Astrophys. **157**, 230 (1986).
49. P. C. van der Kruit, Astron. Astrophys. **173**, 59 (1987).
50. M. S. Warren, P. J. Quinn, J. K. Salmon, and W. H. Zurek, Astrophys. J. **399**, 405 (1992).
51. M. L. Weil, V. R. Eke, and G. Efstathiou, Mon. Not. R. Astron. Soc. **300**, 773 (1998).
52. R. J. Weymann, D. Stern, A. Bunker, *et al.*, Astrophys. J. Lett. **505**, L95 (1998).
53. D. Zaritsky, astro-ph/9810069 (1998).

Translated by A. Dambis

Astronomy Letters, Vol. 26, No. 8, 2000, pp. 494–499. Translated from Pis'ma v Astronomicheskiĭ Zhurnal, Vol. 26, No. 8, 2000, pp. 574–580.

Asymmetry of Compton Scattering by Relativistic Electrons with an Isotropic Velocity Distribution: Astrophysical Implications

S. Yu. Sazonov[1]* and R. A. Sunyaev[2]

[1] *Space Research Institute, Russian Academy of Sciences, Profsoyuznaya ul. 84/32, Moscow, 117810 Russia*
[2] *Max-Planck-Institut für Astrophysik, Karl Schwarzschild Strasse 1, 86740 Garching bei München, Germany*

Received December 27, 1999

Abstract—The angular distribution of low-frequency radiation after a single scattering by relativistic electrons with an isotropic velocity distribution differs markedly from the Rayleigh angular function. In particular, the scattering by an ensemble of ultrarelativistic electrons is described by the law $p = 1 - \cos\alpha$, where α is the scattering angle. Thus, photons are mostly scattered backward. We discuss some consequences of this fact for astrophysical problems. We show that a hot atmosphere of scattering electrons is more reflective than a cold one: the fraction of incident photons reflected after a single scattering can be larger than that in the former case by up to 50%. This must affect the photon exchange between cold accretion disks and hot coronae (or advective flows) near relativistic compact objects, as well as the rate of cooling (through multiple inverse-Compton scattering of the photons supplied from outside) of optically thick clouds of relativistic electrons in compact radio sources. Scattering asymmetry also causes the spatial diffusion of photons to proceed more slowly in a hot plasma than in a cold one, which affects the shapes of Comptonization spectra and the time delay in the detection of soft and hard radiation from variable X-ray sources. *© 2000 MAIK "Nauka/Interperiodica".*

Key words: *Compton scattering, plasma, accretion disks, nonthermal radiation mechanisms, Comptonization, albedo*

INTRODUCTION

In our recent paper (Sazonov and Sunyaev 2000a), we have called attention to the fact that the differential cross section for Thomson scattering of low-frequency photons averaged over an isotropic distribution of relativistic electrons differs markedly from the Rayleigh phase function, which corresponds to the scattering by cold electrons. The resulting angular function is backward-oriented; i.e., photons tend to be scattered backward rather than forward (see Fig. 1). It should be immediately emphasized that this angular function is a characteristic of the scattering by an ensemble of electrons. Similar terminology is used when treating the Compton scattering in dense plasmas, where collective effects are important (see, e.g., Bekefi 1966).

The above phenomenon results from the joint action of two effects. One is that a photon has a higher probability of undergoing a scattering by an electron that is moving toward it rather than away from it (the probability is proportional to the factor $1 - \cos\theta v/c$, where v is the electron velocity, and θ is the angle at which the photon and the electron collide). The other effect is that photons emerge after the scattering preferentially in the direction of motion of the relativistic electron. The angular function in the case under consideration is virtually opposite to the forward-oriented Klein–Nishina angular function, which corresponds to the scattering of energetic photons by an electron at rest.

In this paper, we consider some astrophysical implications of this peculiar scattering behavior of a hot plasma. The most evident consequence of the backward scattering law is that a larger (than in the case of a cold plasma) fraction of the low-frequency photons incident on the surface of an optically thick cloud of relativistic electrons will be reflected from it after a single scattering by an electron. Therefore, fewer photons will be involved in the Comptonization (through multiple scatterings) inside the cloud, and the rate of energy loss by electrons will be lower. Using classical results of the theory of radiative transfer in scattering atmospheres, we derive (see Section 3) simple formulae for the albedos of atmospheres that consist of either mildly relativistic or ultrarelativistic thermal electrons. Our results can be of use, for example, in calculating the photon exchange between cold accretion disks and hot coronae (or mass outflows) above them, as well as in studying the illumination of advective accretion flows by external low-frequency radiation.

Another consequence of the backward-scattering asymmetry is that the coefficient of spatial diffusion for

* E-mail address for contacts: ss@hea.iki.rssi.ru

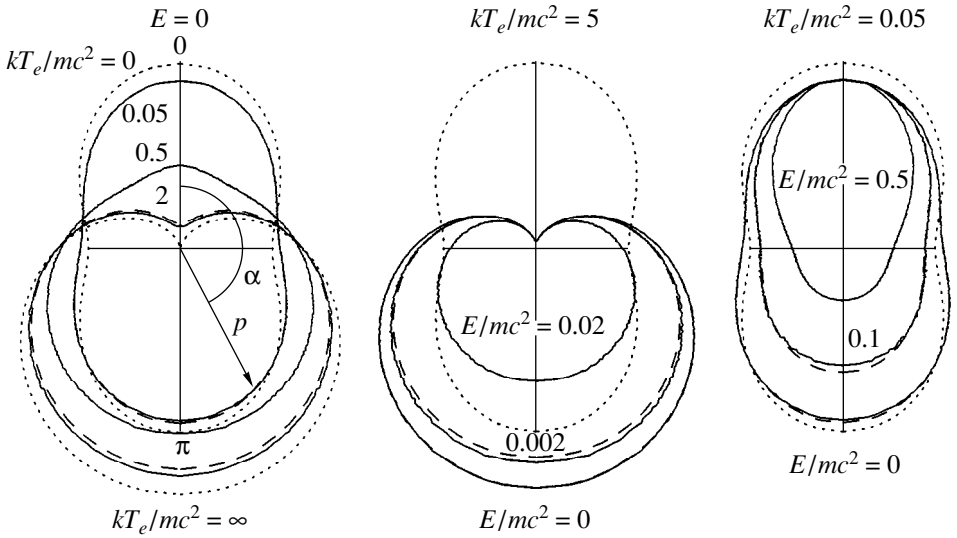

Fig. 1. Angular function (in polar coordinates) for the Compton scattering of photons with energy E by an ensemble of relativistic Maxwellian electrons with temperature T_e. The solid lines indicate the results of our Monte Carlo simulations. The dashed lines represent the fits (when available) given either by Eq. (3) or by Eq. (4). The dotted lines refer to the two extreme cases: an infinitesimal temperature (which corresponds to the Rayleigh angular function) and ultrarelativistic electrons ($kT_e \gg m_e c^2$). In the latter case (presented only in the left panel), the scattering obeys the law $p = 1 - \cos\alpha$.

photons in a hot plasma must be different than that in the case of a nonrelativistic plasma. This affects the Comptonization spectra and time delays in the detection of soft and hard radiation from variable X-ray sources. We discuss this issue in Section 4.

It should be noted that the anisotropic (backward) scattering of low-frequency radiation in a hot plasma has been previously discussed in the literature, and its various astrophysical manifestations have been studied in detail, mostly when considering the formation mechanisms of hard X-ray spectra for compact sources (Ghisellini *et al.* 1991; Titarchuk 1994; Stern *et al.* 1995; Poutanen and Svensson 1996; Gierlinski *et al.* 1997; Gierlinski *et al.* 1999). The scattering angular function proper for an ensemble of Maxwellian electrons was investigated by Haardt (1993), who derived approximate formulae for it from Monte Carlo simulations. The main goal of this study is to present simple analytic formulas for the scattering angular function and related quantities in the ultrarelativistic and mildly relativistic limits.

SCATTERING ANGULAR FUNCTION

The scattering angular function $p(\mu_s)$ allows the probability of scattering through a specified angle $\alpha = \arccos\mu_s$ of a photon by an ensemble of electrons to be determined. We normalize $p(\mu_s)$ in such a way that the photon mean free path in a plasma is

$$\lambda = \frac{1}{N_e \sigma_T \int p(\mu_s) d\mu_s/2}, \quad (1)$$

where N_e is the electron number density, and σ_T is the Thomson scattering cross section. Note that, by the definition (1), $\int p(\mu_s) d\mu_s/2$ is generally < 1 (because of the Klein–Nishina corrections).

Here, we restrict ourselves to the case where low-frequency radiation is scattered by electrons with a relativistic Maxwellian distribution. Two opposite limits can be considered in this situation: (A) the electrons are ultrarelativistic, $kT_e \gg m_e c^2$; and (B) the electrons are mildly relativistic, $kT_e \ll m_e c^2$ (where T_e is the electron temperature). In case (A), the following asymptotic formula is applicable (Sazonov and Sunyaev 2000):

$$p(\mu_s) = 1 - \mu_s. \quad (2)$$

This expression closely corresponds to the ideal situation when $T_e \longrightarrow \infty$ and $\nu \longrightarrow 0$ (ν is the initial photon energy). In this case, the angular function is backward-oriented (see Fig. 1). First-order correction terms, one of which corresponds to the Klein–Nishina correction and the other takes into account the electron finite energy, can be added to Eq. (2) (Sazonov and Sunyaev 2000a):

$$p(T_e, \nu, \mu_s) = 1 - \mu_s - 6\frac{h\nu}{m_e c^2}\frac{kT_e}{m_e c^2}(1 - \mu_s)^2 + \frac{-1 + 3\ln 4 + 6\Gamma(0, m_e c^2/kT_e)}{8}\left(\frac{m_e c^2}{kT_e}\right)^2 \mu_s, \quad (3)$$

where $\Gamma(\alpha, z) = \int_x^\infty x^{\alpha-1} e^{-x} dx$ is the incomplete Gamma function. Formula (3) can serve as a good approximation for $kT_e \gtrsim 2m_ec^2$ and $h\nu kT_e \lesssim 0.01(m_ec^2)^2$.

In case (B), the angular function can be described by the formula (Sazonov and Sunyaev 2000b)

$$p(T_e, \nu, \mu_s) = \frac{3}{4}\Bigg[1 + \mu_s^2 - 2(1-\mu_s)(1+\mu_s^2)\frac{h\nu}{m_wc^2} + 2(1 - 2\mu_s - 3\mu_s^2 + 2\mu_s^3)\frac{kT_e}{m_ec^2} + (1-\mu_s)^2(4+3\mu_s^2)\left(\frac{h\nu}{m_ec^2}\right)^2 + (1-\mu_s)(-7 + 14\mu_s + 9\mu_s^2 - 10\mu_s^3)\frac{h\nu}{m_ec^2}\frac{kT_e}{m_ec^2} + (-7 + 22\mu_s + 9\mu_s^2 - 38\mu_s^3 + 20\mu_s^4)\left(\frac{kT_e}{m_ec^2}\right)^2 + \ldots\Bigg], \quad (4)$$

which is a good approximation when $kT_e \lesssim 0.05m_ec^2$ and $h\nu \lesssim 0.1m_ec^2$. The main term in the above expansion series, $3(1 + \mu_s^2)/4$, describes the standard Rayleigh function, which corresponds to the nonrelativistic case.

Several examples of the scattering angular function for high-temperature electrons, as calculated both from Monte Carlo simulations and from equations (3) and (4), are presented in Fig. 1.

REFLECTION FROM A HOT PLANE-PARALLEL ATMOSPHERE

The angular laws of scattering by an ensemble of Maxwellian electrons described above are readily applicable to any classical problem of radiative transfer in scattering atmospheres. Moreover, as long as the evolution of the photon energy in time and space is unimportant, i.e., the scattering angular function can be considered constant (such a situation takes place, for example, if the energy $h\nu$ remains so small that the Klein–Nishina corrections may be disregarded), we can use some classical results [presented, for example, in the textbooks by Chandrasekhar (1950) and Sobolev (1963)] for hot electron-scattering atmospheres by simply substituting the ensemble-averaged angular function for the classical phase function in the corresponding formulae. Below, we consider the reflection of light from such an atmosphere.

Since Compton scattering involves the transfer of energy between electrons and radiation, it is convenient to perform our analysis in terms of the number of photons rather than in terms of intensity. Our objective is to determine what fraction of the photons incident on the atmosphere is reflected from it after the first scattering. At the same time, this will immediately tell us what fraction of the incident photons can penetrate into the atmosphere while undergoing multiple scatterings, thus taking part in the Comptonization (here, we are talking about an atmosphere with an optical depth $\tau \gtrsim 1$; otherwise, a large fraction of the photons will pass through the atmosphere unscattered). During the subsequent discussion, we restrict ourselves to the case where the energy of the incident photons is low enough for the Klein–Nishina corrections to be unimportant. It should be particularly noted that $\int p(\mu_s) d\mu_s/2 = 1$ in this (Thomson) limit.

In the case of a semi-infinite atmosphere with an optical depth $\tau \longrightarrow \infty$, the number of photons that have undergone a single scattering and emerged in a specified direction $\mu = \cos\theta$, ϕ (the angles are measured relative to the normal to the atmosphere) is given by the relation (Chandrasekhar 1950)

$$N^{(1)}(\mu, \phi; \mu_0, \phi_0) = \frac{1}{4\pi(\mu + \mu_0)} p(\mu, \phi; -\mu_0, \phi_0) F_0, \quad (5)$$

where μ_0 and ϕ_0 specify the direction from which the radiation is incident on the atmosphere, F_0 is the incident photon flux per unit surface area, and p is the scattering phase function.

We may introduce the concept of atmosphere albedo with respect to singly scattered photons:

$$A^{(1)}(\mu_0) = \frac{\int\int N^{(1)}(\mu, \phi; \mu_0, \phi_0)\mu d\mu d\phi}{F_0}, \quad (6)$$

which is a function of the angle of incidence μ_0.

The calculation using equation (6) presents no difficulty for the two scattering laws of interest: (A) $p = 1 - \mu_s$ and (B) $p = 3(1 + \mu_s^2)/4$ (the Rayleigh law), for which the albedos with respect to singly scattered photons are, respectively,

$$\text{(A) } A^{(1)}(\mu_0) = \frac{1}{2}\left[1 + \frac{1}{2}\mu_0 - \mu_0^2 - \mu_0(1-\mu_0^2)\ln\frac{1+\mu_0}{\mu_0}\right], \quad (7)$$

$$\text{(B) } A^{(1)}(\mu_0) = \frac{3}{16}\left[\frac{8}{3} + \frac{1}{2}\mu_0 - \mu_0^2 - \frac{3}{2}\mu_0^3 + 3\mu_0^4 - \mu_0(3 - 2\mu_0^2 + 3\mu_0^4)\ln\frac{1+\mu_0}{\mu_0}\right]. \quad (8)$$

Case (B) corresponds to the situation where the electrons are cold ($kT_e \ll m_ec^2$), whereas case (A) is realized, as follows from the results of Section 2, if the plasma is very hot ($kT_e \gg m_ec^2$). The reflective properties of an atmosphere with the scattering law $p = 1 - \mu_s$

differ markedly from those of a cold atmosphere, as shown by Fig. 2a. In particular, the single-scattering albedo for normally incident photons ($\mu_0 = 1$) is 0.25 for an atmosphere consisting of ultrarelativistic electrons, whereas the corresponding value for case (B) is 0.168. This implies that 50% more photons can be reflected from a hot atmosphere (after a single scattering) than from a cold one. It is evident from Fig. 2a that, even for $kT_e \gtrsim 2m_ec^2$, the albedo does not differ much from the value corresponding to the limiting, ultrarelativistic case (A).

If the electrons are only mildly relativistic, the appropriate expression for the albedo can be derived by integrating the angular function (4):

$$A^{(1)}(\mu_0) = \frac{3}{16}\left\{\frac{8}{3} + \frac{1}{2}\mu_0 - \mu_0^2 - \frac{3}{2}\mu_0^3 + 3\mu_0^4 - \mu_0(3 - 2\mu_0^2 + 3\mu_0^4)\ln\frac{1+\mu_0}{\mu_0} + \left[-2\mu_0 + 6\mu_0^2 + 16\mu_0^3 - \frac{106}{3}\mu_0^4 - 10\mu_0^5 + 20\mu_0^6 - \mu_0(-2 + 16\mu_0^2 - 42\mu_0^4 + 20\mu_0^6)\ln\frac{1+\mu_0}{\mu_0}\right]\frac{kT_e}{m_ec^2}\right\}, \quad (9)$$

where we gave only the correction term proportional to kT_e/m_ec^2. This formula is accurate enough for $kT_e \lesssim 0.2m_ec^2$. As follows from equation (9) and Fig. 2a, the albedo with respect to singly scattered photons of an atmosphere consisting of mildly relativistic electrons is only slightly larger than that of an atmosphere with the Rayleigh scattering law. The relative difference is less than 5% if $kT_e \lesssim 0.1m_ec^2$. We may conclude that, in most practical applications when the reflection of radiation from a plasma with $kT_e \lesssim 0.1m_ec^2$ is studied, the required accuracy will be achieved by using the albedo corresponding to a cold atmosphere.

Although formulas (8) and (9) are, strictly speaking, applicable only to an atmosphere whose optical depth is infinite, a similar increase in the albedo when passing from cold to hot electrons will occur for a transparent atmosphere as well. As follows from Monte Carlo simulations, the single-scattering albedo for normally incident photons increases by approximately 50% when passing from cold to ultrarelativistic electrons for arbitrary optical depths of the atmosphere. An example for which we took $\tau = 0.5$, a value typical of the advection flows near accreting compact objects, is shown in Fig. 2b.

We can also calculate the single-scattering albedo for isotropic incident radiation (when $I_0(\mu_0, \phi_0) = \text{const}$):

$$\text{(A)}\ A_{\text{iso}}^{(1)} = \frac{7 - 4\ln 2}{15} \approx 0.282, \quad (10)$$

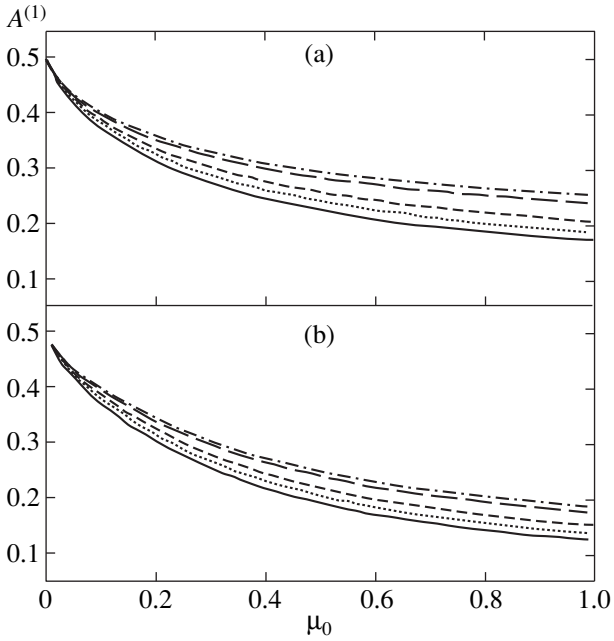

Fig. 2. Albedo of an electron-scattering atmosphere with respect to singly scattered photons versus angle of incidence $\alpha = \arccos\mu_0$. The radiation is of low frequency, $h\nu \ll kT_e \ll (m_ec^2)^2$. The results of our Monte Carlo simulations are shown. (a) The optical depth of the atmosphere is infinite ($\tau \longrightarrow \infty$). Different curves correspond to different electron temperatures: $kT_e \ll m_ec^2$ (solid line), $0.2m_ec^2$ (dotted line), $0.5m_ec^2$ (short dashes), $2m_ec^2$ (long dashes), and $\gg m_ec^2$ (dash–dotted line). (b) The same as (a), but for a transparent atmosphere with $\tau = 0.5$.

$$\text{(B)}\ A_{\text{iso}}^{(1)} = \frac{26 - 27\ln 2}{35} \approx 0.208. \quad (11)$$

Thus, we obtained the following result: 36% more photons are reflected (after the first scattering) from a very hot atmosphere than from a cold one.

PHOTON DISTRIBUTION IN THE TIME OF ESCAPE FROM A CLOUD OF ELECTRONS

In the previous section, we showed that the fraction of the low-frequency photons incident on a cloud of electrons which become the seed photons for the Comptonization inside the cloud, i.e., the normalization constant for the distribution of multiply (more than once) scattered photons in the number of scatterings, depends on the plasma temperature. In this section, we turn to the shape of this distribution, which is also affected (although to a lesser degree) by the scattering angular function.

Sunyaev and Titarchuk (1980) and Payne (1980) derived analytic formulas for the distribution of photons in the time of their escape from a spherical, optically thick plasma cloud. In their derivation carried out

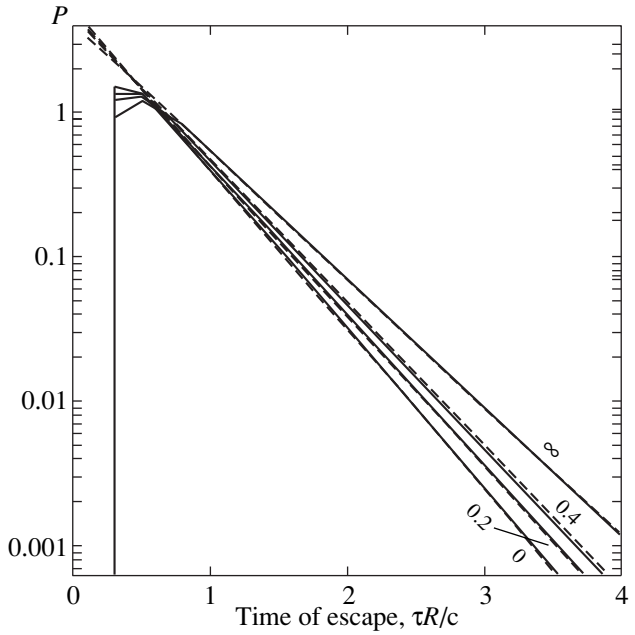

Fig. 3. Distribution of low-frequency photons in the time of their escape from a cloud of electrons with the optical depth $\tau = 5$ (R is the cloud radius) for various plasma temperatures (the values of kT_e/m_ec^2 are shown alongside the corresponding curves). The solid lines represent the results of our Monte Carlo simulations. The dashed lines indicate the results of our calculations by means of the approximate formula (16), which can be used to describe the exponential (power-law in the linear-logarithmic coordinates used here) part of the distribution function. The diffusion coefficient D appearing in equation (16) is given by equation (14) in the case $kT_e \gg m_ec^2$ and by equation (15) in the case $kT_e \leq 0.4m_ec^2$.

in the diffusion approximation, these authors implicitly assumed that the probabilities of forward ($\mu_s > 0$) and backward ($\mu_s < 0$) scattering were equal. This condition is actually satisfied, for example, if the scattering angular function is spherical ($p = 1$) or the Rayleigh one [$p = 3(1 + \mu_s^2)/4$]. The latter is possible when both the photons and the electrons are nonrelativistic ($h\nu,\ kT_e \ll m_ec^2$). However, as we showed in Section 2, the forward–backward symmetry breaks down if the electrons are essentially relativistic.

It is easy to adjust the solution of Sunyaev and Titarchuk (1980) in such a way that it will take into account the dependence of the scattering law on the plasma temperature. To this end, we must use the correct diffusion coefficient, which is given by (see, e.g., Weinberg and Wigner, 1958)

$$D = \frac{1}{3(\sigma/\sigma_T)(1 - \langle\mu_s\rangle)}, \qquad (12)$$

where σ is the total scattering cross section, and

$$\langle\mu_s\rangle = \frac{\int \mu_s p(\mu_s) d\mu_s/2}{\int p(\mu_s) d\mu_s/2}. \qquad (13)$$

In the nonrelativistic limit, $\sigma = \sigma_T$, $\langle\mu_s\rangle = 0$, and $D = 1/3$; it is the latter value that was used by Sunyaev and Titarchuk (1980).

Let us now assume (as we did in Section 3) that the energy of a photon remains low as it diffuses outward from the cloud while undergoing multiple scatterings. Hence, the Klein–Nishina corrections are unimportant. In this case, $\sigma = \sigma_T$, and [see equation (12)] the diffusion coefficient is determined solely by the dependence of $\langle\mu_s\rangle$ on the scattering law.

In the ultrarelativistic case ($kT_e \gg m_ec^2$), it can readily be found, using equation (3), that $\langle\mu_s\rangle = -1/3$, and, consequently,

$$D = \frac{1}{4}. \qquad (14)$$

Thus, the diffusion of low-frequency photons in an ultrarelativistic plasma proceeds a factor of 4/3 more slowly than it does in a cold one. However, it is unlikely that (14) is of practical value. Indeed, a photon acquires a huge amount of energy when scattering from an ultrarelativistic electron of energy γm_ec^2, ($\nu'/\nu \sim \gamma^2$); hence, it typically becomes relativistic (being initially of low-frequency) after few scatterings, and our statement of the problem in the Thomson limit becomes improper.

In the mildly relativistic limit, using equation (4), we find that $\langle\mu_s\rangle \approx -2kT_e/5m_ec^2$ and

$$D(T_e) = \frac{1}{3(1 + 2kT_e/5m_ec^2)}. \qquad (15)$$

We would like to point out that our analysis is similar to the previous studies (Illarionov *et al.* 1979; Grebenev and Sunyaev 1987), in which the diffusion coefficient for the scattering of relativistic photons by cold electrons was derived. There have also been studies (Cooper 1974; Shestakov *et al.* 1988) of the effect of relativistic corrections on the so-called transport cross section, which is used to describe the spatial diffusion of radiation in terms of the intensity rather than in terms of number of photons, as is done here.

Using the diffusion coefficient in the form (15), it is easy to recalculate the distributions of photons in escape time that were deduced by Sunyaev and Titarchuk (1980) for various distributions of photon sources over a spherical cloud. For example, if the source lies at the cloud center and if we are interested in the fate of the photons that underwent more scatterings than the average number, i.e., the dimensionless time $u \equiv c\sigma_T N_e t \gg u_0 = 0.5\tau^2$ (where $\tau \gg 1$ is the optical depth of the cloud along its radius), then

$$P(u) = \frac{2\pi^2 D(T_e)}{(\tau + 2D(T_e))^2} \exp\left[-\frac{u\pi^2 D(T_e)}{(\tau + 2D(T_e))^2}\right], \quad (16)$$

where $D(T_e)$ is given by equation (15).

Figure 3 shows plots of $P(u)$ for several values of kT_e. We see that the agreement between the results of Monte Carlo simulations and the result of equation (16) is satisfactory up to $kT_e \sim 0.4 m_e c^2$. Because of the temperature correction to the diffusion coefficient, photons spend more time (and undergo more inverse Compton scatterings) in the cloud.

The knowledge of how photons are distributed in the time they stay in a scattering cloud is required virtually in all problems related to Comptonization in astrophysical plasmas. In particular, the shapes of Comptonization spectra and the time delays in the arrival of soft and hard radiation from variable X-ray sources strongly depend on this quantity. To solve such problems, it is necessary to additionally study the evolution of the photon energy with time, which is beyond the scope of this paper. Note, however, that much work along these lines (as applied to relativistic thermal plasmas) has already been done (Titarchuk 1994; Hua and Titarchuk 1996; see also references therein).

ACKNOWLEDGMENTS

This study was supported in part by the Russian Foundation for Basic Research (project nos. 97-02-16264, 00-15-96649, and 00-02-16681). We are grateful to the referee, S.A. Grebenev, for valuable remarks. We also wish to thank Drs. A.A. Zdziarski and C. Done, who drew our attention to the necessity of mentioning in the paper a number of published articles that address questions directly related to this study.

REFERENCES

1. G. Bekefi, in *Radiation Processes in Plasmas* (Wiley, New York, 1966).
2. S. Chandrasekhar, in *Radiative Transfer* (Dover, New York, 1950).
3. G. Cooper, J. Quant. Spectrosc. Radiat. Transf. **14**, 887 (1974).
4. G. Ghisellini, I. M. George, A. C. Fabian, and C. Done, Mon. Not. R. Astron. Soc. **248**, 14 (1991).
5. M. Gierlinski, A. A. Zdziarski, C. Done, *et al.*, Mon. Not. R. Astron. Soc. **288**, 958 (1997).
6. M. Gierlinski, A. A. Zdziarski, J. Poutanen, *et al.*, Mon. Not. R. Astron. Soc. **309**, 496 (1999).
7. S. A. Grebenev and R. A. Syunyaev, Pis'ma Astron. Zh. **13**, 1042 (1987) [Sov. Astron. Lett. **13**, 438 (1987)].
8. F. Haardt, Astrophys. J. **413**, 680 (1993).
9. X.-M. Hua and L. G. Titarchuk, Astrophys. J. **469**, 280 (1996).
10. A. Illarionov, T. Kallman, R. McCray, and R. Ross, Astrophys. J. **228**, 279 (1979).
11. D. G. Payne, Astrophys. J. **237**, 951 (1980).
12. J. Poutanen and R. Svensson, Astrophys. J. **470**, 249 (1996).
13. L. A. Pozdnyakov, I. M. Sobol, and R. A. Sunyaev, Astrophys. Space Phys. Rev. **2**, 189 (1983).
14. S. Y. Sazonov and R. A. Sunyaev, submitted to Astrophys. J. (2000b); astro-ph/9910280.
15. S. Y. Sazonov and R. A. Syunyaev, Astron. Astrophys. **354**, L53 (2000a).
16. A. I. Shestakov, D. S. Kershaw, and M. K. Prasad, J. Quant. Spectrosc. Radiat. Transf. **40**, 577 (1988).
17. V. V. Sobolev, *A Treatise on Radiative Transfer* (Van Nostrand, Princeton, 1963).
18. B. E. Stern, J. Poutanen, R. Svensson, *et al.*, Astrophys. J. Lett. **449**, L13 (1995).
19. R. A. Sunyaev and L. G. Titarchuk, Astron. Astrophys. **86**, 121 (1980).
20. L. G. Titarchuk, Astrophys. J. **434**, 570 (1994).
21. A. M. Weinberg and E. P. Wigner, in *The Physical Theory of Neutron Chain Reactors* (Univ. Chicago Press, Chicago, 1958).

Translated by S. Sazonov

Astronomy Letters, Vol. 26, No. 8, 2000, pp. 500–505. Translated from Pis'ma v Astronomicheskiĭ Zhurnal, Vol. 26, No. 8, 2000, pp. 581–586.

Low-Frequency Flux-Density Measurements and Spectral Features of Millisecond Pulsars

A. D. Kuzmin* and B. Ya. Losovsky

Pushchino Radio Astronomy Observatory, Astrospace Center, Lebedev Physical Institute, Russian Academy of Sciences, Pushchino, Moscow oblast, 142292 Russia

Received October 11, 1999

Abstract—Radio flux-density measurements for a large sample of millisecond pulsars at a low frequency of 102 MHz are presented. Using higher frequency measurements, we construct their spectra in the frequency range from 102 MHz to 4.8 GHz, the widest one studied to date. The spectra of millisecond and normal pulsars have been found to differ. The spectra of millisecond pulsars have no low-frequency turnover typical of normal pulsars. The absence of a low-frequency turnover in the spectrum suggests that the emitting regions of millisecond and normal pulsars differ in geometry, which we interpret by deviation of the magnetic field from a dipole one or by compactness of the emitting region. *© 2000 MAIK "Nauka/Interperiodica".*

Key words: *millisecond pulsars, pulsar radio flux density measurements, pulsar radio spectra*

INTRODUCTION

Spectra are one of the main characteristics of pulsars and are of great importance in elucidating the mechanism of their radio emission. Millisecond pulsars represent a special population of pulsars which are distinguished by the period (several milliseconds and tens of milliseconds), its derivative ($\leq 10^{-19}$ s s^{-1}), magnetic-field strength ($\sim 10^8$ G), age ($\sim 10^9$ years), and evolutionary history; studies of their spectra are therefore of particular interest.

Measurements and comparative analyses of the spectra of millisecond pulsars are carried out mainly at high frequencies. Foster *et al.* (1991), Kijak *et al.* (1997), Toscano *et al.* (1998), and Kramer *et al.* (1998, 1999) made measurements and constructed radio spectra of several millisecond pulsars in the frequency range from 425 MHz to 4.8 GHz. Having compared the spectra of millisecond and normal pulsars, these authors found no significant difference between them. At frequencies above 400 MHz, the spectra are represented by a simple power law, $F \propto \nu^{\alpha}$, while the mean spectral index α does not differ markedly from that of normal pulsars.

However, of particular interest are low-frequency spectra, where a low-frequency turnover with the change of sign of the spectral index and the decrease in intensity with decreasing frequency would be expected in millisecond pulsars. Such a spectral turnover is a characteristic feature of normal pulsars (Sieber 1973; Kuzmin *et al.* 1978; Brook *et al.* 1978; Izvekova *et al.* 1979, 1981).

The frequency of the spectrum maximum depends on pulsar period

$$\nu_{max} = 120\, P^{-0.36},$$

where ν is in MHz, and P is in seconds (Malofeev and Malov 1980; Malofeev 1996). One might expect the low-frequency turnover to be most pronounced in millisecond pulsars. For periods $P \leq 50$ ms, the frequency of the spectrum maximum $\nu_{max} \geq 350$ MHz, and, hence, all millisecond pulsars must be in the region of the spectral turnover at the frequency of our measurements (102 MHz).

The first flux measurements and determination of the spectra of millisecond pulsars at low frequencies (102 MHz) were made by Kuzmin *et al.* (1990) and Kuzmin and Losovsky (1996) for the pulsars PSR 1855+09 and PSR J2145–0750. No low-frequency spectral turnover was found. Shitov (1996) measured the flux densities of six millisecond pulsars.

We observed 20 millisecond pulsars at 102 MHz (Kuzmin and Losovsky 1999a). Our comparison of the integrated profiles based on these observations revealed a difference between the frequency dependences of the integrated-profile widths for millisecond and normal pulsars (Kuzmin and Losovsky 1999b). In this paper, we present our radio flux measurements for 18 millisecond pulsars at 102 MHz. Using higher frequency measurements, we construct radio spectra of the millisecond pulsars in a broader (by a factor of 4) frequency range. We compare the spectra of millisecond and normal pulsars.

* E-mail address for contacts: akuzmin@prao.psn.ru

1063-7737/00/2608-0500$20.00 © 2000 MAIK "Nauka/Interperiodica"

OBSERVATIONS

The input data were our observations of the pulsar integrated profiles at 102 MHz (Kuzmin and Losovsky 1999a) and published flux-density measurements at higher frequencies in the range 408–4850 MHz.

The observations were carried out in 1991–1997 with the BSA radio telescope of the Pushchino Radio Astronomy Observatory (Lebedev Physical Institute, Russian Academy of Sciences). We used a 32-channel receiver with the channel bandwidth Δf = 5 kHz. The sampling interval from 0.64 to 0.128 ms was chosen individually for each pulsar, depending on the period P and dispersion measure DM. The integrated profile was formed by synchronous integration of individual pulses with the pulsar period during the passage of the pulsar through the radio telescope beam. To increase the signal-to-noise ratio and to reduce the effects of polarization and scintillations, we added up several observing sessions. The time alignment of the added profiles was performed by means of timing. The pulsar ephemerides were taken from the catalogs of Taylor *et al.* (1995). For profiles with a good signal-to-noise ratio, we additionally corrected the time alignment using the best cross-correlation.

Table 1 lists the pulsars with their periods P, dispersion measures DM, number of added sessions M, and signal-to-noise ratio S/N. The pulsar names are those from the catalog of Taylor *et al.* (1995).

FLUX MEASUREMENTS

We measured the flux densities by comparison with calibration discrete sources with known fluxes using the signal-to-noise ratios of calibration sources and pulsars

$$F_{\rm PSR} = F_{\rm cal}k_{\rm cal}(\Delta f\tau)^{-1/2}_{\rm PSR}({\rm S/N})_{\rm PSR}/k_{\rm PSR}(\Delta f\tau)^{-1/2}_{\rm cal}({\rm S/N})_{\rm cal}.$$

Here, $F_{\rm PSR}$ and $F_{\rm cal}$ are the flux densities, $({\rm S/N})_{\rm PSR}$ and $({\rm S/N})_{\rm cal}$ are the signal-to-noise ratios of the measured pulsar (at pulse maximum) and the calibration source, $k_{\rm cal} = \sin h_{\rm cal}$ and $k_{\rm PSR} = \sin h_{\rm PSR}$ are the coefficients that take into account the dependence of the antenna effective area on height h of the calibration source and the pulsar, Δf is the receiver bandwidth, and τ is the signal integration time.

Since the noise of the receiving system depends on the Galactic-background brightness temperature $T_{\rm bb}$, we chose calibration sources in different sky regions with different brightness temperatures of the Galactic background, and the calibration parameter, which describes the radio-telescope fluctuation sensitivity (in units of flux density),

$$\delta S = F_{\rm cal}k_{\rm cal}(\Delta f\tau)^{1/2}_{\rm cal}/({\rm S/N})_{\rm cal},$$

was represented as

$$\delta S = \delta S_{1000}(a + bT_{\rm bb}),$$

where δS_{1000} is the radio-telescope fluctuation sensitivity toward a sky region with a brightness temperature of 1000 K that was taken as the reference one.

We measured δS_{1000} = 115 ± 25 mJy MHz^{-1} s^{-1}, $a = 0.4 \pm 0.1$, and $b = 0.0006 \pm 0.0001$ using 70 discrete sources with known fluxes, located in sky regions with different Galactic-background temperatures. The flux densities of the calibration sources were determined from the 86-MHz measurements of Artyukh *et al.* (1968) recalculated to our frequency of 102 MHz with their spectral indices.

The measured δS_{1000}, a, and b are in agreement with calculated estimates for the known parameters of the antenna and the receiver system. For an antenna effective area $A \cong 35000\sin h$ m^2, an antenna–feeder efficiency $\eta \cong 0.7$, an antenna stray factor $\beta \cong 0.3$, and a receiver noise factor $F = 1.5$, we have $\delta S_{1000} \cong 100$ mJy MHz^{-1} s^{-1}, $a \cong 0.4$, and $b \cong 0.0006$.

We determined the pulsar radio flux from the relation

$$F_{\rm PSR} = \delta S_{1000}(a + bT_{\rm bb})({\rm S/N})_{\rm PSR}(\Delta f\tau)^{-1/2}_{\rm PSR}/k_{\rm PSR}k_{\rm form},$$

where $k_{\rm form}$ is the form factor of the pulsar profile (on–off time ratio) for recalculation of the pulse peak flux to the pulsar period-averaged flux.

Table 2 (column 2) lists the measured radio flux densities F for 18 millisecond pulsars at 102 MHz.

The errors ΔF (column 3 of Table 2) were determined as the square root of the sum of the systematic and random errors squared $\sqrt{(\sigma^2_{\rm syst} + \sigma^2_{\rm rand})}$. We took the systematic errors to be equal to the error in the radio-telescope fluctuation sensitivity with allowance for its dependence on the Galactic-background brightness temperature: $\sigma_{\rm syst} \cong 25 + 0.0006\,(T_{\rm bb} - 1000)\%$. The random errors were estimated from the scatter of the results of different observing sessions; they also include scintillations.

In order to additionally verify our technique for measuring fluxes from the signal-to-noise ratio, we made check measurements of normal pulsars, whose fluxes were measured by the standard method using a noise generator. A comparison of the check radio flux-density measurements for 40 normal pulsars F (see Fig. 1) with published data $F_{\rm pub}$ (Izvekova *et al.* 1981; Malofeev 1993) shows their good agreement. The mean ratio $F/F_{\rm pub}$ is 0.81 ± 0.10.

For the millisecond pulsars PSR J0034+0534, J1012+5307, B1257+12, J1713+0717, B1855+09, and J2145–0750, the flux densities match, to within the measurement errors, those measured by Shitov (1996).

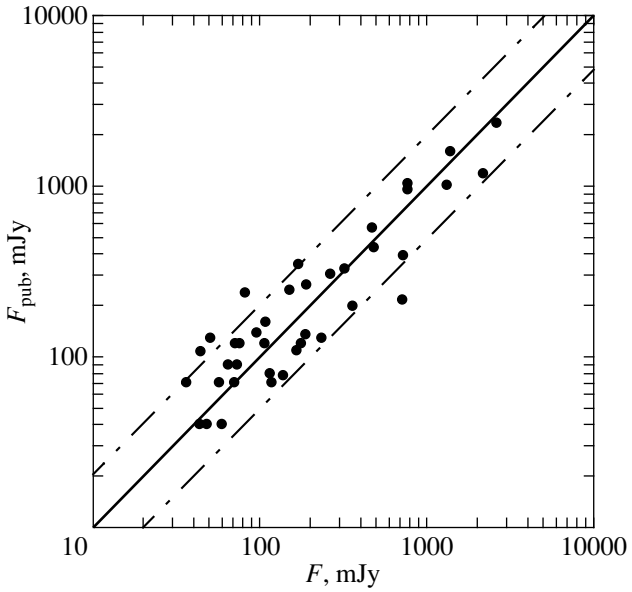

Fig. 1. Comparison of the flux densities of normal pulsars as inferred from our measurements F and from published data F_{pub} (Izvekova *et al.* 1981; Malofeev 1993). The solid line corresponds to $F = F_{pub}$, and the dot–dashed line corresponds to their difference by a factor of 2.

SPECTRA

Figure 2 shows the spectra of 18 millisecond pulsars constructed from our fluxes and from published data.

In contrast to the low-frequency spectral turnover at frequencies $\nu \geq 300$ MHz expected for pulsars with periods $P \leq 50$ ms, of the 18 millisecond pulsars for which we extended the flux-density measurements to low frequencies (to 102 MHz), the low-frequency spectral turnover shows up only in one pulsar, PSR J1012+5307, with a spectral maximum at ~100 MHz. At the same time, for the period of this pulsar $P = 5.25$ ms, the maximum of the spectrum was expected at ~750 MHz, which is not the case. Formally, the spectral turnover can also be noted in the pulsar PSR B1534+12. However, when fitting its spectrum by a power law with a quadratic term, the spectral index of the high-frequency part of the spectrum, $\alpha = -3.8$, differs by more than a factor of 2 from that of the remaining millisecond pulsars. Further flux-density measurements of this pulsar at high frequencies are required. For the remaining 16 millisecond pulsars, the spectra in the entire frequency range from 102 MHz to 4.8 GHz are represented by a simple power law $F \propto \nu^{\alpha}$ and exhibit no low-frequency spectral turnover.

Table 1. Pulsar parameters and observing conditions

PSR	P, ms	DM, pc cm^{-3}	M	S/N
J0034–0534	1.87	13.7	4	15
J0613–02	3.06	38.7	6	10
J0751+1807	3.47	30.2	8	8
J1012+5307	5.25	9.0	7	13
J1022+10	16.45	10.2	5	10
J1025–0709	5.16	6.1	8	12
B1257+12	6.21	10.1	7	15
J1518+1904	40.93	11.6	12	16
B1534+12	37.90	11.6	9	16
J1713+0747	4.57	15.9	20	25
J1730–2304	8.12	9.6	12	8
J1855+09	5.36	13.3	6	16
J1911–1114	3.62	30.9	5	9
J2019+2405	3.93	17.2	17	11
J2033+17	5.94	25.2	13	8
J2145–07	16.05	9.0	11	50
J2229+2643	2.97	23.0	5	8
J2322+2057	4.80	38.4	17	15

The spectral indices α determined by power-law fitting $F \propto \nu^{\alpha}$ are given in column 4 of Table 2. The errors in the spectral indices σ_{α} (column 5) are the formal fitting errors. Column 6 of the table lists references to the high-frequency flux data that we used to construct the spectra. For the pulsar PSR J1012+5307, we fitted the spectrum by a power law with a quadratic term: $\log F = C + \alpha \log \nu + \beta (\log \nu)^2$. Table 2 gives the value of the linear term α for this pulsar. The quadratic term $\beta = -1.0 \pm 0.2$.

The mean spectral index for the millisecond pulsars, $\bar{\alpha} = -1.7 \pm 0.1$, agrees with $\bar{\alpha} = -1.8 \pm 0.1$ obtained by Kramer *et al.* (1998) for 32 millisecond pulsars at higher frequencies.

DISCUSSION

A distinctive feature of the spectra of millisecond pulsars is the absence of a low-frequency turnover or, at least, its considerable shift to low frequencies in comparison with the dependence $\nu_{max}(P) = 120P^{-0.36}$ observed for normal pulsars (Malofeev and Malov 1980; Malofeev 1996).

We interpret the absence of a low-frequency spectral turnover in millisecond pulsars by a difference between the magnetic-field structures (topologies) of millisecond and normal pulsars.

Kuzmin and Solov'ev (1986) showed by model calculations that the pulsar low-frequency spectral turnover is a natural consequence of the hollow-cone model and can be caused by purely geometrical factors, namely, by divergence of the cone of magnetic field lines. This geometrical interpretation of the turnover nature can also explain the absence of this feature in millisecond pulsars. Since the radius of the light cylinder is smaller, the emitting region in millisecond pulsars is closer to the neutron-star surface, where the role of multipole magnetic-field components increases. In a multipole field, configurations with a small divergence of the cone of open field lines are possible (see, e.g., Fig. 5 from Kuzmin and Losovsky 1996).

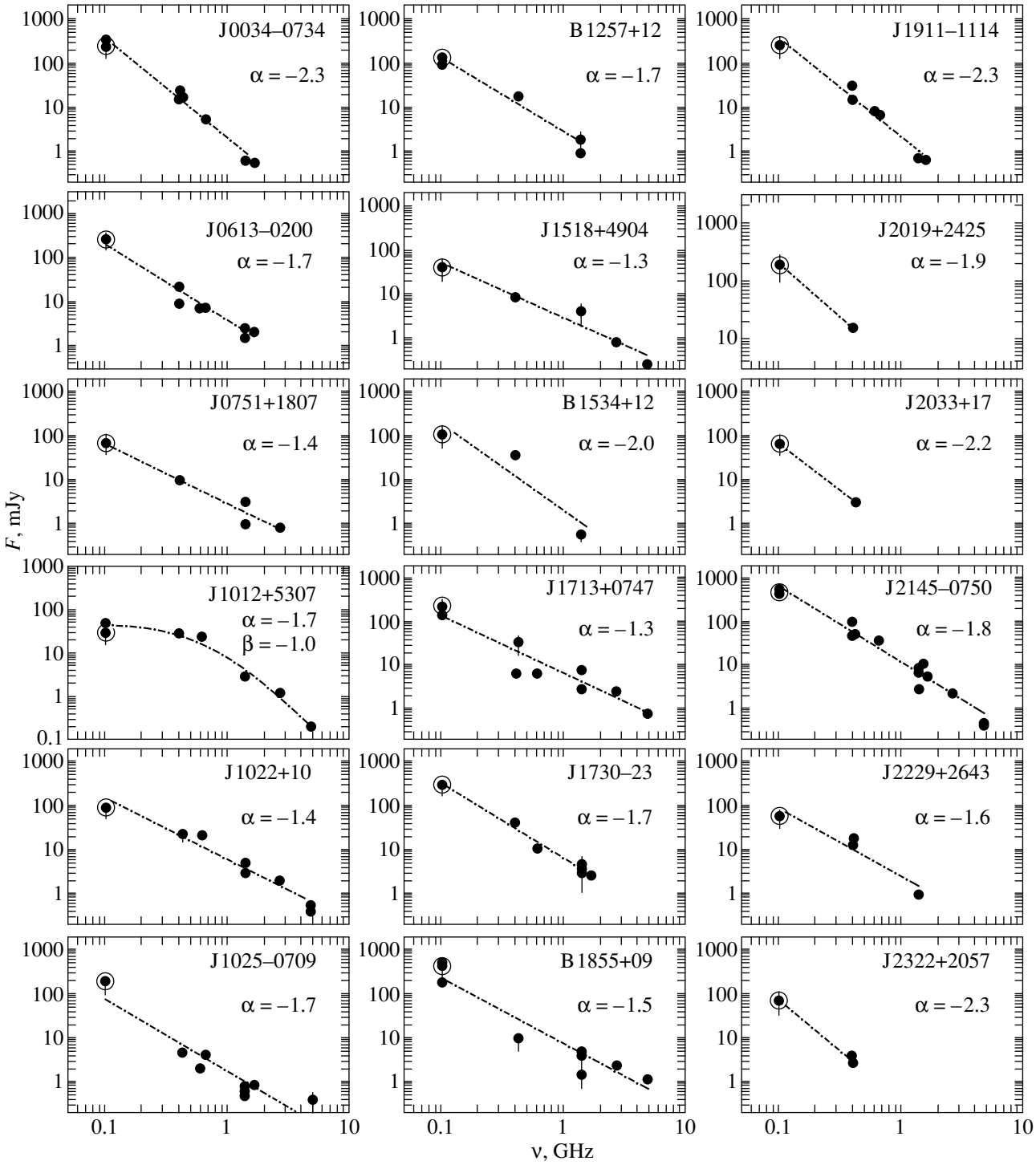

Fig. 2. The spectra of millisecond pulsars. The circled denote indicate our measurements, the points indicate published data, and the dot–dashed line represent the fit $F \propto \nu^{\alpha}$. For the pulsar PSR J1012+5307, the spectrum was fitted by a power law with a quadratic term: $\log F = C + \alpha \log \nu + \beta (\log \nu)^2$.

This interpretation is consistent with the weak frequency dependence of the integrated-profile width for millisecond pulsars, which also suggests a difference in the magnetic-field structures (topologies) of millisecond and normal pulsars (Kuzmin and Losovsky 1996, 1999a, 1999b, 1999c; Kramer *et al.* 1998).

An alternative or complementary interpretation can be compactness of the emitting region of millisecond pulsars and the consequent small difference between the opening angles of the cone of open magnetic field lines at close levels of emission generation at different frequencies. Another alternative can be the idea of two

Table 2. Fluxes and spectral indices

PSR	F, mJy	ΔF, mJy	α	σ_α	References
J0034–0534	250	120	–2.3	0.2	[3, 15, 20, 21]
J0613–02	240	100	–1.7	0.2	[3, 4, 21, 22]
J0751+1807	70	30	–1.4	0.2	[4, 5, 23]
J1012+5307	30	15	–1.7	0.2	[4, 5, 15, 21, 24]
J1022+10	90	40	–1.4	0.2	[2, 4, 5, 21, 25]
J1025–0709	200	100	–1.7	0.2	[3, 4, 5, 26]
B1257+12	150	50	–1.7	0.2	[4, 5, 15, 27]
J1518+4904	40	20	–1.3	0.2	[4, 5, 21]
B1534+12	110	60	–2.0	0.7	[4, 5, 28]
J1713+0747	250	100	–1.3	0.2	[2, 4, 5, 13, 15, 21]
J1730–2304	310	120	–1.7	0.1	[3, 4, 21, 22]
B1855+09	450	250	–1.5	0.2	[1, 2, 4, 5, 15, 30–32]
J1911–11	260	130	–2.3	0.2	[3, 18, 21]
J2019+2405	190	100	–1.9	–	[33]
J2033+17	70	30	–2.2	–	[14]
J2145–07	480	120	–1.8	0.1	[2–5, 15, 20, 21]
J2229+2643	60	30	–1.6	0.4	[4, 25]
J2322+2057	75	40	–2.3	0.2	[25]

Literature to the table: 1, Bailes *et al.* (1994); 2, Stairs *et al.* (1999); 3, Toscano *et al.* (1998); 4, Lorimer *et al.* (1995); 5, Kramer *et al.* (1998); 6, Lundgren *et al.* (1995); 7, Nicastro *et al.* (1995); 8, Camilo *et al.* (1996); 9, Kramer *et al.* (1999); 10, Kijak *et al.* (1997); 11, Bailes *et al.* (1997); 12, Wolszczan, Frail (1992); 13, Wolszczan *et al.* (1991); 14, Foster *et al.* (1993); 15, Kuz'min *et al.* (1990); 16, Segelstein (1986); 17, Foster *et al.* (1991); 18, Fomalont *et al.* (1992); 19, Lorimer *et al.* (1996); 20, Taylor *et al.* (1995); 21, Ray *et al.* (1996); 22, Kuz'min, Losovsky (1996); 23, Shitov (1996).

types of pulsars (Malov 1989), according to which the emission of short-period pulsars is generated near the light cylinder and emerges from approximately the same level, irrespective of frequency. In this case, the low-frequency turnover can also be less pronounced or absent altogether.

CONCLUSION

We have measured the flux densities of 18 millisecond pulsars at the lowest frequency of 102 MHz. Using published data, we have constructed their spectra in the broadest frequency range from 102 MHz to 4.8 GHz.

The spectra of millisecond pulsars in the frequency range from 102 MHz to 4.8 GHz have been found to be represented by a simple power law $F \propto \nu^\alpha$ and exhibit no low-frequency spectral turnover, which is typical of most of the normal pulsars.

We explain the absence of a low-frequency spectral turnover in millisecond pulsars by a difference in the magnetic-field structures (topologies) of millisecond and normal pulsars.

There is no significant difference between the mean spectral indices of millisecond and normal pulsars.

In conclusion, it should be noted that the intensity of the observed radio emission from nearby pulsars at low frequencies is subject to considerable scintillations; therefore, further flux-density measurements with averaging over a larger number of observing sessions are desirable. Flux-density measurements of millisecond pulsars at even lower frequencies are also needed in the search for a possible low-frequency spectral turnover in this range.

ACKNOWLEDGMENTS

We wish to thank Yu. P. Shitov for useful discussions, K.A. Lapaev and V.D. Pugachev for help with the software. This study was supported in part by the Russian Foundation for Basic Research (project no. 98-02-17532) and INTAS (project 96-0154).

REFERENCES

1. V. S. Artyukh, V. V. Vitkevich, R. D. Dagkesamanskiĭ, and V. N. Kozhukhov, Astron. Zh. **45**, 712 (1968) [Sov. Astron. **12**, 567 (1968)].
2. M. Bailes, P. A. Harrison, D. Lorimer, *et al.*, Astrophys. J. Lett. **425**, L41 (1994).
3. M. Bailes, S. Johnston, J. F. Bell, *et al.*, Astrophys. J. **481**, 386 (1997).
4. Yu. M. Bruk, J. G. Davies, A. D. Kuz'min, *et al.*, Astron. Zh. **55**, 1031 (1978) [Sov. Astron. **22**, 588 (1978)].
5. F. Camilo, D. J. Nice, J. A. Shrauner, *et al.*, Astrophys. J. **469**, 819 (1996).
6. E. B. Fomalont, W. M. Goss, and A. G. Lyne, Mon. Not. R. Astron. Soc. **258**, 497 (1992).
7. R. S. Foster, L. Fairhead, and D. C. Backer, Astrophys. J. **378**, 687 (1991).
8. R. S. Foster, A. Wolszczan, and F. Camilo, Astron. Astrophys. **410**, L91 (1993).
9. V. A. Izvekova, A. D. Kuzmin, V. M. Malofeev, *et al.*, Aust. J. Phys. **32**, 25 (1979).

10. V. A. Izvekova, A. D. Kuzmin, V. M. Malofeev, *et al.*, Astrophys. Space Sci. **78**, 45 (1981).
11. J. Kijak, M. Kramer, R. Wielebinski, *et al.*, Astrophys. J. Lett. **318**, L63 (1997).
12. M. Kramer, K. M. Xilouris, D. R. Lorimer, *et al.*, Astrophys. J. **501**, 270 (1998).
13. M. Kramer, Ch. Lange, D. Lorimer, *et al.*, Astrophys. J. **450**, 835 (1999).
14. A. D. Kuzmin, V. M. Malofeev, Yu. P. Shitov, *et al.*, Mon. Not. R. Astron. Soc. **185**, 441 (1978).
15. A. D. Kuzmin and A. G. Solov'ev, Astron. Zh. **63**, 62 (1986) [Sov. Astron. **30**, 38 (1986)].
16. A. D. Kuzmin, Yu. I. Alekseev, K. A. Lapaev, *et al.*, Pis'ma Astron. Zh. **16**, 208 (1990) [Sov. Astron. Lett. **16**, 89 (1990)].
17. A. D. Kuzmin and B. Ya. Losovsky, Astron. Astrophys. **308**, 91 (1996).
18. A. D. Kuzmin and B. Ya. Losovsky, Astron. Zh. **76**, 338 (1999a) [Astron. Rep. **43**, 288 (1999)].
19. A. D. Kuzmin and B. Ya. Losovsky, Pis'ma Astron. Zh. **25**, 441 (1999b) [Astron. Lett. **25**, 375 (1999)].
20. A. D. Kuzmin and B. Ya. Losovsky, Astron. Astrophys. **352**, 489 (1999c).
21. D. R. Lorimer, L. Nicastro, A. G. Lyne, *et al.*, Astrophys. J. **430**, 933 (1995).
22. D. R. Lorimer, A. G. Lyne, M. Bailes, *et al.*, Mon. Not. R. Astron. Soc. **283**, 1383 (1996).
23. S. C. Lundgren, A. F. Zepka, and J. M. Cordes, Astron. J. **453**, 419 (1995).
24. I. F. Malov, Tr. Fiz. Inst. Akad. Nauk SSSR **199**, 83 (1989).
25. V. M. Malofeev and I. F. Malov, Astron. Zh. **57**, 90 (1980) [Sov. Astron. **24**, 54 (1980)].
26. V. M. Malofeev, Pis'ma Astron. Zh. **19**, 366 (1993) [Astron. Lett. **19**, 138 (1993)].
27. V. M. Malofeev, *Pulsars: Problems and Progress, Proc. 160th IAU Coll. Astron. Soc. Pac. Conf. Ser., Sydney, Australia, 8–12 January, 1996* (Sydney, 1996), Vol. 105, p. 271.
28. L. Nicastro, A. G. Lyne, D. R. Lorimer, *et al.*, Mon. Not. R. Astron. Soc. **273**, L68 (1995).
29. P. S. Ray, S. E. Thorsett, *et al.*, Astrophys. J. **470**, 1103 (1996).
30. D. J. Segelstein, Nature **322**, 714 (1986).
31. Yu. P. Shitov, in *Thesis of IAU Colloquium, Sydney, 1996* (Univ. Sydney, Sydney, 1996), p. 66.
32. W. Sieber, Astron. Astrophys. **28**, 273 (1973).
33. I. H. Stairs, R. E. Thorst, F. Camilo, *et al.*, Astrophys. J., Suppl. Ser. **123**, 627 (1999).
34. J. H. Taylor, R. N. Manchester, A. G. Lyne, *et al., Catalog of 706 Pulsars* (1995) (unpublished work).
35. M. Toscano, M. Bailes, R. N. Manchester, *et al.*, Astrophys. J. **506**, 863 (1998).
36. A. Wolszczan and D. A. Frail, Nature **350**, 368 (1991).
37. A. Wolszczan and D. A. Frail, Nature **355**, 145 (1992).

Astronomy Letters, Vol. 26, No. 8, 2000, pp. 506–519. Translated from Pis'ma v Astronomicheskiĭ Zhurnal, Vol. 26, No. 8, 2000, pp. 587–602.

Infrared Photometry of Sakurai's Object (V4334 Sgr) in 1996–1999

A. M. Tatarnikov[1], V. I. Shenavrin[1], B. F. Yudin[1]*, P. A. Whitelock[2], and M. W. Feast[3]

[1] *Sternberg Astronomical Institute, Universitetskiĭ pr. 13, Moscow, 119899 Russia*
[2] *South African Astronomical Observatory, South African Republic*
[3] *Cape Town University, Cape Town, South African Republic*

Received November 20, 1999; in final form, January 20, 2000

Abstract—The infrared photometric observations of V4334 Sgr in 1996–1999 are presented. Together with optical data, they have allowed us to accurately estimate the bolometric flux from this star and to investigate the structure of its dust envelope over the above period. The star is shown to have passed through four well-defined stages in these four years as it moved backward along the post-AGB track, and it now appears to have started moving forward after a halt. At the first stage (1996), there was no dust in the star's envelope. Its visual brightness slightly increased, and it reddened in the entire observed spectral range. The bolometric flux also gradually rose. At the second stage (1997), an optically thick dust envelope condensed around the star, which, however, essentially did not manifest itself at optical wavelengths. The bolometric flux continued to rise through an increase in the star's infrared brightness alone; the rate of its rise also increased. At the third stage (1998–March 1999), V4334 Sgr entered the R CrB phase. First two shallow minima and then two deep minima were observed at optical wavelengths. The star appreciably reddened during the deep minima. The bolometric flux ceased to rise and began to gradually fall in the second half of 1998. At the fourth stage (since March 1999 up until now), V4334 Sgr has been at a protracted deep minimum, which is atypical of the R CrB stars. The bolometric flux between March and October underwent no significant variations. We describe the structure of the dust envelope around V4334 Sgr since its formation. From June 1997 until July 1998, the optical depth of the dust shell, its inner and outer radii, and its mass increased by factors of ~2.2, ~2.0, 2.3, and ~10, respectively. In July 1998, $\tau(V) \approx 2.3$, $R_{\mathrm{d,\,in}} \approx 7.4 \times 10^{14}$ cm, $R_{\mathrm{d,\,in}}/R_{\mathrm{d,\,out}} \approx 0.7$ ($R_{\mathrm{d,\,in}}/R_{*} \approx 47$), and $M_{\mathrm{dust}} \approx 1.6 \times 10^{-7}\ M_{\odot}$. © *2000 MAIK "Nauka/Interperiodica".*

Key words: *stars—variable and peculiar*

INTRODUCTION

On February 20, 1996, the Japanese amateur astronomer Sakurai (1996) discovered a novalike variable in Sagittarius, which was designated V4334 Sgr and is commonly referred to as Sakurai's object. The outburst of this star can be said to have begun before February 1995. At this time, its photographic magnitude was ~$12\overset{m}{.}4$. In September 1994, it was fainter than 15^m. The observations of V4334 Sgr by Duerbeck and Benetti (1996) immediately after its discovery showed that the star appears as an F supergiant whose atmosphere is depleted of hydrogen and enriched with carbon and oxygen. They also detected an old planetary nebula of low surface brightness around the star. All of these findings led them to suggest that V4334 Sgr is a star that underwent the so-called final helium flash at the stage when it was already a planetary nebula nucleus (Iben 1984; Pollaco 1999; Kerber *et al.* 1999). The star returns to the post-AGB track in the temperature–luminosity diagram, initially moving backward along it, i.e., gradually cooling down through its expansion. Another well-studied representative of the so-called born again AGB stars is FG Sge, the central star of the planetary nebula He 1–5.

An analysis of the chemical composition for the atmospheric surface layers of V4334 Sgr shows that, during 1996, the abundance of hydrogen in them decreased, while the abundance of *s*-process elements increased (Asplund *et al.* 1997). In addition, $^{12}C/^{13}C$ = 2–5; i.e., this ratio was very low. In general, the atmosphere of V4334 Sgr proved to be similar in chemical composition to the atmosphere of V854 Cen, an R CrB star with a moderate hydrogen deficiency (Asplund *et al.* 1998).

V4334 Sgr cooled down most rapidly in 1996. By October 1996, according to the calculations by Duerbeck *et al.* (1997) and Arkhipova *et al.* (1998), its effective temperature had decreased by ~1000 and ~1800 K, respectively. Molecular C_2 lines (Kerber *et al.* 1997) and, subsequently, CN and CO lines (Arkhipova *et al.* 1998; Eyres *et al.* 1998) were detected in its spectrum in March 1997, when the observations of V4334 Sgr

* E-mail address for contacts: yudin@sai.msu.su

resumed after a winter pause. Thus, it turned into a carbon star during the winter. Its spectral type in June and October 1997 was estimated to be, respectively, C1,4 ($T_{\rm eff} \approx 4600$ K) and C3,4 ($T_{\rm eff} \approx 4200$ K) (Arkhipova *et al.* 1998). Thus, the star also continued to cool down in 1997, though not so rapidly as it did in 1996. In March 1997, an infrared excess associated with radiation from the condensed dust envelope was detected in the spectral energy distribution of V4334 Sgr (Kimesvenger *et al.* 1997). The envelope parameters were estimated by Arkhipova *et al.* (1998). The infrared spectroscopic observations of Sakurai's star in the first half of 1997 are presented in Eyres *et al.* (1998).

In 1998, the optical light curve of V4334 Sgr exhibited three minima in March, June, and October (Liller *et al.* 1998a; Jacoby and De Marco 1998; Arkhipova *et al.* 1999). The star's visual brightness at the last, deepest minimum dropped by $\sim 7^m$. An even deeper minimum was detected in March 1999 (Jacoby 1999). Thus, V4334 Sgr became similar to R CrB stars not only in atmospheric chemical composition but also photometrically (in light-curve shape).

Here, we present our infrared photometric observations of V4334 Sgr in 1996–1999. Together with optical data, they have allowed us to accurately estimate the bolometric flux from the star and to study the structure of its dust envelope over the above period. We discuss the structure of the dust envelope around V4334 Sgr mainly in context with the question of how well the detected variations in its bolometric flux reflect the actual variations in the star's bolometric luminosity at various stages of its evolution; this essentially reduces to the question of how many holes there are in the dust "blanket" formed around Sakurai's star in 1997 and whether the star falls within one of the holes at a particular time. If the blanket is without holes, i.e., if dust clouds completely cover the star, then it follows from our observations that, being similar to a supergiant, the star moves along the AGB track, though backward, even after the helium flash, and its bolometric luminosity can vary appreciably. In addition, we give here a generalized description of the evolution of a dust envelope. A detailed discussion of the separate aspects of dust formation in the envelope of Sakurai's star and model calculations of its parameters is beyond the scope of this paper. We intend to fill this gap in our next paper.

OBSERVATIONS

The photometric *JHKLM* observations of V4334 Sgr are being carried out with the 1.9-m SAAO telescope (South Africa) and with the 1.25-m telescope at the Crimean Station of the Sternberg Astronomical Institute (SAI). Their results are given in Table 1.

Figure 1 shows *V, K* light and *B–V, J–L* color variations in V4334 Sgr, as well as variations in its bolometric magnitude $m_{\rm bol}$. We used the optical observations of the following authors: Duerbeck *et al.* (1997); Goranskiĭ (1998); Liller *et al.* (1998a, 1998b); Jacoby and De Marco (1998); Arkhipova *et al.* (1998, 1999); and, in part, amateur observers of variable stars VSOLJ (http://www.kusastro.kyoto-u.ac.jp/vsnet). In the (JD, $m_{\rm bol}$) diagram, the bolometric magnitudes estimated by Duerbeck *et al.* and Arkhipova *et al.* (1998) are indicated by crosses. Note that we and the above authors took the same interstellar extinction; it corresponds to the color excess $E(B–V) = 0.54$ (Duerbeck *et al.* 1997). The inclined dashed line indicates bolometric-magnitude variations in the case of stellar expansion at a constant rate without variations in effective temperature (see below for details). The horizontal dashed lines correspond to $m_{\rm bol} = 7.86$ and $m_{\rm bol} = 8.51$.

Figure 2 shows various color–magnitude diagrams not only for V4334 Sgr but also for FG Sge. Note that all points in the *B–V, V* diagram, except for six points (marked by asterisks), were constructed from the observations of V4334 Sgr at the Crimean Station of the SAI alone [see Arkhipova *et al.* (1999) and references therein], which allows systematic errors to be avoided in the magnitude estimates for the star. The rightmost asterisk in this diagram corresponds to the observations of V4334 Sgr in March 1999. Table 2 gives photometric parameters for V4334 Sgr on selected dates, which characterize the star's behavior since its discovery. These dates are marked in Fig. 1. The magnitudes in Fig. 2 and Table 2 were corrected for interstellar reddening with the color excess $E(B–V) = 0.54$.

We calculated the bolometric fluxes by integrating the energy distributions. The latter were constructed from *UBVJHKLM* observations of V4334 Sgr by using various interpolation methods. In addition, the energy distributions were extrapolated to shorter and longer wavelengths.

In 1996, when there was no dust in the stellar envelope, we made extrapolation to shorter wavelengths ($\lambda < 0.36$ μm) in accordance with the spectral energy distribution for a supergiant whose spectral type corresponded to the observed *U–B* color. The observed energy distribution was extended to longer wavelengths ($\lambda > 3.5$ μm) by a blackbody curve with the temperature equal to the color temperature of V4334 Sgr in the range 2.2–3.5 μm. Note that the increase in bolometric-flux estimate through the star's ultraviolet radiation does not exceed 10%. At the same time, when the energy distribution is extrapolated in the infrared, its increase is negligible (~1%). During interpolation, we first converted the spectral fluxes and the corresponding wavelengths to a logarithmic scale and then interpolated the relation $\log F_\lambda = f(\log\lambda)$ by using an appropriate polynomial. Figure 3 (left panel) shows the spectral energy distribution for V4334 Sgr in June 1996 (JD 2450242 in Table 2), together with the spectral energy distribution for a G0 Ib supergiant, a blackbody curve with $T = 6400$ K, and the fit. Note that the black-

Table 1. Photometric *JHKLM* observations of V4334 Sgr at SAAO (1) and at the Crimean Station of the SAI (2)

JD 2450000+	*J*	*H*	*K*	*L*	*M*	Observatory
0142	9.36	9.04	8.85	8.80*		1
0147	9.30	8.98	8.80	8.67		1
0199	9.10	8.77	8.58			1
0203	9.10	8.77	8.57	8.40		1
0242	8.94	8.77	8.35	8.01*		2
0318	8.62	8.27	8.02	7.83		1
0325	8.60	8.22	8.00	7.82		1
0383	8.44	8.04	7.77	7.51		1
0387	8.44	8.02	7.76	7.57		1
0536	7.86		6.24			2
0563	7.75	6.86	6.10	4.98		1
0597	7.65	6.76	6.02	4.84		1
0624	7.58	6.62	5.77	4.55	4.45	2
0625	7.55	6.53	5.75	4.51	4.43	2
0642	7.46	6.47	5.60	4.38		1
0676	7.24	6.37	5.45	4.09		2
0679				4.00		2
0701	7.36	6.30	5.41	3.91	3.81	2
0760	7.24	6.21	5.32	3.88		1
0873	7.72	6.34	5.13	3.54		1
0914	7.56	6.22	5.12	3.56		1
0918	7.42	6.25	5.20	3.59	3.19	2
0966	7.51	6.21	5.09	3.51	3.25	2
0977	7.45	6.16	5.11	3.33	3.27	2
0981			5.08	3.39		2
1007	7.22	6.08	4.97	3.15	2.95	2
1034		6.43	5.19	3.26		2
1036	7.81	6.46	5.20	3.23		2
1037	7.84		5.18			2
1039			5.25	3.27		2
1040	7.94	6.62	5.26	3.27	2.98	2
1062		6.77	5.37	3.26		2
1069		6.83	5.35	3.22		2
1094	9.80	7.36	5.49	3.32		1
1299	12.18	8.71	6.30	3.60		1
1328	12.33	8.91	6.43	3.70		1
1352		9.33*	6.54	3.56		2
1361		9.56*	6.77	3.68	3.02	2
1391	13.73*	9.64	6.91			1
1453			6.83	3.38		2
1456		9.72	6.85	3.69		1

* The measurement error is $0^m.1$. In the *M* band, it does not exceed $0^m.07$. In the remaining cases, it is smaller than $0^m.03$.

body temperature was determined from the observed *B–V* color.

In the (JD, m_{bol}) diagram (Fig. 1), the m_{bol} estimates obtained in 1996 by Duerbeck *et al.* (1997) and Arkhipova *et al.* (1998) are indicated by crosses. Their estimation method was based on the calculation of a bolometric correction to the *V* magnitude of V4334 Sgr in accordance with the star's spectral classification by *B–V*. In the former and latter papers, it was compared with the corresponding colors of numerical models for

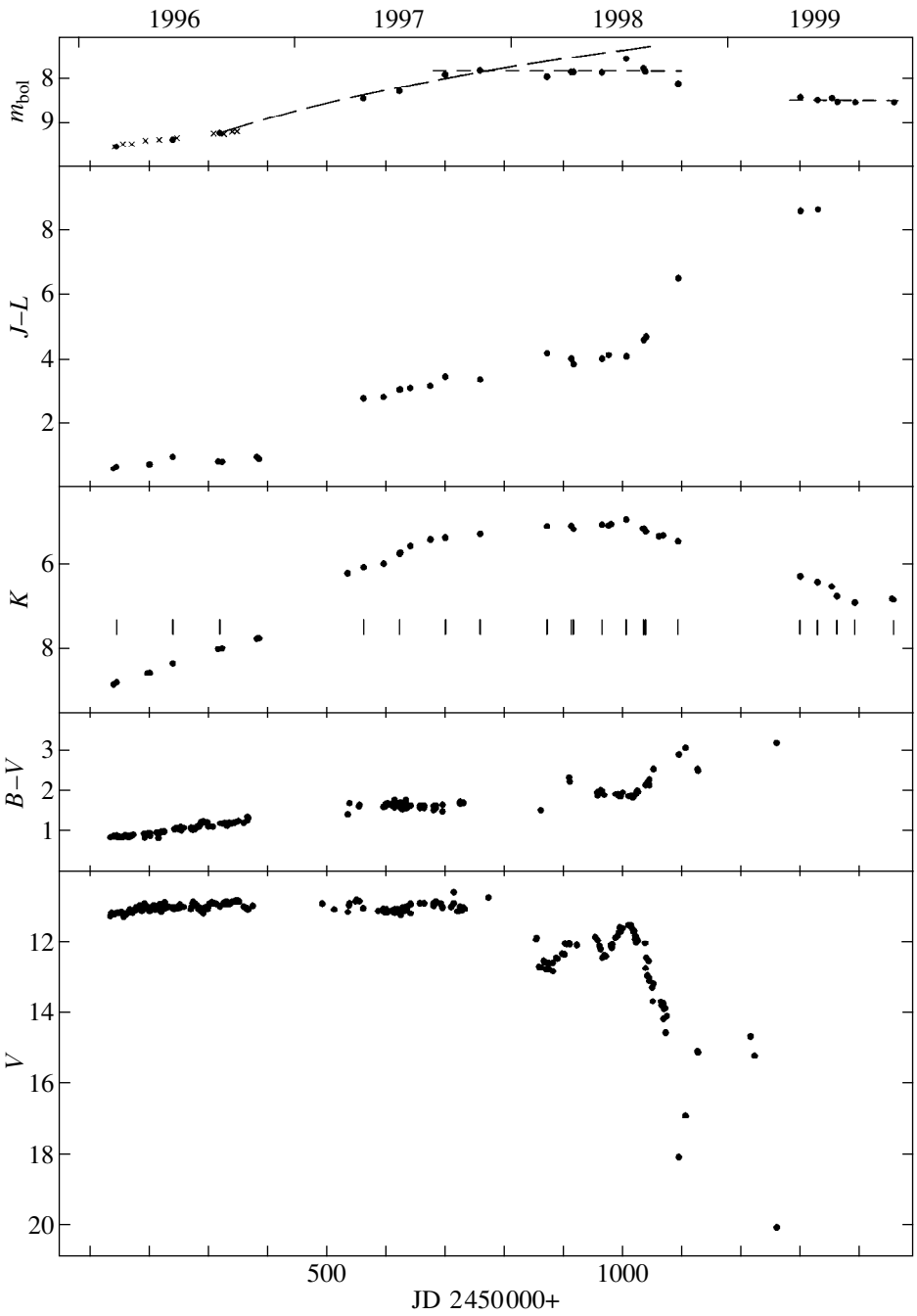

Fig. 1. *V, K* light, *B–V, J–L* color, and bolometric-magnitude variations in V4334 Sgr during 1996–1999. The optical data were taken from the papers cited in the text. The bars in the (JD, *K*) diagram indicate the dates for which we computed the bolometric magnitudes of V4334 Sgr. The crosses in the (JD, m_{bol}) diagram represent the estimates of m_{bol} obtained by Duerbeck *et al.* (1997) and Arkhipova *et al.* (1998); the inclined dashed line indicates bolometric-magnitude variations in the case of stellar expansion at a constant rate estimated in 1996 without change in effective temperature. The horizontal dashed lines correspond to $m_{bol} = 7.86$ and 8.51.

hydrogen-poor stellar atmospheres and with the colors of normal supergiants, respectively. We see from Fig. 1 that there is good agreement between all m_{bol} estimates in 1996. All of them can be said to lie within an inclined strip $<0^m.1$ in width.

In 1997, an optically thick dust envelope formed around V4334 Sgr, which has persisted to the present day. From then on, the bolometric correction due to the stellar radiation at $\lambda < 0.36$ μm has been negligible (< 1%). The energy distribution was interpolated in the same way as described above. At the same time, the bolometric correction due to the radiation at wavelengths longer than the upper limit of the spectral range of our observations was estimated from model energy distri-

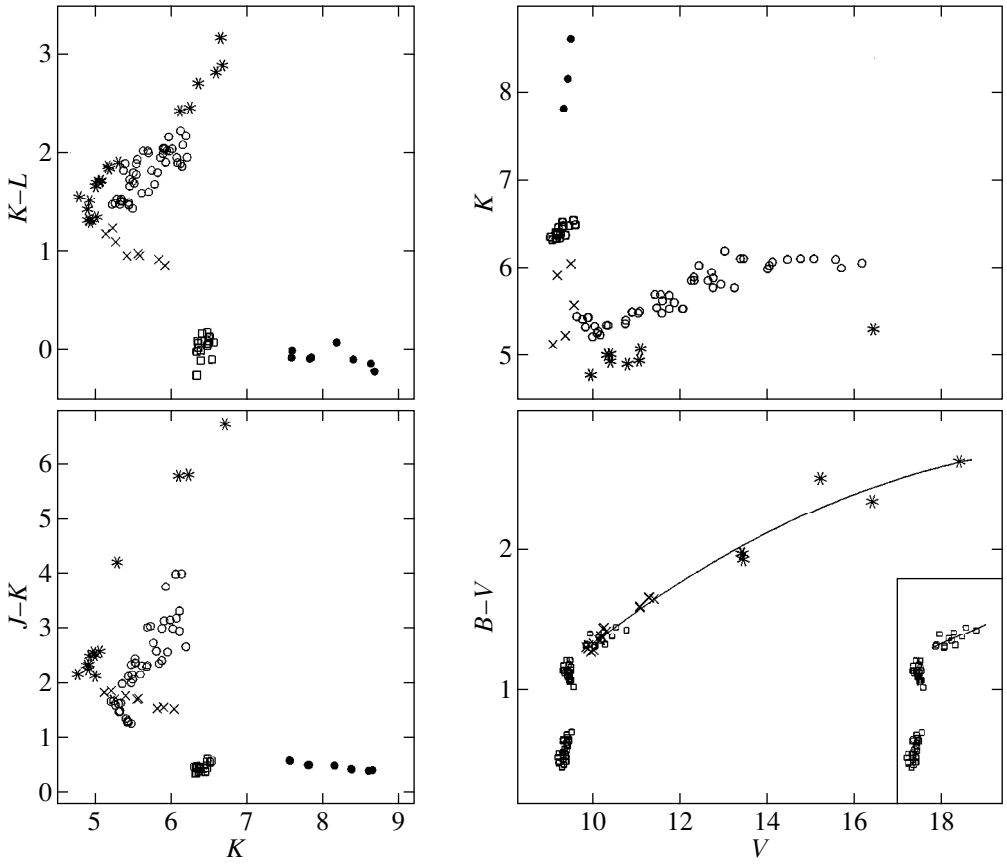

Fig. 2. (*J–K*, *K*), (*K–L*, *K*), (*K*, *V*), and (*B–V*, *V*) diagrams for V4334 Sgr and FG Sge corrected for interstellar reddening. In the first three diagrams, the squares and circles mark the positions of FG Sge, while the dots, crosses, and asterisks mark the positions of V4334 Sgr. The squares and circles refer to the observations of FG Sge before and after the onset of the R CrB stage, respectively. The dots, crosses, and asterisks refer to the observations of V4334 Sgr in 1996, 1997, and 1998–1999, respectively. When constructing the (*K*, *V*) diagram, we increased the visual magnitude of FG Sge by $1\overset{m}{.}4$. In the (*B–V*, *V*) diagram, the squares and crosses represent the observations by Arkhipova *et al.* (1999) (see also references therein), and the asterisks represent the observations by Jacoby and De Marco (1998) and Jacoby (1999). The two groups of squares along the vertical line refer to 1996 (lower) and 1997 (upper). The squares also mark the positions of V4334 Sgr in 1998 before the onset of its first profound brightness decline. The crosses and asterisks, except the rightmost asterisk, which was obtained at the deep minimum in March 1999, refer to this episode. The solid line represents a second-degree polynomial fitting the (*B–V, V*) relation in this segment. In the insert, the solid line represents a linear polynomial fitting the (*B–V, V*) relation when the star passed through the shallow minimum in June 1998 (see Fig. 1).

butions. They were computed for two dates in 1997 and for three dates in 1998 (JD 2450624, 701, 873, 1007, and 1094). Note that the increase in bolometric-flux estimate through the stellar radiation at wavelengths longer than 4.8 μm (*M* band) is ~10% in 1997 and ~20% in 1998. At the same time, the correction due to the radiation at wavelengths longer than 10 μm (*N* band) is a mere ~1%.

At the deep optical minimum in October 1998 (JD 2451094), the bolometric flux from V4334 Sgr was almost completely concentrated in the infrared. No more than 1% and 4% of the bolometric flux was concentrated at wavelengths $\lambda < 1$ μm and $\lambda < 1.6$ μm, respectively. Since V4334 Sgr became even redder in the infrared in late April, 1999 (JD 2451250), a mere ~1% of the star's bolometric flux remained at $\lambda < 1.6$ μm. This allows us to estimate the bolometric flux from V4334 Sgr in 1999 on those dates on which no *J* observations are available. Note also that there is a match between the *M* magnitudes of V4334 Sgr estimated in August 1998 and in July 1999, allowing them to be used to construct the spectral energy distribution for V4334 Sgr on all dates of its observations in 1999. In addition, to reduce the error in the estimated bolometric flux, we added the *BVRI* magnitude estimates of V4334 Sgr obtained in March 1999 (Jacoby 1999) to our infrared magnitude estimates for this star.

Figure 3b shows the energy distribution in June 1997 (JD 2450624), together with the interpolated and model energy distributions. In the range 0.36–4.8 μm, the difference between the total fluxes under the last two curves does not exceed 2%. In April 1997 (JD 2450553),

Table 2. Magnitudes, colors, and bolometric magnitudes of V4334 Sgr on selected dates

JD(opt) 2450000+	JD(IR) 2450000+	V	K	$B–V$	$J–K$	$K–L$	m_{bol}
147	147	9.50	8.62	0.35	0.22	0.05	9.56
242	242	9.43	8.17	0.51	0.31	0.25	9.40
321	325	9.34	7.83	0.66	0.32	0.10	9.25
556	563*	9.19	5.92	1.09	1.37	1.03	8.47
624	624	9.57	5.58	1.07	1.52	1.14	8.30
726	701	9.37	5.23	1.16	1.67	1.41	7.93
774	760	9.03	5.13	1.18	1.64	1.35	7.84
860	873	11.07	4.95	0.98	2.31	1.51	7.97
911	914*	10.41	4.94	1.73	2.16	1.47	7.87
966	966*	10.80	4.91	1.45	2.14	1.49	7.88
1000	1007	9.96	4.79	1.42	1.97	1.73	7.57
1026	1036	10.33	5.01	1.44	2.36	1.85	7.79
1039	1039	11.10	5.08	1.61	2.40	1.90	7.86
1095	1094	16.42	5.31	2.36	4.03	2.08	8.13
1259	1299	18.41	6.12	2.64	5.60	2.61	8.44
	1328		6.25		5.62	2.64	8.50
	1352		6.36			2.89	8.46
	1361		6.59			3.00	8.54
	1391		6.73		6.54	3.13	8.55
	1456		6.67			3.07	8.55

Note: The magnitudes were corrected for interstellar reddening with $E(B–V) = 0.54$ (Duerbeck and Benetti 1996). JD(opt) and JD(IR) are the Julian dates of the optical and infrared observations, respectively. The optical data were taken from the papers cited in the text.

* N observations of V4334 Sgr are available near these dates.

a spectrum of V4334 Sgr was taken on the Infrared Space Observatory (ISO) in the range 2.4–40 μm (Eyres *et al.* 1998); this spectrum allowed us to estimate its N magnitude, $\sim 4\overset{m}{.}6$. This magnitude estimate for V4334 Sgr in the N band may be added to our estimates of its *JHKL* magnitudes, which were also obtained in April 1997 (JD 2450563 in Table 2). This allows the contribution of the star's radiation in the range 3.5–10 μm to its bolometric flux to be estimated. The N flux from the star in April is marked in Fig. 3b. Note that the star's L brightness rose by $\sim 0\overset{m}{.}4$ between April and June. Its N brightness may therefore be slightly higher than the above level.

Lynch *et al.* (1998) with the 3-m IRTF telescope and Kaeufl and Stecklum (1998) with the 3.6-m ESO telescope carried out N observations of V4334 Sgr on JD 2450894, 946, and JD 2450977, respectively. Given the observational errors, the magnitude estimates of the star for all three dates proved to be the same: $N = 1\overset{m}{.}7 \pm 0\overset{m}{.}1$. Not only the energy distributions on dates close to the dates of N observations, but also all the remaining ones referring to 1998 (Table 2) may be supplemented with this point. Such a procedure is quite justifiable for several reasons. First, the small ($<0\overset{m}{.}5$) L light variations of the star in 1998 (Table 1) suggest small N variations as well. To be more precise, they must be smaller in N than in L. Second, when changing the N magnitude estimate for the star by $0\overset{m}{.}5$, the bolometric-flux estimate changes by $\leq 2\%$.

Thus, to summarize our discussion of the technique for estimating the bolometric flux from V4334 Sgr in its various states, we can say that the errors in the estimated bolometric magnitudes (Table 2) apparently do not exceed $0\overset{m}{.}1$. Figure 4 shows (V, Δm_{bol}) and (K, Δm_{bol}) diagrams ($\Delta m_{bol} = m_{bol} - 7.86$).

THE BEHAVIOR OF V4334 Sgr IN 1996–1999

Figure 1 shows that the star's visual brightness underwent the smallest variations during 1996–1997 (see also Fig. 2). All the points of the visual light curve referring to this period can be said to lie within a $0\overset{m}{.}5$-wide horizontal strip and, in the (K, V) and ($B–V$, V) diagrams, within the corresponding vertical strips (Fig. 2). Arkhipova *et al.* (1999) found that all well-observed times of minimum visual light for V4334 Sgr in 1996–1997 could be described, by analogy with FG Sge, in terms of the model of a pulsating star with a single but systematically increasing pulsation period. According

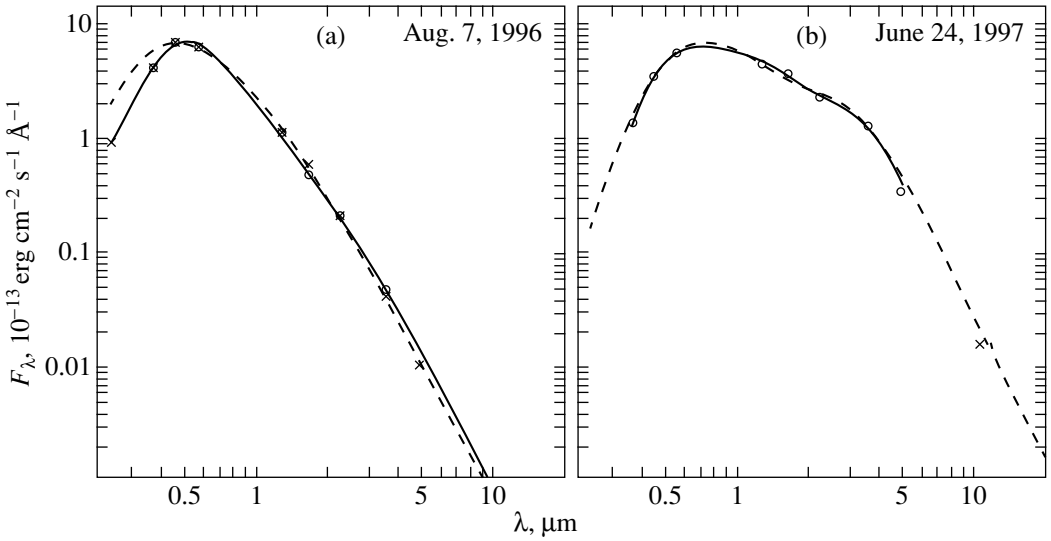

Fig. 3. The spectral energy distributions for V4334 Sgr (a) in June 1996 and (b) June 1997 (JD 2450242 and 2450624 in Table 2, respectively). They are indicated by circles. (a) The crosses indicate the spectral energy distribution for a G0 Ib supergiant, the solid line represents a fit to the energy distribution, and the dashed line represents the spectral energy distribution for a blackbody source with $T = 6400$ K; (b) the cross indicates the N flux in April 1997 estimated from the spectrum of V4334 Sgr (Eyres *et al.* 1998), the solid line represents a fit to the energy distribution, and the dashed line represents a model energy distribution.

to their estimates, the period increased from 9 to 40 days in two years. They believe the period increase to be a direct result of the star's gradual cooling and expansion.

In 1996, when the spectral energy distribution of V4334 Sgr exhibited no infrared excess (Fig. 3), i.e., when there was no appreciable amount of dust in its envelope, the validity of this assertion directly follows from the observed increase in the star's optical and infrared color indices (Fig. 1). The star's cooling was accompanied by a rise in its bolometric flux. It rose by a factor of ~1.35 between March and September (Table 2). The bolometric-flux variations can be excellently described by a linear function:

$$F_{\rm bol}(t)/F_{\rm bol}(147) = 1.9 \times 10^{-3} t + 1,$$

where t = JD – 2450147.

As we see from Fig. 3, the spectral energy distribution for V4334 Sgr in the range 0.44–3.5 μm (*BVJHKL*) in 1996 can be satisfactorily fitted by a blackbody curve. The difference becomes noticeable only in the violet. However, the difference between the total fluxes under these curves in the entire spectral range in Fig. 3 does not exceed 10%. Expressing the bolometric and *K* fluxes in terms of the solid angle and effective temperature of the star (in the latter case, we rely on the fact noted above) for two dates of its observations (JD 2450147, 2450321 in Table 2) and solving the derived set of two equations yield $T_{\rm eff}(321)/T_{\rm eff}(147) \approx 0.86$ and $R_*(321)/R_*(147) \approx 1.55$. Duerbeck *et al.* (1997) estimated the cooling of V4334 Sgr to be slightly smaller. Accordingly, its expansion was smaller, because the estimated bolometric fluxes are essentially equal. At the same time, according to the estimates by Arkhipova *et al.* (1998), the reverse is true. Recall that the stellar temperature in these studies was determined in accordance with the star's spectral classification by *B–V*. In the former and in the latter, it was compared with the corresponding colors of numerical models for hydrogen-poor stellar atmospheres and with the colors of normal supergiants, respectively.

If the expansion of Sakurai's star in 1996 is assumed to have been uniform, then the rate of increase in its radius was $\sim 3.1 \times 10^{-3}\ R_*(147)$ day^{-1}. The inclined dashed line in Fig. 1 indicates the (JD, $m_{\rm bol}$) relation derived by assuming that in 1997–1998 Sakurai's star expanded uniformly, at the same rate, and without any change in effective temperature. Its deviation from the observed points of the bolometric light curve in 1997 turned out to be no larger than $0\overset{m}{.}1$ (~2% on the temperature scale). If the dust envelope condensed in 1997 was spherically symmetric and if the effective temperature of V4334 Sgr decreased in accordance with its spectral classification (Arkhipova *et al.* 1998), then we could say that the star's expansion rate in 1997 increased.

If the distance to V4334 Sgr is ~5.5 kpc (Duerbeck and Benetti 1996), then its bolometric luminosity early in March 1996 (JD 2450147 in Table 2) was $L_{\rm bol} \approx 3.2 \times 10^3\ L_\odot$. At $T_{\rm eff} \approx 8000$ K (Duerbeck *et al.* 1997; Arkhipova *et al.* 1998), the star's photospheric radius is $R_* \approx 30\ R_\odot$, and its expansion rate is $\sim 0.09\ R_\odot$ day^{-1}. At such an expansion rate, if it had been constant since the outburst, the latter should have occurred in April 1995, while it actually occurred in the

fall of 1994. Thus, the expansion appears to have taken place with acceleration at the initial stage of the outburst (Duerbeck *et al.* 1997).

In the spring of 1997, when the observations of V4334 Sgr resumed after the winter pause, it was a carbon star with an appreciable infrared excess associated with dust radiation (Fig. 3). Its bolometric flux increased in this time by a factor of ~2 (Table 2, Fig. 4) virtually through the increase in infrared flux alone (Figs. 1 and 2). Since the visual brightness of V4334 Sgr was essentially at the level of the second half of 1996 (Figs. 1 and 2), the dust envelope did not show up in any way visually. The bolometric flux continued to rise during the entire 1997 at a higher rate than it did in 1996 (Fig. 1) and also through the increase in infrared flux alone. In November 1997 (JD 2450760 in Table 2), it was a factor of ~4.9 and ~3.7 higher than the level in February and August 1996, respectively.

The infrared color indices of V4334 Sgr abruptly increased because of the dust-envelope radiation (Figs. 1 and 2). The *B*–*V* color index also increased (Figs. 1 and 2), but not so much as one might expect for a normal reddening law from a dust envelope producing such a large infrared excess. In principle, the increase in the star's reddening at optical wavelengths could be entirely attributed to its further cooling. In general, we can say that in 1997 *B*–*V* fluctuated within $0\overset{m}{.}3$ (Figs. 1 and 2), while its mean value was ~$0\overset{m}{.}4$ larger than that in late September 1996. At the same time, the visual brightness of V4334 Sgr, while also fluctuating, was within its 1996 values. There was no appreciable correlation between the star's *V* magnitude and its *B*–*V* color in these years (Fig. 2).

Thus, if there were no infrared observations, dust condensation in the envelope of Sakurai's star would go unnoticed. The rise in the infrared flux from V4334 Sgr observed in 1997 without appreciable variations in its optical light implied an increase in the contribution of the dust envelope to the star's bolometric flux. In other words, dust particles continued to condense and/or grow, and, accordingly, the optical depth of the dust envelope gradually increased during 1997. If it was a blanket with holes, then the optical depth averaged over the sphere can be said to have increased.

The situation changed drastically in 1998. The visual brightness of Sakurai's star generally decreased, and first two shallow but distinct minima and then a very deep minimum appeared in the corresponding light curve (Fig. 1). At the same time, the bolometric magnitude was generally at the level of the fall of 1997. Its estimates obtained during this period lie within a $0\overset{m}{.}6$-wide horizontal strip, whose middle is marked in Fig. 1 (JD, m_{bol}) by a horizontal dashed line (m_{bol} = 7.86).

Note that there are only two *B*–*V* color estimates for the episode of the first shallow minimum: at the minimum itself and immediately after it. They were

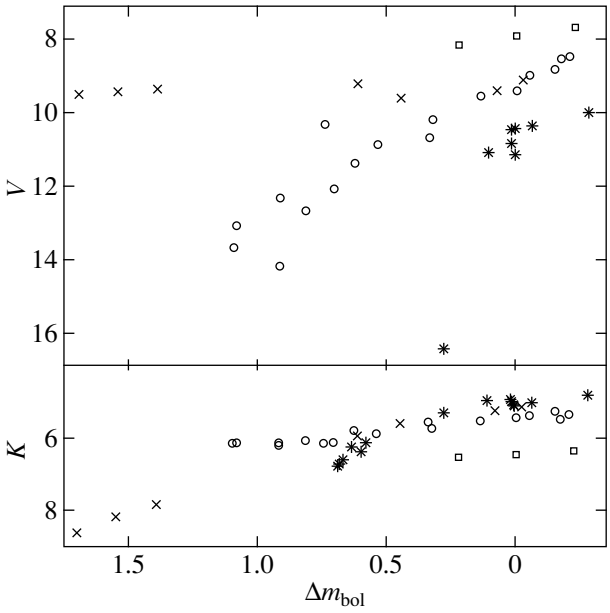

Fig. 4. The (K, Δm_{bol}) and (V, Δm_{bol}) diagrams constructed for V4334 Sgr (crosses and asterisks) and FG Sge (squares and circles). $\Delta m_{bol} = m_{bol}$–7.86. The data for V4334 Sgr and FG Sge were taken from Table 2 and Tatarnikov *et al.* (1998), respectively. The crosses and asterisks refer to the observations of V4334 Sgr during 1996–1997 and 1998–1999, respectively. The squares and circles refer to the observations of FG Sge before and after the onset of dust formation in its envelope.

obtained by Liller *et al.* (1998b) and Goranskii (1998). As we see from Fig. 1, the star appears appreciably bluer at the minimum than it does after it. However, as these observations were carried out with different photometers, we apparently cannot assert that such a behavior of the star's color is typical of the episodes of its temporary visual fading, especially since such a situation was not observed at the two succeeding minima.

In the first half of 1998, i.e., before the onset of the first profound decline in the visual brightness of V4334 Sgr, its *B*–*V* color was, on the average, ~$0\overset{m}{.}25$ larger than that in 1997. In the (*B*–*V*, *V*) diagram (Fig. 2), the points referring to this period were constructed by using data from Arkhipova *et al.* (1999). The second shallow minimum corresponds to them in the visual light curve (Fig. 1). If we formally smooth this portion of the (*B*–*V*, *V*) diagram with a linear function, then the slope of this straight line will correspond to $R = A(V)/E(B–V) \approx 7.1$. In other words, the star slightly reddened at the minimum.

If the second shallow minimum in the star's visual light curve is attributable to the condensation of an additional amount of dust in its envelope, then these dust grains will differ markedly in total-to-selective absorption ratio (R) from interstellar ones with $R \approx 3.1$. They must be much larger in size. For graphite and silicate grains, whose optical properties are given in Draine (1985), it turns out that their radii must be in the

range 0.8–1.0 μm in order to obtain $R \approx 7$. However, the observed correlation between the star's color and magnitude may prove to be false; it may have arisen simply because of the limited number of points in the corresponding portion of the (*B–V*, *V*) diagram (an insert in Fig. 2). In its turn, the amplitude of the bolometric-magnitude variations in this episode was a mere $\sim 0\overset{m}{.}3$, so it can be associated, in principle, with stellar pulsations.

The star's reddening was clearly observed during the first deep minimum. It began as soon as the brightness started to decline, and the initial (*B–V*, *V*) relation was sharper (Fig. 2). When smoothing it with a second-degree polynomial (Fig. 2), we found that $R = A(V)/E(B–V) = 1/(0.47–0.02V)$. Thus, $R \approx 4.3$ at the onset of brightness decline. Only fine ($a_{gr} < 0.07$ μm) silicate grains have such a value of this parameter. Note that $R < 2.2$ for the corresponding graphite grains. At minimum visual light ($V \approx 16.4$), $R \approx 7$. The increase in *R* may stem from the fact that, when the star's direct radiation is greatly attenuated, its light scattered by the dust envelope will contribute appreciably to the object's optical flux. At the same time, the scattered light is bluer than the incident one, because the scattering by fine grains obeys the Rayleigh law. However, this all is true only in the model in which the attenuation of optical starlight is attributed to the formation of only a dust cloud on the line of sight rather than a cloud cover without breaks. The cloud in this model attenuates its direct radiation, while the dust envelope, which had already formed by this time, scatters it.

The bolometric flux at minimum visual light of V4334 Sgr in October 1998 accounted for ~60% of its maximum value over the entire period of our observations. At the local maximum of the star's visual brightness in July 1998, the bolometric flux reached a maximum and was a factor of ~6.2 higher than that in March 1996. If the star's cloud cover is assumed to be without breaks, then the luminosity of V4334 Sgr at this time can be said to have reached $\sim 2 \times 10^4\ L_\odot$.

V4334 Sgr initially began to emerge rapidly from the deep minimum in October 1998 (Fig. 1). However, judging by the observations of amateur astronomers (http://www.kusastro.kyoto-u.ac.jp/vsnet), a complete emergence did not occur. In March 1999, we detected a second deep minimum in the star's optical brightness. The rightmost asterisk in the (*B–V*, *V*) diagram (Fig. 2) corresponds to it. There are no more positive optical-brightness estimates for the star, although it has always been within observers' view. In particular, it was continuously monitored at the Crimean Station of the SAI, where it could be recorded if its visual brightness rose to 17^m.

The infrared brightness of V4334 Sgr also declined, though not so much as in the visual band, and the star reddened appreciably (Figs. 1 and 2). We see from Table 1 that the amplitude of the infrared-brightness decline decreases abruptly with increasing wavelength and becomes zero in the *M* band. Accordingly, we can assume that the star's *N* brightness did not change either, and its estimate in 1998 can be used to calculate the bolometric flux. On April 30, 1999, it accounted for ~76% of its value at the deep minimum in October 1998 (JD 2451094, 2451299 in Table 2). By the end of 1999, it had decreased by a further ~10%. In general, however, the bolometric magnitude of V4334 Sgr in 1999 can be said to have been virtually constant (Fig. 1, Table 2).

Thus, four well-defined stages can be identified in the photometric behavior of V4334 Sgr in 1996–1999. At the first stage (1996), there was no dust in the stellar envelope, and, accordingly, there was no infrared excess in its spectral energy distribution. Its visual brightness slightly rose, and it reddened in the entire observed spectral range. The bolometric flux also gradually, almost linearly increased.

At the second stage (1997), an optically thick dust envelope condensed around the star, which, however, essentially did not manifest itself at optical wavelengths. The bolometric flux continued to rise through an increase in the star's infrared brightness alone, i.e., through an increase in the infrared excess. The rate of rise in the bolometric flux also increased.

At the third stage (1998–March 1999), V4334 Sgr entered the R CrB phase. First two shallow minima and then two deep minima were observed optically. The star reddened appreciably during the deep minima. The bolometric flux ceased to rise. Its mean value in 1998 remained at the level of late 1997, while its peak-to-peak variability amplitude was ~50% of the mean. It decreased to the level of early 1997 at the second deep minimum.

At the fourth stage (March 1999–up until now), V4334 Sgr has been at a protracted deep minimum, which is atypical of the R CrB stars. The variability amplitude of its *K* brightness is $\sim 0\overset{m}{.}3$. The bolometric flux from March through October underwent no significant variations.

DISCUSSION

V4334 Sgr and FG Sge belong to the same group of stars called born again red giants. The nonstationary dust formation in the envelope of FG Sge, which entailed the emergence of a sequence of deep minima in its visual light curve, began in 1992 and, accordingly, has been studied adequately (Tatarnikov *et al.* 1998; Tatarnikov and Yudin 1998). It therefore makes sense to compare the behavior of V4334 Sgr with that of FG Sge during our discussion.

Before the onset of dust formation, i.e., by the end of the first stage, V4334 Sgr and FG Sge did not differ markedly in appearance from each other. They were classified as *F–G* supergiants with an enhanced carbon abundance ($C/O \geq 3$) in their atmospheres [see Asplund *et al.* (1999) and references therein]. However, whereas

the first stage in V4334 Sgr took about two years, in FG Sge it lasted for more than 100 years. It can also be said that the state of FG Sge was virtually the same ten years before the onset of the R CrB stage, so its transition to this stage proved to be completely unexpected. At that time, it pulsated with a period of ~120 days (Arkhipova 1994), with an amplitude of its bolometric-magnitude variations being $\sim 0\overset{m}{.}25$ (Fig. 4).

There has apparently been no second stage in the evolution of FG Sge, although, strictly speaking, this does not follow from observations, because there was a ~9-month-long break in its infrared photometry before the onset of the third stage in August 1992 (Tatarnikov *et al.* 1998). In the model of circumstellar-envelope formation from continuously condensing individual clouds, until such a cloud falls on the line of sight and produces a profound visual fading of the star, the bolometric flux from the object, by which we mean below the star with its dust envelope, can exceed the bolometric flux corresponding to its bolometric luminosity. However, such a situation between the (six) deep visual brightness minima of FG Sge has not been observed so far, although they might have rightly been expected in the above model. In other words, there was no time during the third stage of its evolution when the star would be in a hole of the dust blanket, i.e., when the optical depth on the line of sight [$\tau_{ls}(V)$] would be appreciably smaller than the sphere-averaged optical depth of the dust envelope. The optical depth of the dust envelope averaged over the sphere [$\tau_{av}(V)$] determines its percentage contribution to the object's flux, i.e., the percentage contribution of the infrared excess to the bolometric flux.

The bolometric magnitude of FG Sge increases appreciably at deep minima, returning each time after them to the range of its values recorded during the stellar pulsations at the end of the first stage of its evolution (Fig. 4). By this time, however, the dust envelope still remains optically thick on the line of sight [$\tau_{ls}(V) \geq 1$], reducing the object's visual brightness by no less than 1^m. Collectively, these findings suggest that the circumstellar dust envelope after emergence from a deep minimum appears as a cloud cover without breaks, with $\tau_{ls}(V) \approx \tau_{av}(V)$. In other words, the optical depth of the dust envelope on the line of sight at this time corresponds to the infrared excess taken in the percentage ratio to the bolometric flux. Accordingly, the dust-envelope parameters can be estimated when fitting the object's spectral energy distribution in the model of a spherically symmetric dust shell (Tatarnikov *et al.* 1998).

The local maximum in the optical brightness of V4334 Sgr in July 1998 (JD 2451007 in Table 2), which followed the first two relatively shallow minima (Fig. 1), can be attributed to such a time at the third stage of its evolution. Figure 5 shows the spectral energy distribution for V4334 Sgr at this time, together with the energy distribution computed in the model of a spherically symmetric dust shell. The same is also shown for FG Sge at the time of its emergence from the first deep minimum (JD 2449292). At that time, its bolometric flux returned to its mean value recorded before the onset of the R CrB stage, while the star was fainter visually than it was, on the average, before the onset of this stage by another $\sim 1\overset{m}{.}5$.

We can thus say that the bolometric flux from V4334 Sgr at the local maximum of its visual brightness in July 1998 appears to correspond to the star's bolometric luminosity [$\tau_{ls}(V) \approx \tau_{av}(V)$]. At least, the star can hardly be assumed to have been in a hole of the dust blanket after two successive minima in its visual brightness [$\tau_{ls}(V) < \tau_{av}(V)$]. At the local maximum, the visual brightness of V4334 Sgr was lower than that in 1997, while its bolometric flux was slightly higher (Fig. 1). In other words, the bolometric luminosity of V4334 Sgr in July 1998 estimated from its bolometric flux is its lower limit: $L_{bol} \geq 2 \times 10^4\, L_\odot$. Accordingly, the star's luminosity can be said to have risen by a factor of ~6.2 from March 1996 through July 1998. Note that, when the color excess $E(B–V)$ increases to $0\overset{m}{.}7$ (Pollaco 1999), the amplitude of the rise decreases to ~4.3.

We see from Fig. 2 that, when passing from the first stage to the third one, the rise in the *K* brightness of V4334 Sgr is much larger than that for FG Sge in a similar situation. Definitely, the transition of FG Sge to the R CrB stage was not accompanied by an increase in its bolometric luminosity. Depending on the dust-envelope model, we can only say that its bolometric luminosity either drops or remains constant at deep minima. Accordingly, the rise in its *K* brightness is associated only with the condensation of an optically thick dust envelope, i.e., with the emergence of an infrared excess. Thus, the example of FG Sge clearly shows the extent to which the star can brighten in this band in such a situation. Consequently, it may be inferred from the diagrams in Fig. 2 that the transition of V4334 Sgr from the first stage to the third one must have been accompanied by an appreciable increase in its bolometric luminosity, which occurred mainly at the second stage after the outburst evolution, This, in turn, implies that the dust envelope was a cloud cover without breaks at this stage as well [$\tau_{ls}(V) \approx \tau_{av}(V)$].

Figure 6 shows the spectral energy distribution for V4334 Sgr in June 1997 (JD 2450624 in Table 2), together with the energy distributions computed in the model of a spherically symmetric dust shell (M1) and of the same shell but with a hole on the line of sight (M2). We see from this figure that it is difficult to prefer one of these two computed curves from the viewpoint of fitting quality. In model M2, the star's bolometric luminosity no longer corresponds to the bolometric flux. In this case, it is a factor of ~1.6 lower than that in model M1. In turn, the bolometric flux from the dust envelope ($F_{d,\,bol} \approx 0.5F_{bol}$) specified in model M2 is achieved through an appreciably increase in its optical

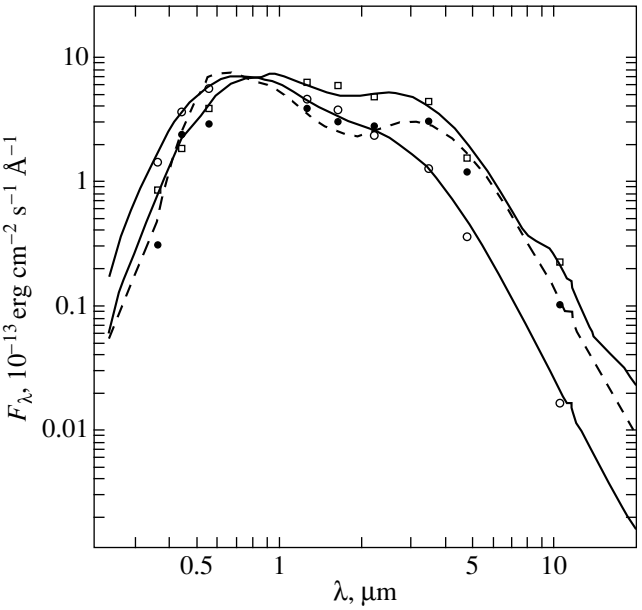

Fig. 5. The spectral energy distributions for V4334 Sgr in June 1997 (circles) and July 1998 (squares) and for FG Sge in November 1993 (dots). The lines indicate computed energy distributions.

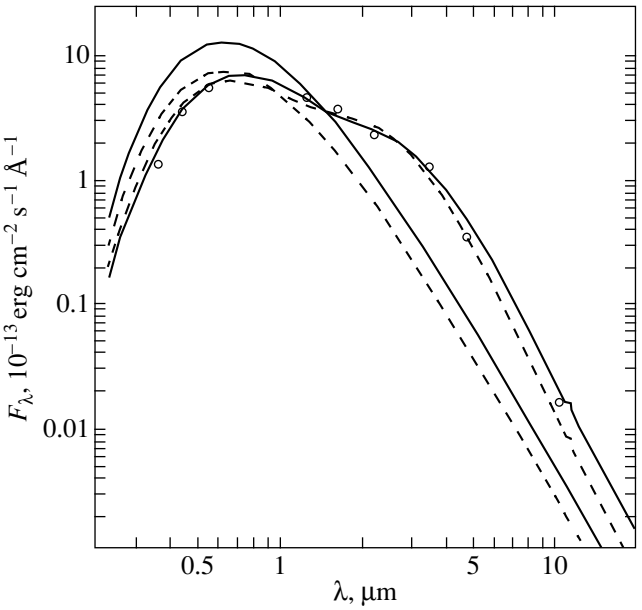

Fig. 6. The spectral energy distribution for V4334 Sgr in June 1997 (circles). The solid lines represent the energy distribution computed in the model of a spherically symmetric dust shell and the star's spectral energy distribution. The dashed lines represent the energy distribution computed in the model of a spherically symmetric dust shell with a hole on the line of sight and the star's spectral energy distribution in this model.

depth: $\tau(V) \approx 1.05$ and 2.5 in models M1 and M2, respectively. Note that the envelope optical depth in a hole on the line of sight in model M2 is $\tau_{ls}(V) \approx 0.3$.

The bolometric flux from V4334 Sgr rose between June and November 1997 by a factor of ~1.5 (Table 2), and, as was already noted above, this rise was caused by a rise in the infrared flux alone, i.e., by an increase in $F_{d, bol}$. In model M2, the observed rise in the star's infrared brightness cannot be reproduced without changing its bolometric luminosity but only increasing the optical depth of the dust envelope. For example, when $\tau(V)$ increases from 2.5 to 4, the object's K brightness in model M2 does not change, while the bolometric flux from the dust envelope $F_{d, bol}$ increases by a mere ~15%. In addition, the computed spectral energy distribution for V4334 Sgr at such a significant $\tau(V)$ differs markedly from the observed one.

Thus, in order to reproduce the rise in bolometric flux from June through November 1997 in model M2, we have to increase the star's bolometric luminosity, as in model M1. Besides, the model of a dust envelope with a single hole on the line of sight persisting for almost one year is clearly unrealistic. At the same time, by introducing additional breaks in it, we have to increase the star's bolometric luminosity to reproduce the observed infrared excess and simultaneously to increase the optical depth of the dust envelope on the line of sight to maintain the object's V brightness.

For example, if holes in the dust blanket occupy ~40% of its area, then we must raise the star's bolometric luminosity to the level of model M1 in order to reproduce the observed infrared excess and simultaneously increase the optical depth on the line of sight to the level of this model in order to maintain the object's V brightness. However, the star's observed spectral energy distribution can no longer be reproduced in such a model with dust clouds covering ~60% of the sphere. For this to be done, we must "spread" them over its entire surface. This will reduce their optical depth but maintain the infrared excess. Clearly, the set of these transformations will eventually lead us to model M1 of a cloud cover without breaks with $\tau_{ls}(V) \approx \tau_{av}(V)$.

Arkhipova *et al.* (1999) pointed out that, in two-color (U–B, B–V) and (B–V, V–R) diagrams, V4334 Sgr moved along the line of normal colors for supergiants at the first stage of its evolution and along the normal reddening line rather than along the line of normal colors for carbon stars at the second stage. In other words, this just implies the absence of a hole in the dust cloud cover on the line of sight.

The B–V color index of FG Sge decreases appreciably on the descent to minimum light; i.e., the star becomes bluer. If this phenomenon is associated with the structure of the dust envelope, then it is a dust blanket with holes [see Tatarnikov and Yudin (1998) for more detail]. No such phenomena have been observed in V4334 Sgr. As was noted above, it started to redden at optical wavelengths from the very beginning of its profound fading in August 1998. However, no such appreciable reddening as one might expect for the condensation of fine graphite grains has been observed. Recall that, as the star's visual brightness declined, the value of R increased from $R \approx 4.3$ at its beginning to

$R \approx 7$, when the visual brightness dropped by $\sim 6\overset{m}{.}5$. At the same time, $R < 2.2$ for fine graphite grains. In this case, when A_V increases by $\sim 6\overset{m}{.}5$, the increase in $B–V$ is $\sim 3^m$, whereas its observed value was $\sim 1\overset{m}{.}2$ (Table 2). Note that no appreciable reddening is observed during dust condensation in the envelope of FG Sge and in the envelopes of classical novae either. Its absence implies that a dust shell (cloud) condenses in such a way that its optical depth throughout this process is determined by large (~0.1 μm) grains.

In Fig. 5, the spectral energy distributions for V4334 Sgr in June 1997 and July 1998 were computed in the model of a spherically symmetric dust shell (a cloud cover without breaks) consisting of graphite grains 0.05, 0.1, and 0.25 μm in size. Their percentage by particle number (by mass) is 85(25), 14(32), and 1(43)%, respectively. We performed such calculations for FG Sge; thus, a fairly detailed description of their scheme and a justification of precisely this choice of the set of grains by their sizes can be found in Tatarnikov *et al.* (1998). An important feature of this model is that we can vary the star's optical reddening over a wide range, starting from its complete absence, by varying the percentage of fine grains.

It should be noted that we cannot accurately determine the percentage of fine grains for each specific spectral energy distribution of V4334 Sgr, because we do not know the precise $B–V$ color index of the star itself. However, their percentage can be estimated from its change. The $B–V$ color index in July 1998 exceeded its observed value in June 1997 (JD 2450624 and 2451007 in Table 2) by $\sim 0\overset{m}{.}35$. For the specified grain size distribution, its computed increase is $\sim 0\overset{m}{.}25$, so $\sim 0\overset{m}{.}1$ can be attributed to the star's cooling. At the same time, all its increase can be attributed to an increase in the dust-envelope optical depth by increasing the percentage of fine grains and to the star's cooling by decreasing it.

Note that, if the dust envelope contains only graphite grains with sizes ≤0.05 μm, then the $B–V$ color index will increase by $\geq 0\overset{m}{.}5$. However, a much larger discrepancy between the observed increase in $B–V$ and its increase in the model of a dust envelope with ≤0.05-μm grains shows up at a deep minimum (as discussed above). At the same time, a dust envelope consisting of 0.05-, 0.1-, and 0.25-μm grains with their percentage given above allows the computed increase in $B–V$ to be reconciled with its observed increase during the first deep minimum.

From June 1997 through July 1998, the optical depth of the dust shell, its inner and outer radii, and its mass increased by a factor of ~2.2, ~2.0, 2.3, and ~10, respectively. In July 1998, these parameters were $\tau(V) \approx 2.3$, $R_{\mathrm{d,\,in}} \approx 7.4 \times 10^{14}$ cm, $R_{\mathrm{d,\,in}}/R_{\mathrm{d,\,out}} \approx 0.7$ ($R_{\mathrm{d,\,in}}/R_* \approx 47$), and $M_{\mathrm{dust}} \approx 1.6 \times 10^{-7}\, M_\odot$ ($D = 5.5$ kpc). It should be noted that the N and L magnitudes of V4334 Sgr decreased within a year after April 1997 by $\sim 2\overset{m}{.}9$ and $\sim 1\overset{m}{.}5$, respectively. In other words, the star's brightness rise near $\lambda = 10$ μm was much larger than that at shorter wavelengths (Fig. 5). This situation can be reproduced only by assuming that silicate grains with an emission feature near $\lambda = 10$ μm emerged in the stellar envelope during this period. In the computed spectral energy distribution for V4334 Sgr in July 1998, fine (≤0.025 μm) silicate grains contribute ≤5% to the optical depth of the dust envelope in the V band, but their radiation is noticeable near $\lambda = 10$ μm. In other words, if we remove silicate grains from the star's envelope model, then this will show up in the object's spectral energy distribution in the disappearance of the silicate emission feature, and it will become similar to the spectral energy distribution of FG Sge in its vicinity (Fig. 5).

An important peculiarity of the dust envelope whose optical depth is determined mainly by medium- and large-sized grains is its high albedo. In the described envelope model, it contributes ~25% to the total V flux from V4334 Sgr in June 1997; in July 1998, its contribution increases to ~38%. We therefore cannot associate a deep minimum in the star's visual light curve with the emergence of a dust cloud on the line of sight in this model of the dust envelope. No deep minimum is possible for such an envelope, because, by blocking the star's direct radiation, we will see it only slightly weakened in reflected light.

We see from Table 2 that the bolometric flux from V4334 Sgr decreased by a factor of ~1.3 from October 1998 through April 1999 and by another ~10% by the fall. Since the stellar radiation contributed only a few percent to the object's flux at these times, the same is also true for its bolometric luminosity. This, in turn, implies that the star's bolometric luminosity has decreased appreciably (by a factor of ~2.4) since the local maximum in July 1998 and returned to its value observed in early 1997.

The He I λ1.08 μm absorption line whose intensity rose during the entire year appeared in the spectrum of V4334 Sgr in March 1998 (Eyres *et al.* 1999), while in March 1999 it was in emission (Geballe *et al.* 1999). At this time, the star was embedded in a dense dust envelope. Given the unprecedented rate of its evolution along the post-AGB track backward after the outburst and the hydrogen depletion in its atmosphere, we can assume that, having reached the turnoff point and having ejected the remnants of its atmosphere above the active helium shell source, it again became hot enough. However, to make sure that this is the case requires an optical spectrum of V4334 Sgr.

CONCLUSION

(1) Having flared up in the second half of 1994, V4334 Sgr passed through four (in particular, photometrically) well-defined stages of its evolution along the post-AGB track backward during its intensive observations in 1996–1999. The star's bolometric luminosity rose at the first two stages; the rate of its rise increased appreciably at the second stage. The rise ceased at the third stage; this can be said to have occurred abruptly. At the fourth stage, the star's bolometric luminosity began to decrease, and the He I λ1.08 μm emission line appeared in its spectrum. Since the rise in luminosity was caused by atmospheric expansion of V4334 Sgr, its fairly abrupt halt can be said to be attributable to the same abrupt cessation of the atmospheric expansion. In our view, such a course of events can be understood by assuming that the mass of the envelope overlying the flashed helium shell source is sufficiently small that it was virtually completely ejected by stellar wind within five years after the outburst evolution.

According to our calculations, the dust-envelope mass in October 1998 during the first deep minimum was $\sim 2.5 \times 10^{-7}\ M_\odot$. Given that the carbon abundance accounts for ~10% of the helium abundance and exceeds the abundances of the remaining elements, including hydrogen (Asplund *et al.* 1999), and assuming that all carbon condensed into dust grains, we find a lower limit on the mass of the part of the gas envelope containing dust to be $\sim 3 \times 10^{-6}\ M_\odot$. If the gas layer overlying the helium shell source (stellar atmosphere) is assumed to have been ejected by now, its mass must be of the order of the above value. The small mass of this layer can, in principle, suggest that the degenerate core of V4334 Sgr is fairly massive. This, in turn, is consistent with the high rate of stellar evolution after the outburst.

(2) In the model of a dust envelope representing a cloud cover without breaks and containing graphite grains 0.05, 0.1, and 0.25 μm in size, the photometric behavior of V4334 Sgr can all be reproduced since the onset of envelope condensation. This is also true for the deep minima in its visual light curve and for the observed increase in *B–V*. However, if the envelope contains such fairly large grains, then it has a high albedo, and this, in turn, implies that the deep minima can in no way be associated with the formation of a single cloud on the line of sight. If the star's direct radiation is blocked, then it will appear fairly bright in reflected light. Lest this occur, the graphite grain sizes must be ≤0.02 μm. However, the increase in the star's reddening at a deep minimum must then be appreciably larger than it actually is. Formally, it remains possible that grains in the dust cloud rapidly grow to large sizes and are subsequently destroyed for some reasons, so the dust blanket itself contains fine grains.

Classical novae give a clear example of the formation of a dust envelope at the so-called condensation radius, i.e., at such a distance from the star at which the temperature of seed grains ≤1500 K. Dust condensation in their envelopes does not differ in all photometric characteristics from similar processes in the envelopes of V4334 Sgr and FG Sge. Based on model calculations of grain condensation, Goeres and Sedlmayr (1992) showed that the deep minima in the light curves of R CrB stars could be associated with the formation of another dust shell in which the grains at the time of their condensation have a temperature ≤1500 K.

(3) We computed the dust-envelope parameters for V4334 Sgr in the model outlined in Section 2 for the following Julian dates: JD 245624, 701, 860, 1007, and 1094 (Table 2). The dust-envelope mass in this time interval, i.e., during 1997–1998, was found to have increased almost linearly: $M_{\rm dust} \approx (0.44t + 263) \times 10^{-9}\ M_\odot$, where t = JD–2450000. Knowing the dust density, say, at the inner radius of the dust envelope, taking into account its chemical composition (see Section 1), and assuming that all carbon has condensed into dust grains and that the envelope expansion velocity is 50 km s^{-1}, we can estimate the mass loss rate. In June 1997, it was $\dot{M} \approx 3 \times 10^{-7}\ M_\odot\ {\rm yr}^{-1}$.

It is clear, however, that this mass loss rate in our model must refer to a much earlier time. This time can be estimated by dividing the inner radius of the dust envelope by its expansion velocity. We found it to be ~2.5 years. Thus, the above estimate of the mass loss rate for V4334 Sgr refers to early 1995, when its visual magnitude was ~12^m. In accordance with the dust-envelope parameters estimated for October 1998, $\dot{M} \approx 9 \times 10^{-7}\ M_\odot\ {\rm yr}^{-1}$, and this estimate of the mass loss rate refers to the mid-1996. It can be inferred from the time dependence of the mass loss rate constructed for 1995–1996 that it appears to have stabilized in late 1996. In that case, the atmospheric mass of V4334 Sgr has decreased by now by $\leq 5 \times 10^{-6}\ M_\odot$. For obvious reasons, this estimate of the total mass loss by the star since its outburst slightly exceeds its estimate in Section 1.

(4) The constancy of the visual brightness of V4334 Sgr at the second stage of its evolution (1997) cannot be explained by the presence of a hole in the dust envelope on the line of sight over this entire period. As yet, we have no reason to believe that there are preferred directions in which V4334 Sgr ejected a considerably larger amount of matter during its evolution after the outburst. It would therefore be strange enough to suggest, even at first glance, that dust clouds, while condensing virtually in all directions (large infrared excess), did not fall on the line of sight during the entire 1997, while during the next year they fell on this direction four times in a row, with the condensation of dust clouds along the line of sight becoming constant after the second deep minimum in March 1999.

ACKNOWLEDGMENTS

We are grateful to the referee for critical remarks.

REFERENCES

1. V. P. Arkhipova, Pis'ma Astron. Zh. **22**, 828 (1994) [Astron. Lett. **22**, 743 (1996)].
2. V. P. Arkhipova, V. F. Esipov, R. I. Noskova, *et al.*, Pis'ma Astron. Zh. **24**, 297 (1998) [Astron. Lett. **24**, 248 (1998)].
3. V. P. Arkhipova, R. I. Noskova, V. F. Esipov, and G. V. Sokol, Pis'ma Astron. Zh. **25**, 711 (1999) [Astron. Lett. **25**, 615 (1999)].
4. M. Asplund, B. Gustafsson, D. L. Lambert, and N. K. Rao, Astron. Astrophys. **321**, L17 (1997).
5. M. Asplund, B. Gustafsson, N. K. Rao, and D. L. Lambert, Astron. Astrophys. **332**, 651 (1998).
6. M. Asplund, D. L. Lambert, T. Kipper, *et al.*, Astron. Astrophys. **343**, 507 (1999).
7. T. Geballe, S. Eyres, A. Evans, and B. Smalley, IAU Circ., No. 7159 (1999).
8. V. P. Goranskiĭ, private communication (1998).
9. A. Goeres and E. Sedlmayr, Astron. Astrophys. **265**, 216 (1992).
10. B. T. Draine, Astrophys. J., Suppl. Ser. **57**, 587 (1985).
11. H. W. Duerbeck and S. Benetti, Astron. J. **468**, L111 (1996).
12. H. W. Duerbeck, S. Benetti, A. Gautschy, *et al.*, Astron. J. **114**, 1657 (1997).
13. I. Iben, Astrophys. J. **277**, 333 (1984).
14. S. P. S. Eyres, A. Evans, T. R. Geballe, *et al.*, Mon. Not. R. Astron. Soc. **298**, L37 (1998).
15. S. P. S. Eyres, B. Smalley, T. R. Geballe, *et al.*, Mon. Not. R. Astron. Soc. **307**, L11 (1999).
16. H. U. Kaeufl and B. Stecklum, IAU Circ., No. 6938 (1998).
17. F. Kerber, H. Gratl, and M. Roth, IAU Circ., No. 6601 (1997).
18. F. Kerber, J. Koppen, M. Roth, and S. C. Trager, Astron. Astrophys. **344**, L79 (1999).
19. S. Kimesvenger, H. Gratl, F. Kerber, *et al.*, IAU Circ., No. 6608 (1997).
20. W. Liller, M. Janson, H. W. Duerbeck, and A. van Genderen, IAU Circ. No. 6825 (1998a).
21. W. Liller, H. W. Durbeck, A. van der Meer, and A. van Genderen, IAU Circ. No. 7049 (1998b).
22. D. K. Lynch, R. W. Russel, and C. J. Rice, IAU Circ., No. 6952 (1998).
23. D. Pollaco, Mon. Not. R. Astron. Soc. **304**, 127 (1999).
24. Yu. Sakurai, IAU Circ., No. 6322 (1996).
25. A. M. Tatarnikov and B. F. Yudin, Pis'ma Astron. Zh. **24**, 359 (1998) [Astron. Lett. **24**, 303 (1998)].
26. A. M. Tatarnikov, V. I. Shenavrin, and B. F. Yudin, Astron. Zh. **75**, 428 (1998) [Astron. Rep. **42**, 377 (1998)].
27. A. M. Tatarnikov and B. F. Yudin, Pis'ma Astron. Zh. **24**, 359 (1998) [Astron. Lett. **24**, 303 (1998)].
28. G. Jacoby and O. De Marco, IAU Circ., No. 7065 (1998).
29. G. Jacoby, IAU Circ., No. 7155 (1999).

Translated by V. Astakhov

Astronomy Letters, Vol. 26, No. 8, 2000, pp. 520–528. Translated from Pis'ma v Astronomicheskiĭ Zhurnal, Vol. 26, No. 8, 2000, pp. 603–612.

UBVRI Photometry of the Eclipsing Symbiotic System CI Cygni in 1996–1999

E. S. Dmitrienko*

Crimean Astrophysical Observatory, p/o Nauchnyĭ, Crimea, 334413 Ukraine

Received October 28, 1999; in final form, December 27, 1999

Abstract—The *UBVRI* photometry of the eclipsing symbiotic star CI Cyg in 1996–1999 is presented. The system continued to be in quiescence during this period. The shape of the minima in its light curves attributable to eclipses of the compact star with an accretion disk by the red giant is the same as that in 1988–1995. An analysis of our observations and those of other researchers, which span a total of 27 years, has revealed a cyclic variability of the out-of-eclipse photometric properties of CI Cyg on a time scale of about 10.7 ± 0.6 years with the clearest manifestation in the *U–B* color. The fact that the system's out-of-eclipse light variations in *U*, on the one hand, and in *BVRI*, on the other, occur in antiphase suggests that the titanium red giant plays a significant role in this cyclic process. However, with its contribution to the total *U* flux being no larger than 10%, the observed light fluctuations of CI Cyg in this band must be caused not only by variability of the giant but also by light variations of the hot component. The presence of a 10.7-year cycle in the system's active and quiescent states suggests that some precession phenomenon is responsible for it. Precession of the accretion disk, which would cause both the observed brightness of the primary component and the effect of its radiation on the titanium red giant to vary, can serve as an example of such a phenomenon. © *2000 MAIK "Nauka/Interperiodica"*.

Key words: *symbiotic stars*

1. INTRODUCTION

CI Cyg belongs to the symbiotic stars, which have been observed since the end of the past century. Photographic brightness measurements for CI Cyg have been carried out approximately since 1890.

Hydrogen emission lines in the spectrum of CI Cyg were discovered by Cannon (1922) in 1922. TiO absorption bands and numerous emission lines of H, He I, He II, [Fe VII], [O III], and other species were first detected in 1931 by Merrill (1933). The spectroscopic studies of CI Cyg and two similar symbiotic stars, AX Per and BF Cyg, in 1964–1965 allowed Boyarchuk (1969) to show for the first time that these are binary systems containing a cool M5 III giant and a hot low-luminosity star. The system's stellar components are embedded in a fairly dense nebula concentrating to the hot star.

Photometric variability of CI Cyg was discovered by Greenstein (1937). In 1911, the brightness of CI Cyg rose from 12.5 to 10.7 (in photographic magnitudes), and the system stayed in an active state for about 200 days (Hoffleit 1966). Subsequently, nova-like outbursts of CI Cyg were detected in 1937 (Hoffleit 1966), as well as in 1971, 1973, and 1975 (Mattei 1977). Having analyzed visual and photographic observations, Whitney (see Aller 1954) found a 855.25-day period in the light variations of CI Cyg with an amplitude of ~1 mag in the photographic band.

The photometric measurements by Belyakina (1979, 1983) confirmed the existence of this period, which she explained as the orbital period of the binary system. Belyakina (1979) showed that the significant brightening of CI Cyg in 1975 was caused by an outburst of the hot component, and that the deep brightness minimum of the same year resulted from an eclipse of a small hot star surrounded by a gaseous envelope by a cool M4–M6 giant. Such a star must be similar to a hot subdwarf after the nova-like outbursts in 1973 and 1975 (see, e.g., Boyarchuk 1976). Hoffleit (1968) and Puchinskas (1972) also suggested that CI Cyg could be an eclipsing binary.

The currently universally accepted model of CI Cyg is based both on ground-based infrared and visible measurements and on IUE (International Ultraviolet Explorer) ultraviolet observations. According to this model, the observed outbursts of CI Cyg result from changes in the luminosity of its hot component, a compact star with an accreting disklike envelope (see, e.g., Boyarchuk 1976; Lijima 1982; Stencel *et al.* 1982; Kenyon *et al.* 1991). This star was assumed by Kenyon *et al.* (1991) to be a main-sequence dwarf. The spectral type of the giant (cool component) is M5 II (Kenyon and Fernandez-Castro 1987). Apart from these two components, the system has an extended common gas-

* E-mail address for contacts: dmitrien@crao.crimea.ua

eous envelope with intense, high-excitation emission lines (see, e.g., Boyarchuk 1969; Kenyon *et al.* 1991).

The red giant in CI Cyg exhibits various types of photometric variability. Its brightness varies with orbital phase because of the so-called ellipticity effect (Taranova 1987). Strictly speaking, in a close binary system which CI Cyg is, the giant must differ in shape from a regular ellipsoid and must be pear-shaped. The brightness of the red giant also depends on orbital phase because of its heating by radiation from the hot component (Kenyon and Fernandez-Castro 1987; Munari 1989).

The giant in CI Cyg is also characterized by 40–60-day light fluctuations with amplitudes $A(V) < 0.4$ mag and $A(I) < 0.2$ mag in the *V* and *I* bands, respectively (Belyakina 1987). They do not show up in the *U* band. The time scales and amplitudes of these fluctuations are variable. According to the observations by Taranova (1987), they have a period of 37.2 days and an amplitude $A(J) \approx 0.11$ mag in the *J* band. This kind of light fluctuations led Belyakina (1987) to suggest that the giant in CI Cyg belongs to the red semiregular (SR) variables, by the GCVS classification (Kholopov *et al.* 1985). Light variations in these stars may occur on a time scale from 20 to 2300 days or more and with an amplitude from several tenths of a magnitude to several magnitudes.

Here, we present the *UBVRI* photometry of CI Cyg in 1996–1999, which is a continuation of our monitoring of this system since 1990. Particular attention is given to analyzing the color behavior of CI Cyg over a period of about 27 years. To this end, we use the *UBV* observations in 1973–1989 and the *RI* observations in 1982–1989 published by Belyakina (1991, 1992) and our *UBVRI* photometry in 1990–1999.

2. OBSERVATIONS

The observations of CI Cyg in 1996–1999 were carried out with the Helsinki Observatory five-channel photometer–polarimeter attached to the 1.25-m Crimean Astrophysical Observatory telescope (AZT-11). The instrument was described in detail by Korhonen *et al.* (1984). In photometry mode, it allows the stellar radiation to be simultaneously recorded in five spectral bands close to Johnson's standard *UBVRI* system. Observations of standard stars from the lists by Nescel and Chini (1980) and Barnes and Moffett (1979) were used to determine the coefficients of conversion from instrumental magnitudes to standard ones. The sky background was measured quasi-simultaneously with the object by rapid (≈100 Hz) modulation of the flux from two equal apertures; the star with background was observed through one aperture and the background alone through the other aperture. The pure integration time was generally chosen to be from 1 to 20 s. A time resolution from 2.2 to 45 s corresponded to it. In order to take into account atmospheric extinction, we observed comparison stars *A* and 5 from the list by Belyakina (1991). We used 10″, 15″, and 20″ apertures. Our data and the 1990–1995 observations are presented in the table.[1] It contains Julian dates, *UBVR* magnitudes of CI Cyg, errors of the mean (designated as ME), and the errors determined from photon-counting statistics (designated as MS). The *I*-band observations will be published later.

Figures 1 and 2 show the *U*, *B* and *R*, *I* light curves of CI Cyg, respectively. Figures 3 and 4 display the system's *U–B* and *V–R*, *V–I* color curves, respectively. The object's *U* and *V* light curves in quiescence are compared in Fig. 5. The photometry of CI Cyg in 1998 is shown in Figs. 6 and 7. The 1990–1999 and 1973–1989 data were obtained by us (Dmitrienko 1996; this paper) and Belyakina (1991, 1992), respectively. The accuracy of the determined values lies in the range ±0.01–±0.03 mag for *UB* and within ±0.01 mag for *VRI*. The symbol sizes in all figures are larger than the observational errors.

3. RESULTS AND DISCUSSION

In 1996–1999, the symbiotic system CI Cyg was in a quiescent state similar to that observed in 1988–1995. An in the previous years, the *BVRI* light curves of CI Cyg at phases ~0.4–0.6 exhibit a brightness decline by approximately 0.16, 0.26, 0.19, and 0.16 mag, respectively. Belyakina and Prokof'eva (1992) assumed that this fading of the system is produced by a partial eclipse of the giant by the hot component and is a secondary minimum. The large sampling interval of the observations and the photometric variability do not allow the exact times that would correspond to the middle points of these eclipses to be determined. The *U–B*, *B–V*, *V–R*, and *V–I* color indices at primary minimum generally increased on its descending branch and decreased on its ascending branch. The general pattern of *V–R* and *V–I* color variations at phases of about 0.4–0.6 is the same as that at primary minimum. The occasionally observed local jumps in color indices from the general pattern of their variations at minimum light may result from some nonstationarities in the system's gas flows (for example, in mass outflow from the red giant and/or in mass accretion onto the compact star, etc.) and/or may serve as a manifestation of the variability of the red giant itself.

The total brightness variation of CI Cyg observed in 1996–1990 lay in the following ranges: 13.20–11.90, 13.05–12.08, 11.50–10.72, 9.31–8.70, and 7.17–6.93 mag in *UBVRI*, respectively. The depth of the photometric minimum at phases of about 0.9–1.1 attributable to an eclipse of the hot component by the red giant increases from *I* to *U*. Outside these phases, the photometric variability of CI Cyg has a maximum amplitude

[1] The table is published in electronic form only and is accessible at ftp cdsarc.u-strasbg.fr/pub/cats/J (130.79.128.5) or at http://cdsweb.u-strasbg.fr/pub/cats/J.

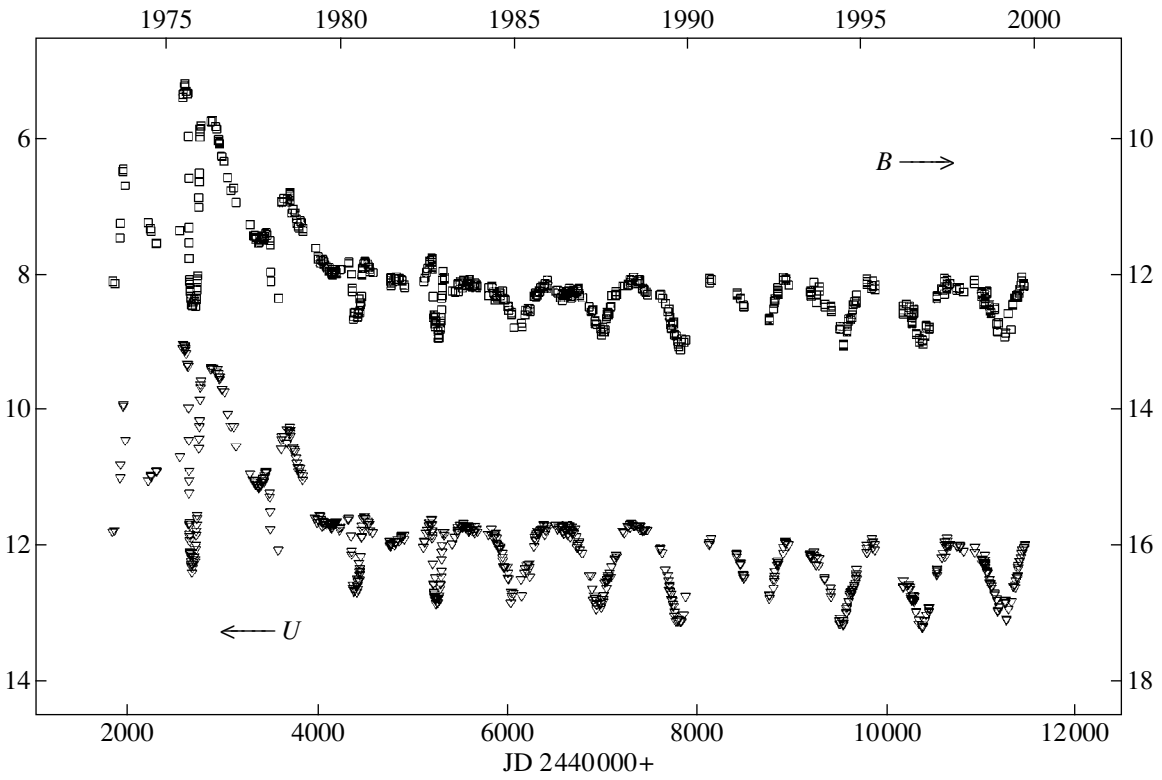

Fig. 1. *U* (triangles and the left *y* axis) and *B* (squares and the right *y* axis) light curves of CI Cyg in 1973–1999. Time on the *x* axis is in Julian days (lower scale) and in years (upper scale).

in *V*. As was noted previously in the case of observations of the system's quiescent state (see, e.g., Belyakina 1987; Taranova 1987; Kenyon and Fernandez-Castro 1987; Munari 1989; Belyakina and Prokof'eva 1992; and Dmitrienko 1996), this variability must be caused by a collection of the phenomena of a possible eclipse of the red giant itself, intrinsic variations of its brightness on a time scale of the order of 37–60 days, as well as the nonspherical shape of the giant and its heating by radiation from the hot component.

74-Day Variability

Figures 6 and 7 show the *UBVRI* light and color curves constructed from our observations in 1998. Time in days is plotted along the lower *x* axis, and time in fractions of the orbital period is plotted along the upper *x* axis. For the convenience of graphically illustrating the system's photometric behavior, the brightness of CI Cyg (Fig. 6) is given relative to magnitudes of 10.62, 10.98, 10.48, 8.20, and 6.02 mag in *UBVRI*, respectively, while its *U–B*, *B–V*, *V–R*, and *V–I* colors (Fig. 7) are given relative to 0.86, 0.30, 0.28, and 2.46 mag, respectively.

We chose the semiannual time interval, because the system's brightness measurements were most frequent compared to other observing seasons. It begins from June 27, 1998, and its duration (in orbital phases) is from 0.70 to 0.92. The brightness declines with orbital phase in all the five bands under consideration. In *BVRI*, however, there are light fluctuations with amplitudes ~0.22–0.25, 0.35–0.41, 0.27–0.29, and 0.15–0.20 mag, respectively, on a time scale $T \approx 75$–78 days against the background of this smooth decline. The duration of one cycle for *V–R* and *V–I* is about 74.3–74.5 days, which matches twice the period of the system's *J* light fluctuations found by Taranova (1987) from an analysis of the 1978–1986 observations.

The light fluctuations reach a maximum amplitude in *V*. They do not show up in *U*. The same features in the behavior of the system's variability amplitude in *UBV* were noted by Belyakina (1987) when analyzing the 1981 and 1983 observations.

The derived different durations *T* of the cycles in the light and color variations of CI Cyg and the large uncertainty in *T* in the former case most likely stem from the fact that, in the observed interval of orbital phases, the photometric variability depends markedly on several factors, whereas only one of them causes the 74-day variation in the system's radiation energy redistribution. Accordingly, the effect of the sampling interval of the observations on the flux in different bands can be considerably larger than its effect on their ratios.

It would be most natural to assume that variability of the red giant in CI Cyg is responsible for the system's light fluctuations observed in 1998. Let us con-

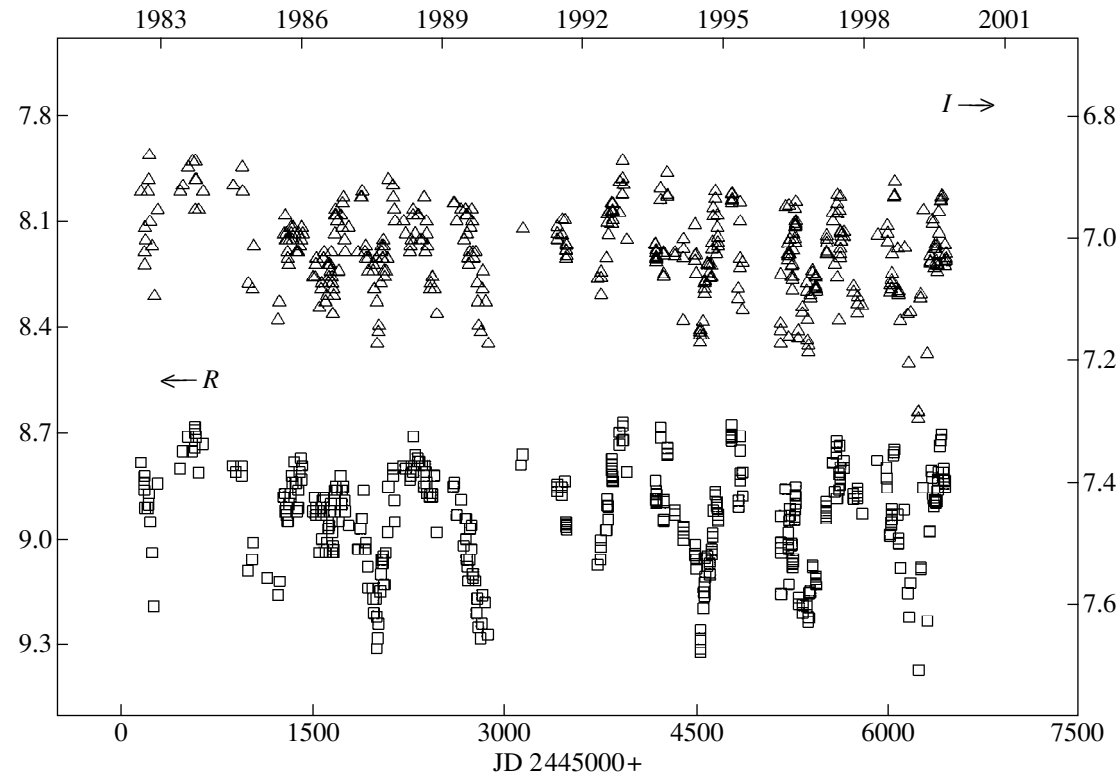

Fig. 2. *I* (triangles and the right *y* axis) and *R* (squares and the left *y* axis) light curves of CI Cyg in 1982–1999. Time on the *x* axis is in Julian days (lower scale) and in years (upper scale).

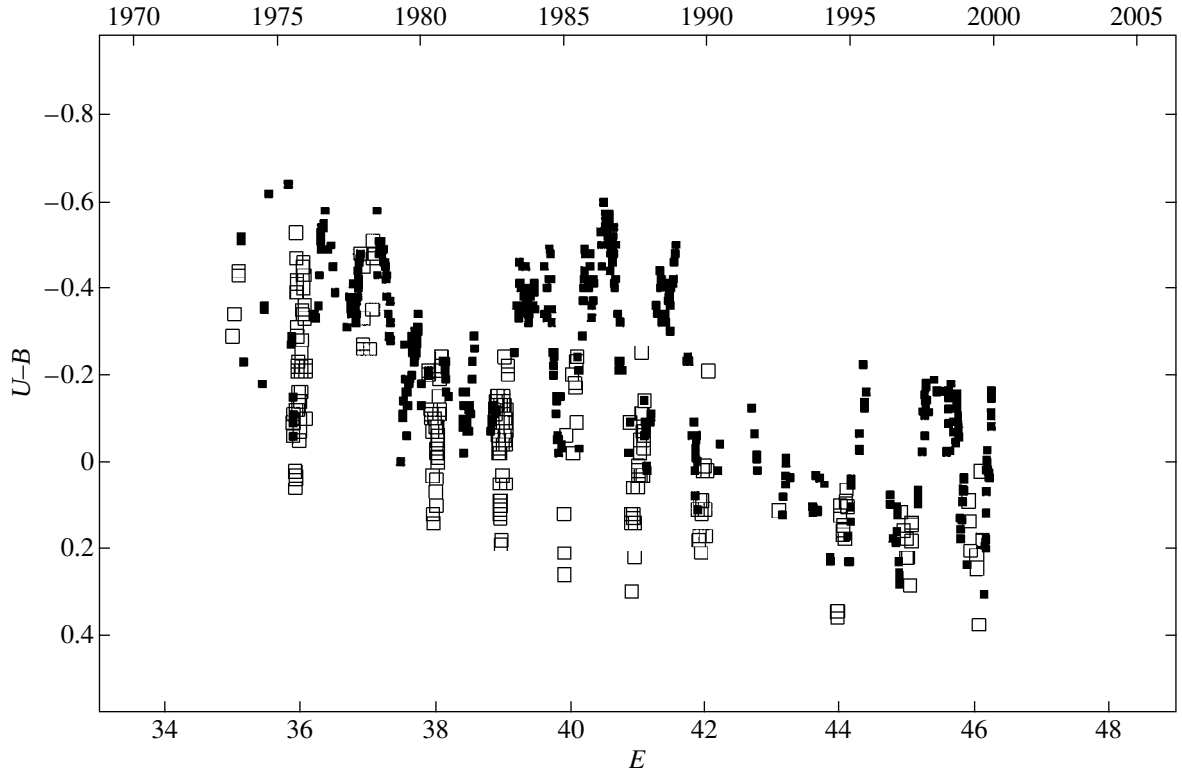

Fig. 3. *U–B* color curve of CI Cyg in 1973–1999 at phases of the primary minimum and outside it (filled symbols). Time on the *x* axis is in orbital cycles *E* with zero epoch at JD 2411902 (lower scale) and in years (upper scale).

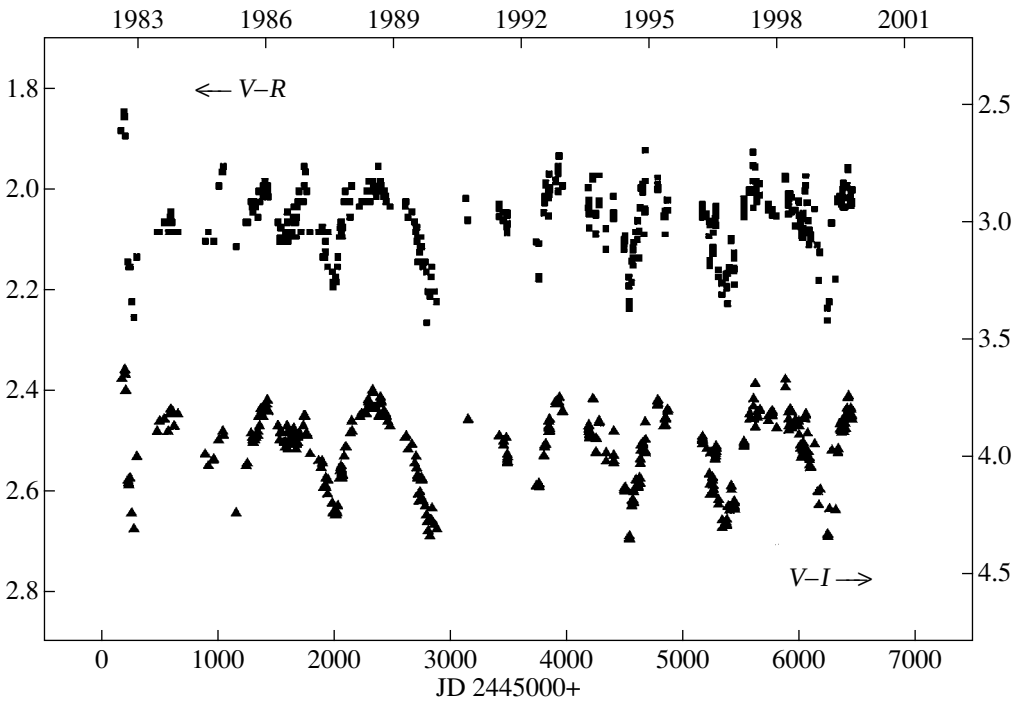

Fig. 4. *V–R* (squares and the left *y* axis) and *V–I* (triangles and the right *y* axis) color curves of CI Cyg in 1982–1999. Julian days (lower scale) and years (upper scale) are along the *x* axis.

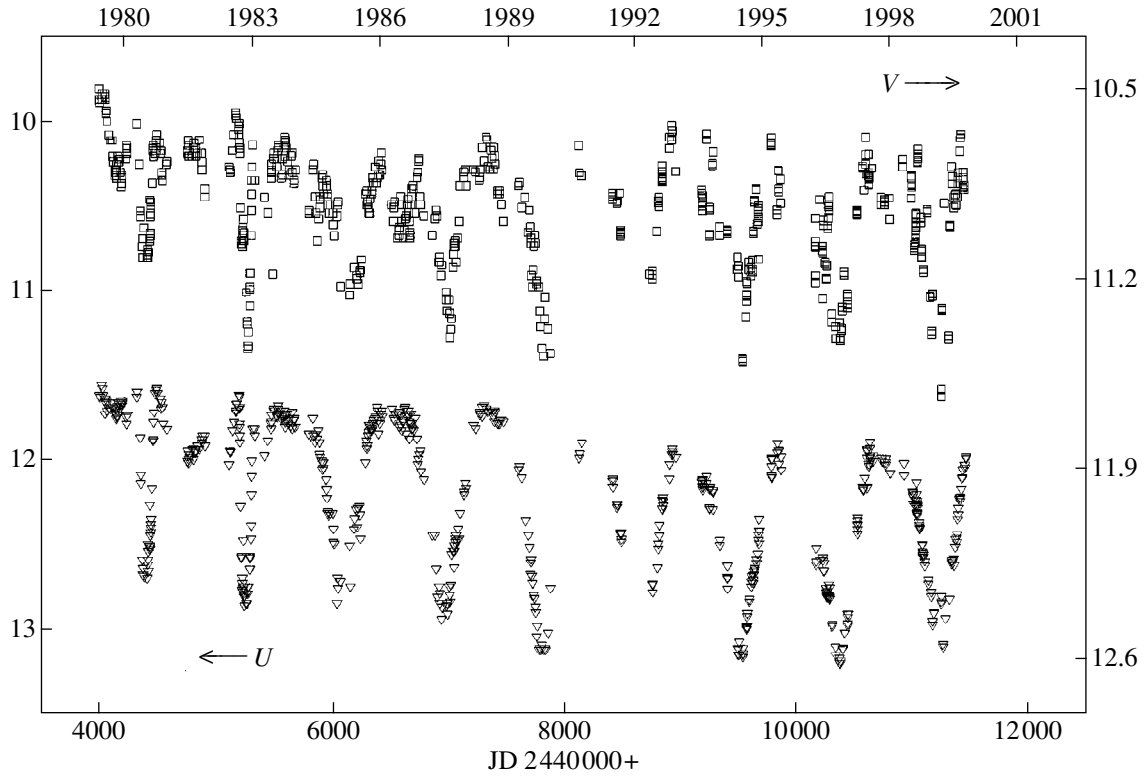

Fig. 5. Comparison of the *U* (triangles and the left *y* axis) and *V* (squares and the right *y* axis) light curves for CI Cyg in quiescence. Julian days (lower scale) and years (upper scale) are along the *x* axis.

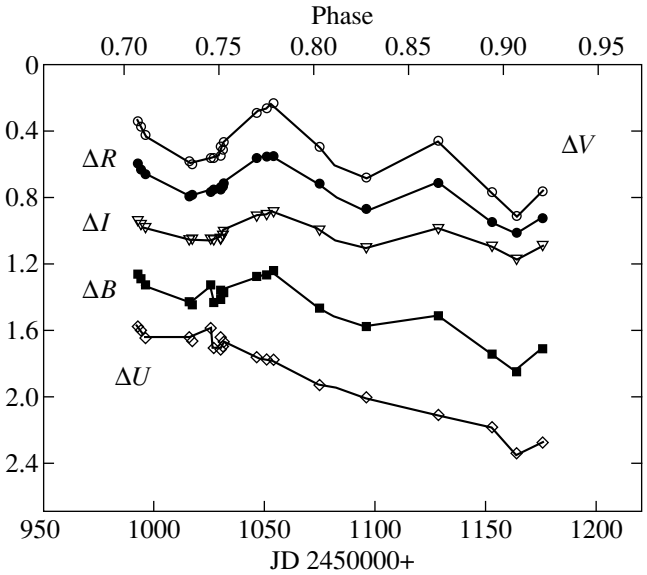

Fig. 6. *UBVRI* light curves of CI Cyg in 1998. Time on the lower *x* axis is in Julian days; phases, in fractions of the 855.25-day orbital period with zero epoch at JD 2411902, are plotted along the upper *x* axis. The brightness of CI Cyg is plotted along the *y* axis relative to 10.62, 10.98, 10.48, 8.20, and 6.02 mag in *UBVRI*, respectively.

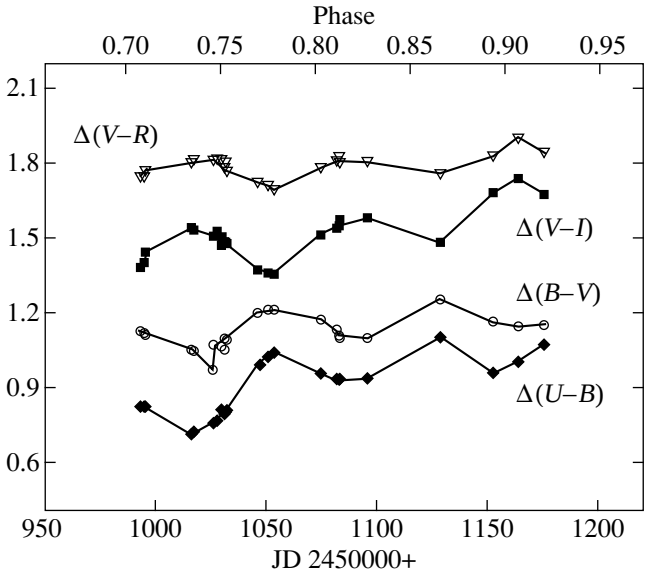

Fig. 7. Color curves of CI Cyg in 1998. Time on the lower *x* axis is in Julian days; phases, in fractions of the 855.25-day orbital period with zero epoch at JD 2411902, are plotted along the upper *x* axis. The *U–B*, *B–V*, *V–R*, and *V–I* colors are plotted along the *y* axis relative to 0.86, 0.30, 0.28, and 2.46 mag, respectively.

sider this issue in more detail. According to the studies by Boyarchuk (1969), the flux from the red giant for the quiescent state of CI Cyg in 1964 accounts for ~2, 57, and 84% of the system's total flux in *UBV*, respectively. Taranova and Yudin (1981) believe the giant in 1978–1980 to have contributed no more than 10% and no less than 85% to the ultraviolet and *R* fluxes from CI Cyg, respectively, while the observed infrared flux from the system belongs to the red giant alone. If the giant is assumed to account for a fraction *Y* equal to 0.57 *L* in *B*, 0.84 *L* in *V*, 0.85 *L* in *R*, and 0.95 *L* in *I* of the total flux *L*, then the fading of the red giant in these bands corresponding to the observed brightness decline in CI Cyg during the 74-day cycle with amplitudes in the above ranges will be about 0.45 ± 0.03, 0.47 ± 0.04, 0.34 ± 0.01, and 0.19 ± 0.03 mag. The *U–B* color index of the giant will decrease by 0.45 ± 0.03 mag, while its *V–R* and *V–I* color indices will increase by 0.13 ± 0.05 and 0.28 ± 0.07 mag, respectively. The amplitude of the *B–V* color variation is insignificant: -0.02 ± 0.07 mag.

The inferred hypothetical pattern of the color behavior of the red giant in CI Cyg is consistent with the universally accepted ideas that the color of a titanium giant is determined by its effective temperature and by molecular TiO-band absorption. The intense TiO bands in the giant's spectrum (Merrill 1933; Boyarchuk 1969) must strongly affect its radiation in *BVRI*. Only the *U* magnitude does not depend on TiO-band absorption. This absorption therefore affects *U–B* more strongly, whereas the effective temperature and absorption have an approximately equal effect on *B–V*. Accordingly, during the cyclic photometric variability observed in titanium giants, the variation of *B–V* with cycle phase must be less significant than that of *U–B*. The *U–B* amplitudes for such stars are of the order of several tenths of a magnitude (see, e.g., Ikaunieks 1971; Smak 1964). As was pointed out by Ikaunieks, Smak, and other researchers (e.g., Alksne *et al.* 1983; Kiseleva 1976), the color curves of semiregular variables have the same pattern as do those of Mira-type stars: for example, *U–B* is bluer, while *V–R* is redder in a fainter state of the star and vice versa. The *U–B* color index is largest at maximum light and smallest at minimum light.

10.7-Year Variability

An analysis of the photometric behavior of CI Cyg and its color behavior outside eclipse in a time interval of about 27 years has revealed yet another type of its variability on a time scale of about 10.7 ± 0.6 years. For the convenience of distinguishing this variability from other types of variations in the system's properties, we call it 10.7-year variability. It should be emphasized here that the number 10.7 refers only to the mean duration (in years) of those two and a half cycles of the system's photometric variations which we detected by using the available 27-year-long observations. How long these cycles will exist and whether they are periodic are the questions of a further monitoring of CI Cyg.

The *U–B* color exhibits particularly pronounced cyclic variations. Their amplitudes reach ≈0.36 (±0.06) mag. Figure 3 shows the *U–B* color curve at primary minima (orbital phases 0.9–1.1) and outside them (filled sym-

bols). The currently available data call into question the possible existence of the system's 10.7-year variability cycle observed at primary minima. This is attributable both to the appreciably larger sampling interval of the observations at orbital phases 0.9–1.1 compared to other factors and to the fact that the light variations at primary minima are mainly determined by the eclipsing effect. At this stage in our study, our assumption about the existence of a 10.7-year variability cycle in CI Cyg therefore refers to segments of the light curve outside the primary minimum. For definiteness, by the term "out-of-eclipse," we mean here only the brightness measured outside this minimum.

The fading of CI Cyg in 1975–1981 after the nova-like outbursts of 1971, 1973, and 1975 is clearly seen in the *U* and *B* light curves and the *U–B* color curve in Figs. 1 and 3. It also clearly shows up in *V*. Since approximately 1982, this effect has been observed only in the general trend of variations toward a reddening of the *U* light and the *U–B* color. By contrast to the *U* band, the effect of post-outburst "cooling" of the system did not show up in the behavior of the *BVRI* light curves after 1981. Moreover, in comparison with 1982–1989, the mean out-of-eclipse *BVRI* brightness of CI Cyg has risen since 1991 by approximately 0.07–0.10, 0.06–0.10, 0.05–0.07, and 0.03 mag, respectively (Figs. 1, 2, 5). Thus, an analysis of the available data leads us to conclude that the observed variability of the system's out-of-eclipse *U* brightness (with a mean amplitude of about 0.25 mag over the entire 27-year period) is accompanied by its smaller variations of opposite sign in *BVRI*. The *U–B* behavior suggests that, despite the complex pattern of variations in the intensity of the radiation from CI Cyg during its nova-like outbursts in 1971–1975, its energy distribution reflects some cyclic process, which is also characteristic of the system's quiescent state. The fact that a dip in the *BVRI* radiation from CI Cyg (see the light curves at JD 2445460–2447460 in Figs. 1, 2, 5) is observed in its brightest state in *U* during 1983–1988 suggests that the red giant may play a significant role in this process. The spectroscopic data from Kenyon *et al.* (1991) may also serve as evidence for this suggestion. In the above period from 1983–1988, the intensity of the observed [O III] λ4363 Å emission from CI Cyg dropped by approximately a factor of 2, while that of the [Fe VII] λ3760 Å emission rose by a factor of 2 or 3. In contrast to the [Fe VIII] line, the [O III] line lies near the head of an intense TiO λ4352 Å absorption band.

The giant under study is a member of a close binary system. Apart from the tidal effect from the hot component, it is also strongly illuminated by the latter, as was mentioned above. Since the part of the red giant's atmosphere responsible for molecular TiO absorption overlies the emission layers, tides and the giant's illumination can primarily affect its absorptivity. The importance of the possible effect of illumination by the hot component on the properties of the red giant (particularly on the properties of the giant's side facing it) in CI Cyg and in similar symbiotic systems has been noted by many researchers. For example, Munari *et al.* (1997) emphasized that such an effect can cause periodic color variations in the giant at its constant bolometric luminosity. Taranova and Yudin (1981) concluded that the possible hot spot in the atmosphere of the giant in CI Cyg resulting from illumination by the companion can significantly affect it, and that this effect will be particularly pronounced in *BVR*. Kenyon and Fernandez-Castro (1987) surmised that the TiO-band intensity variability in the spectra of symbiotic systems, which is observed in many of them over several years, takes place because the red giant is heated by the neighboring star, and that there must be a correlation between the intensity variations of the TiO absorption bands and the *V* radiation in all symbiotic systems. In all likelihood, CI Cyg is one of the first symbiotic stars in which such a correlation has been observed.

Let us consider the possibility that the 10.7-year variability of CI Cyg is the result of some cyclic process in one of the system's components. Assume that the fraction *Y* of the system's total flux *L* accounted for by the giant is ~0.1 *L* in *U*, 0.57 *L* in *B*, 0.84 *L* in *V*, 0.85 *L* in *R*, and 0.95 *L* in *I*. The observed change of the system's brightness by ±0.1, 0.1, 0.07, and 0.03 mag in *BVRI*, respectively, and by ∓0.25 mag in *U* (with the sign opposite to that in *BVRI*) must then be caused either by brightness changes by +0.25/–0.22, +0.87/–0.51, +0.58/–0.40, +0.86/–0.48 mag in *BVRI* and by –0.27/+0.28 mag in *U* in the hot component alone, or by brightness changes by +0.18/–0.17, +0.12/–0.12, +0.08/–0.08, +0.03/–0.03 in *BVRI* and by –1.39 mag in *U* in the red giant alone; in the situation with the *U* band under consideration, i.e., when the giant's contribution to the total flux in this band does not exceed 10%, the system's brightness cannot decline because of the giant's variability alone. If no fading of the hot component occurred, then the fraction of the giant would be more than 20%. At the same time, the brightening of CI Cyg in *U* with its simultaneous fading in *BVRI* and conversely cannot be explained by variability of the hot component alone, whose main radiation is attributable to accretion processes. Consequently, both its components must be involved in the observed 10.7-year photometric cycles of CI Cyg.

Let us estimate the giant's possible light variations in this case. If we assume that 1.5% of the total radiation from the hot component is incident on the giant (Taranova and Yudin 1981) and that the change of its intensity in *U* accounts for ~1.5% of the change in the intensity of the hot component's radiation, then the system's brightening (fading) in this band by 0.25 mag can be caused by the simultaneous brightening (fading) of the giant by 0.19–0.04 mag (0.18–0.03 mag) and of the hot component by 0.11–0.27 mag (0.09–0.28 mag) at $Y = 0.02–0.1$, respectively. The *U* light variations in the red giant under consideration for $Y = 0.1$ are given in the table, where the amplitudes of the light and color variations in the entire system CI Cyg (columns 1 and 3)

Photometric variations of the red giant in CI Cyg during the 10.7-year cycle

Amplitude	CI Cyg	Giant	CI Cyg	Giant
d*U*	0.25	0.03	−0.25	−0.04
d*B*	−0.10	−0.31	0.10	0.50
d*V*	−0.10	−0.12/−0.16	0.10	0.12/0.19
d*R*	−0.07	−0.08/−0.12	0.07	0.08/0.14
d*I*	−0.03	−0.03/−0.04	0.03	0.03/0.05
d(*U*–*B*)	0.35	0.34	−0.35	0.54
d(*B*–V)	−0.00	−0.19/−0.15	0.00	0.38/0.31
d(*V*–*R*)	−0.03	−0.04/−0.08	0.03	0.04/0.11
d(*V*–*I*)	−0.07	−0.09/−0.13	0.07	0.09/0.16

are placed in correspondence with the giant's calculated parameters (columns 2 and 4; all quantities in the table are in magnitudes). These parameters in *BVRI* were determined as follows. Let Y = 0.57, 0.84, 0.85, and 0.95 L in *BVRI*, respectively. Assume that the brightness rise and decline in the hot component occur simultaneously in all *UBVRI* bands with the maximum amplitude A(hot) = 0.27 mag in *UB* and with $0 < A(\text{hot}) < 0.27$ mag in *VRI*. The brightnesses of the giant and the entire system in *U*, on the one hand, and in *BVRI*, on the other, are taken to vary with opposite signs. Here, we do not dwell on the possible existence of phase shifts in the *BVRI* light fluctuations in the giant under study.

The red giant's fading amplitudes of about 0.50, 0.12–0.19, 0.08–0.14, and 0.03–0.05 mag in *BVRI* will then correspond to the observed fading amplitudes of CI Cyg (see the table). The system must brighten in *BVRI* when the giant brightens in these bands by 0.31, 0.12–0.16, 0.08–0.12, and 0.03–0.04 mag. The giant's *B–V*, *V–R*, and *V–I* color changes must lie in the ranges (–0.19)–(–0.15), (–0.04)–(–0.08), and (–0.09)–(–0.13) mag as it brightens and in the ranges 0.38–0.31, 0.04–0.11, and 0.09–0.16 mag as it fades, respectively. In the former case, when the intensity of the giant's radiation increases in *BVRI* and decreases in *U*, its *U–B* color must become redder by 0.49–0.34 mag. In the latter case, when the situation is opposite, it must decrease by 0.69–0.54 mag (for Y = 0.02–0.1, respectively).

The 27-year interval under study contains only two complete cycles with the period of 10.7 ± 0.6 years, and as yet nothing can be said about the stability of this cycle. The involvement of both components in the cycle may be either due to the overall effect of some factor on them or due to internal changes in one of the components, the response to which is the neighbor's variability. A change in which of the components could serve as a trigger for the possible emergence of their common long-term cycle? The presumed light fluctuations in the hot component of CI Cyg (a compact star with a disk accreting onto it) can occur because of some peculiarities of mass transfer and accretion. As was mentioned above, these fluctuations must also affect somewhat the giant, at least its energy distribution through intensity variations of the TiO absorption bands. The giant's possible intrinsic variability as the root cause of the fluctuations in its mass loss rate, which, in turn, may cause variations in accretion onto the compact star, cannot be ruled out either.

On the other hand, the presence of a 10.7-year cycle both during the novalike outbursts associated with variations in accretion and in the quiescent state of CI Cyg suggests that it can be produced, for example, by some precession phenomena in the system. Thus, both the contribution of the hot component to the system's total light and the effect of its radiation on the red giant will change through precession of the accretion disk.

4. CONCLUSION

In 1996–1999, we performed *UBVRI* observations of the eclipsing symbiotic star CI Cyg. They are a continuation of the systematic five-band brightness measurements of this object initiated at the Crimean Astrophysical Observatory in 1982 by Belyakina (1987) and continued by us after 1990. The *UBVRI* photometry in 1996–1999 shows that the system continued to be in quiescence during this period with the same shape of eclipsing minima as that in 1988–1995. The relatively frequent brightness measurements for CI Cyg in 1998 revealed a 74-day cycle in its *BVRI* light variations, which is attributable to variability of the titanium giant. This cycle had not disappear by the fall of 1999 either. How long it will exist is the question of a further monitoring.

The 40–60-day light fluctuations that were first noticed by Belyakina (1987) using the *BVRI* data of 1981 and 1983 and traceable during different periods of observations of CI Cyg (see, e.g., Belyakina's data), as well as the 37-day *J* light fluctuations detected in 1978–1986 by Taranova (1987) and the 74-day variations in the *BVRI* flux from the system that we recorded in 1998, most likely suggest that the light variations in the red giant are not strictly periodic. Their "quasi-periodicity" in combination with measurements differing in frequency and duration produces observed differences between the variability time scales of up to several tens of days.

An analysis of our observations and those of other researchers spanning a total of 27 years has revealed a cyclic process in CI Cyg, which manifests itself in vari-

ations of its out-of-eclipse photometric properties on a time scale of about 10.7 ± 0.6 years. These variations are most pronounced in the *U–B* color. The fact that the system's out-of-eclipse light fluctuations in *U*, on the one hand, and in *BVRI*, on the other, occur in antiphase suggests that the titanium red giant plays a significant role in them. However, with its contribution to the total *U* flux being no larger than 10%, the observed photometric variability of CI Cyg in this band cannot occur without light variations in its primary component. The existence of the cyclic process under consideration in various states of CI Cyg (both during the outburst and tens of years later) suggests that some "geometrical" effect, for example, precession of the disk accreting onto the compact star, is most likely its root cause.

Our analysis of the five-band observations of CI Cyg performed by using published determinations of the relative contributions of the hot component and the giant to the system's total flux allowed us to estimate the possible variations in the photometric parameters of its giant in *UBVRI* both for the light fluctuations on a time scale of several tens of days and for the long-term cycle.

REFERENCES

1. Z. Alksne, A. Alksnis, and U. Dzervitis, *Characteristics of Galactic Carbon Stars* (Zinatne, Riga, 1983).
2. L. H. Aller, Publ. Dom. Astrophys. Obs. Victoria **9**, 321 (1954).
3. T. G. Barnes and T. J. Moffett, Publ. Astron. Soc. Pac. **80**, 165 (1979).
4. T. S. Belyakina, Izv. Krym. Astrofiz. Obs. **59**, 133 (1979).
5. T. S. Belyakina, Izv. Krym. Astrofiz. Obs. **68**, 108 (1983).
6. T. S. Belyakina, Izv. Krym. Astrofiz. Obs. **76**, 40 (1987).
7. T. S. Belyakina, Izv. Krym. Astrofiz. Obs. **83**, 118 (1991).
8. T. S. Belyakina, Izv. Krym. Astrofiz. Obs. **84**, 45 (1992).
9. T. S. Belyakina and V. P. Prokof'eva, Izv. Krym. Astrofiz. Obs. **85**, 62 (1992).
10. A. A. Boyarchuk, Izv. Krym. Astrofiz. Obs. **39**, 124 (1969).
11. A. A. Boyarchuk, *Eruptive Stars* (Nauka, Moscow, 1976).
12. A. Cannon, Bull. Harv. Coll. Obs., No. 778 (1922).
13. E. S. Dmitrienko, Astrofizika **39**, 212 (1996).
14. N. K. Greenstein, Bull. Harv. Coll. Obs., No. 906 (1937).
15. D. Hoffleit, *AAVSO Abstract, October 14-15, 1966* (1966).
16. D. Hoffleit, Ir. Astron. J. **8**, 149 (1968).
17. Ya. Ya. Ikaunieks, *Long-Period Variable Stars* (Zinatne, Riga, 1971).
18. S. J. Kenyon and T. Fernández-Castro, Astron. J. **93**, 938 (1987).
19. S. J. Kenyon, N. A. Oliversen, J. Mikolajewska, *et al.*, Astron. J. **101**, 637 (1991).
20. P. N. Kholopov, N. I. Samus', V. P. Goranskiĭ, *et al.*, *General Catalog of Variable Stars* (Nauka, Moscow, 1985), Vol. 1.
21. T. K. Kiseleva, Bull. Inst. Astrofiz., Akad. Nauk Tadzh. SSR, Nos. 66–67, 60 (1976).
22. T. Korhonen, V. Piirola, and A. Reiz, ESO Messenger, No. 38, 20 (1984).
23. T. Lijima, Astron. Astrophys. **116**, 210 (1982).
24. P. W. Merrill, Astrophys. J. **77**, 231 (1933).
25. J. A. Mattei, J. R. Astron. Soc. Can. **71**, 217 (1977).
26. U. Munari, Astron. Astrophys. **208**, 637 (1989).
27. U. Munari, E. A. Kolotilov, A. A. Popova, and B. F. Yudin, Astron. Zh. **74**, 898 (1997) [Astron. Rep. **41**, 802 (1997)].
28. Th. Nescel and R. Chini, Astron. Astrophys., Suppl. Ser. **39**, 411 (1980).
29. A. Puchinskas, Byull. Vil'nyus. Astrofiz. Obc., No. 33, 50 (1972).
30. J. Smak, Astrophys. J., Suppl. Ser. **89**, 9 (1964).
31. R. E. Stencel, A. G. Michalitsianos, M. Kafatos, and A. A. Boyarchuk, Astrophys. J. Lett. **253**, L77 (1982).
32. O. G. Taranova, Pis'ma Astron. Zh. **13**, 423 (1987) [Sov. Astron. **13**, 173 (1987)].
33. O. G. Taranova and B. F. Yudin, Astron. Zh. **58**, 1051 (1981) [Sov. Astron. **25**, 598 (1981)].

Translated by V. Astakhov

Astronomy Letters, Vol. 26, No. 8, 2000, pp. 529–538. Translated from Pis'ma v Astronomicheskiĭ Zhurnal, Vol. 26, No. 8, 2000, pp. 613–623.

Solving Wolf's *uvbyRI* Light Curves for the Star BM Ori

A. S. Vasileĭskiĭ and É. A. Vitrichenko*

Space Research Institute, Russian Academy of Sciences, Profsoyuznaya ul. 84/32, Moscow, 117810 Russia

Received September 3, 1999; in final form, January 10, 2000

Abstract—We solve the *uvbyRI* light curves obtained by Wolf (1994) with a CCD photometer. Wolf did not solve the light curves, while particular interest in them stems from the fact that a secondary minimum, which other observers failed to detect, is clearly seen in the *byRI* light curves. This enables us to consider a new eclipse model in which we hypothesize that the secondary component at primary minimum completely obscures the primary, smaller B star, but, at the same time, the light from a third star is observed. Based on this hypothesis, we computed the brightness of each of the three stars for the six bands by analyzing the depths of the primary and secondary minima. Satisfactory agreement between theoretical and observed light curves was achieved by assuming the following parameters for the stars: effective temperature T_1 = 17000 K, radius $R_1 = 2.5\ R_\odot$, spectral type Sp_1 = B3–B4 for the primary; T_2 = 5700 K, $R_2 = 8.4\ R_\odot$, Sp_2 = G0–G2 for the secondary; and T_3 = 29000 K, $R_3 = 1.0\ R_\odot$, Sp_3 = B0 for the third star. In the Hertzsprung–Russell diagram, the first star lies on the zero-age main sequence, the second is on the way from the birthline to the main sequence in the region of giants, and the third falls within the region of hot subdwarfs. © *2000 MAIK "Nauka/Interperiodica".*

Key words: *stars—variable and peculiar*

INTRODUCTION

BM Ori is an eclipsing variable star and a member of the Orion Trapezium. Its period is 6.46 days. At present, this is the only Trapezium star for which radial-velocity curves have been constructed for both components, allowing their masses and radii to be determined (Vitrichenko *et al.* 1996). However, there is a problem with brightness estimation for the components, which stems from the fact that the eclipse geometry is not known for certain. A total eclipse lasting 8.5 h is observed, but attempting to assume that the cool secondary component at primary minimum completely obscures the B star leads to a conflict with spectroscopic observations: the spectrum of the B star is seen during totality (Doremus 1970; Popper and Plavec 1976).

The first attempt to construct and solve the light curve was made by Parenago (1947). Using photographic and visual observations, he concluded that the small star passes over the disk of the giant star during minimum light. In this case, the brightness of the small star is $L_2 = 0.01$; i.e., it is 5^m fainter than the primary. Photoelectric observations did not confirm this pattern of eclipse.

Photoelectric observations of the star were obtained, and attempts were made to solve its light curve by taking into account the problem described above. All these attempts were based on the assumption that the secondary component had an exotic nature (Hall 1971). An overview of this issue can be found in Vitrichenko (1998a).

Vitrichenko and Larionov (1996) came up with the idea that one need not attribute peculiar properties to the secondary component but may assume that there is a third light in the system whose source could be the secondary. This idea has not yet been verified, because no good observations have been obtained near the secondary minimum, while such observations are a critical test. The absence of a secondary minimum forces us to assume that the surface brightness of the secondary is similar to that of the primary, or that the eclipse is produced by a dust envelope. The first assumption implies that the secondary is much brighter than the primary, which is in conflict with spectroscopic observations. This hypothesis is also in conflict with the star's observed reddening at primary minimum. The second assumption forces us to introduce the idea of a dust envelope around the secondary component. The presence of a secondary minimum refutes both these assumptions, but forces us to make a different assumption: there is a third star in the system which is not involved in the eclipse (third light). If this star is of spectral type B, then its spectrum is seen during totality, which accounts for the paradox first noted by Doremus (1970).

Recently, three companions have been discovered near BM Ori (McCaugrean and Staufer 1994; Petr *et al.* 1998; Simon *et al.* 1999; Weigelt *et al.* 1999). Since

* E-mail address for contacts: vitrich@nserv.iki.rssi.ru

these stars fall within the photometer aperture during photoelectric observations and within the spectrograph slit during spectroscopic observations, their fluxes must be taken into account in any analysis. It becomes of current interest to consider the eclipse model with a third light in connection with the companions' detection.

Obtaining high-quality brightness measurements for BM Ori is a difficult observational problem for the following five reasons. First, the light curve is unstable, as was pointed out by many authors (Arnold and Hall 1976; Bondar' and Vitrichenko 1995, 1996, 1997; Zakirov and Shevchenko 1982). Second, the background is difficult to measure with a conventional photometer, because the bright Orion Nebula has a clumpy structure. Third, atmospheric extinction fluctuations limit the accuracy of observations (Bondar' and Vitrichenko 1997); besides, the star lies low above the horizon at mid-latitudes because of its negative declination, which reduces the accuracy of photoelectric observations further still. The star is observed in winter, when the photometric nights are few in number, and the seeing is often poor. Fourth, a definitely constant star to be used as a comparison star is difficult to find in the Orion Trapezium region. The last reason is that twice the star's period is almost 13 days (a 13-day star). As a result, a light curve with a uniform distribution of observations in phase cannot be constructed during a single season. One has to observe the star for several years.

Wolf (1994) was the first to observe this star with a CCD photometer; he chose Θ^1 Ori D, which was commonly used by other authors and whose variability was not detected, as a comparison star. In this way, he eliminated the second, third, and fourth reasons. The fifth reason was also eliminated, because the star was observed during several seasons. Thus, only brightness instability of the star itself results in the scatter of observations in its light curve. The principal value of the observations is that a secondary minimum is clearly seen in four of the six light curves, which other observers failed to detect. For the above reasons, Wolf's observations are unique, but he did not solved his light curves.

Here, we set the following objectives: (1) to analyze Wolf's (1994) light curves in an effort to estimate the depths of the primary and secondary minima, (2) to determine the brightness of all three stars using these estimates by hypothesizing the existence of a third light, (3) to compare the observed light curves with the theoretical ones constructed by assuming the existence of a third light and to estimate the system's parameters, and (4) to discuss the nature of the third light.

SOLVING THE LIGHT CURVES

Wolf (1994) presented his observations in the form of *uvbyRI* light curves. The first four and the last two bands refer to Stroemgren's (Straizis 1977) and Cousin's (Bessel 1979) photometric systems, respectively. We scanned and digitized these curves. We rectified the errors attributable to deformation of the curves when printing and coping by using our program.

The light curves were solved in several steps. First, we analyzed the out-of-eclipse brightness. We singled out segments in the light curve that were free from eclipses and calculated the parameters a_0, a_1, and a_2 for these segments by least squares using the conditional equations

$$m = a_0 + a_1\cos\Theta + a_2\cos 2\Theta. \quad (1)$$

Here, m is the observed magnitude relative to the comparison star, a_0 is the mean magnitude outside eclipse, a_1 is the reflection coefficient, a_2 is the ellipticity coefficient, and Θ is the phase.

The results of our calculations are presented in Table 1. Here, the first, second, and third rows give the band, its effective wavelength λ, and the number N of observations, respectively. The next five rows list characteristics of the out-of-eclipse brightness: a_0, a_1, a_2, the error σ_1 of a single measurement, and the number N_0 of observations in the part of the light curve outside eclipse. The error, in units of the last digit, is given in parentheses. The mean reflection coefficient is significant, $a_1 = 0\overset{m}{.}017(2)$; the mean ellipticity coefficient is nearly zero, $a_2 = 0\overset{m}{.}002(2)$.

During our calculations, we rejected some of the observations by using the $3\sigma_1$ criterion. An analysis of outliers shows that most of them are rises in brightness, i.e., flares (Bondar' and Vitrichenko 1996, 1997). Some of the brightness rises lie near the first and fourth contacts, i.e., in the region of "shoulders" (Vitrichenko 1995). An abnormally large σ_1 is observed in the v band, which is also seen from the scatter of observations in the light curve itself (see Fig. 3).

Next, we determined the depths of the primary and secondary minima. We singled out the region in the light curve between the second and third contacts and averaged all measurements in this region. For the primary minimum, Table 1 gives magnitude m_1 at minimum light, number N_1 of observations, and depth Δm_1 of the primary minimum calculated from the formula

$$\Delta m_1 = m_1 - a_0 - a_1 - a_2. \quad (2)$$

For the secondary minimum, Table 1 gives magnitude m_2 at minimum light, number N_2 of observations, and depth Δm_2 of the secondary minimum calculated from the formula

$$\Delta m_2 = m_2 - a_0 + a_1 - a_2. \quad (3)$$

Figure 1 compares the depth of the primary minimum from Table 1 with that from Bondar' and Vitrichenko (1995). The observed discrepancy far exceeds the error limits and can be attributed to a difference between the observing techniques. In general, Wolf's data yield a larger depth of the minimum; therefore,

Table 1. Results of the light-curve solution

Band	*u*	*v*	*b*	*y*	*R*	*I*
λ, μm	0.35	0.41	0.47	0.55	0.64	0.79
N	170	181	196	196	185	186
a_0	1.840(2)	1.429(3)	1.343(2)	1.278(2)	1.178(2)	1.035(2)
a_1	0.015(2)	0.009(3)	0.013(2)	0.017(2)	0.024(2)	0.023(2)
a_2	−0.007(3)	0.007(3)	0.000(2)	−0.003(2)	0.008(2)	0.004(2)
σ_1	0.018	0.021	0.015	0.016	0.016	0.015
N_0	96	115	119	114	120	112
m_1	2.718(5)	2.162(7)	2.033(4)	1.927(5)	1.748(6)	1.549(5)
N_1	19	16	25	20	20	21
Δm_1	0.870	0.716	0.677	0.636	0.538	0.487
m_2	1.810(7)	1.430(7)	1.357(4)	1.294(5)	1.202(4)	1.066(3)
N_2	14	19	21	17	17	14
Δm_2	−0.008	0.004	0.026	0.036	0.040	0.050
L_1	0.551	0.483	0.464	0.444	0.391	0.362
L_2	−0.080	0.041	0.271	0.370	0.406	0.514
L_3	0.529	0.476	0.265	0.186	0.203	0.125

these data are more credible, because systematic errors most commonly reduce the depth of the minimum. The deviation from a smooth wavelength dependence of the depth of the minimum is sharpest in the *v* band. This can be associated with the fact that it is in this band that hydrogen emission lines and oxygen forbidden lines, which originate in the hot gas in the vicinity of the system (McCulough *et al.* 1995), may be located.

The general pattern of behavior for the depth of the minimum with wavelength is confirmed: it decreases with increasing wavelength (Zakirov and Shevchenko 1982), suggesting an increase in the contribution of the cooler (secondary) component to the system's total light. As the wavelength increases further, the depth of the minimum abruptly increases (Vitrichenko 1998b).

DETERMINING L_1, L_2, AND L_3

In our case, the brightness L_i of one of the three stars is given by

$$L_i = F_i/(F_1 + F_2 + F_3), \quad (4)$$

where F_1, F_2, and F_3 are the heterochromatic fluxes from the primary, the secondary, and the third star, respectively. L_i is called brightness (Mikhailov 1962), relative luminosity, or luminosity (Martynov 1977).

We determine the brightness of the stars by solving the set of equations

$$\begin{aligned} L_1 + L_2 + L_3 &= 1, \\ \Delta m_1 &= -2.5\log(1 - L_1), \\ \Delta m_2 &= -2.5\log(1 - k^2 L_2). \end{aligned} \quad (5)$$

The first equation follows from the definition (4). The second equation describes the primary minimum under the assumption that the secondary completely obscures the primary star (the depth of the primary minimum is on the left-hand side of this equation). The third equation describes the secondary minimum. $k = r_1/r_2 = 0.298(8)$ is the ratio of the radii of the primary and secondary stars. (Bondar' and Vitrichenko 1995).

The primary's brightness L_1 was calculated from the second equation in (5). We determined the secondary's brightness L_2 from the third equation in (5) and then used the first equation to calculate the brightness L_3 of the third star. The results of these calculations are presented in Table 1.

An examination of Table 1 leads us to interesting conclusions. We obtained a negative *u* brightness for the secondary component, because the depth of the minimum is negative in this band, but lies within the limits of the measurement errors. In the *uv* bands the primary and third stars make an overwhelming contribution to the system's total light, while in the *I* band the secondary star is brightest. The ratio of the fluxes from the primary and from the sum of the primary and third stars is approximately the same in *byRI*, on the average, 0.69(3). When solving the light curves in terms of an eclipse of two stars or an eclipse by a dust envelope, we therefore achieved good agreement between the theoretical and observed light curves by assuming a maximum eclipse phase $\alpha_0 \sim 0.63(3)$ (Bondar' and Vitrichenko 1995; Vitrichenko 1996).

LIGHT CURVES

Using L_i and other elements of the system [$r_1 = 0.080(2)$, $r_2 = 0.268(2)$, $i = 83^\circ.8(2)$] from Bondar' and Vitrichenko (1995), we constructed light curves for all six bands. An examination of these curves shows that,

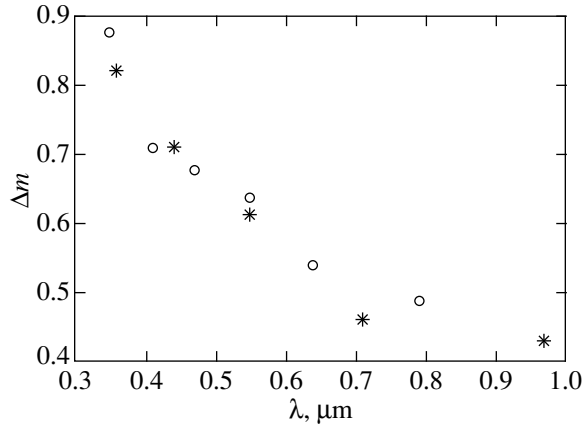

Fig. 1. Depth of the primary minimum versus wavelength. The circles and asterisks represent our data and the data from Bondar' and Vitrichenko (1995).

first, all light curves are displaced from the central eclipse phase by –0.003(1), in fractions of the period, and, second, all light curves satisfy well the light-curve elements after applying this correction. After applying the correction to the phase, we recalculated all the parameters in Table 1, and the table gives their final values.

The systematic correction to the phase is associated with the accumulation of error in the system's elements from Hall and Garrison (1969), which were used by Wolf. Using the more accurate elements from Bondar' and Vitrichenko (1995) yields a correction of –0.005(2) to the phase, in satisfactory agreement with the measured correction to the phase.

Figures 2–7 display the *uvbyRI* light curves as measured by Wolf (1994). An examination of all six light curves shows that the observations are in satisfactory agreement with the theoretical curve constructed in the presence of a third star. We see that the *uv* light curves near the secondary minimum constructed by assuming the absence of a third star disagree with the observations. In the other bands, the observations are consistent with both eclipse models. No secondary minima must be observed in the hypothesis of an eclipse by a dust envelope. The *uv* light curves are consistent with this hypothesis, while the remaining light curves are in conflict with it.

CHARACTERISTICS OF THE SYSTEM'S STARS AND THEIR EVOLUTIONARY STATUS

The photometric data for each of the three stars in Table 1 allow their spectral types to be estimated. We obtained these estimates by fitting the observed flux ratio of the stars with the theoretical ratios constructed by using the colors of main-sequence stars from Straizis (1977).

The fitting results are presented in Figs. 8 and 9. These figures show that the observed flux ratios satisfactorily match the theoretical ones. The largest deviation is observed in Fig. 9 for the *v* band, but the abnormal depth of the primary minimum in this band has already been discussed above. In both cases, the rms deviation of the observed flux ratios from the theoretical ones is 0.08 on the scale of the total *y* flux from the system. This deviation agrees in order of magnitude with the error in the secondary's brightness.

Let us estimate the absolute magnitudes of the components. In the subsequent calculations, we assume the magnitude differences in *y* and *V* to be equal. The effective wavelengths for these bands are the same, the absolute-flux calibrations are also in agreement, and only the band widths differ (Straizis 1977).

The apparent magnitude of BM Ori is $V = 7\overset{m}{.}95(5)$ (Bondar' and Vitrichenko 1995), and the extinction toward this system is $A_v = 0\overset{m}{.}70(5)$ (Vitrichenko and Larionov 1996). The star's unreddened magnitude is then $V_0 = 7\overset{m}{.}95 - 0\overset{m}{.}70 = 7\overset{m}{.}25(7)$. Let us determine the unreddened magnitude of each component from the formula

$$V_0^i = V_0 - 2.5\log L_i. \quad (6)$$

We took the values of L_i from Table 1 for the *y* band. The components' magnitudes calculated from (6) are given in Table 2. The numbers 1, 2, and 3 in the first row of this table denote the primary, the secondary, and the third star, respectively. The bolometric absolute magnitude was calculated for the distance modulus $m - M = 8\overset{m}{.}2$ (Van Altena *et al.* 1988).

Solving the radial-velocity curve and the light curve yields highly accurate radii of the primary and secondary stars (Vitrichenko *et al.* 1996). We calculated the temperatures of the primary and the secondary by using the well-known formula (Martynov 1977)

$$M_b = 42.31 - 5\log R - 10\log T. \quad (7)$$

The results of our calculations are presented in Table 2. The primary's temperature was found to be lower than follows from its spectral type; however, the difference is not large and can be attributed to errors in the light-curve solution. $T_{\rm eff}$ = 17000 K for the primary star, which, according to the tables from Straizis and Kuriliene (1981), corresponds to the spectral type B4. The temperature for the secondary turned out to be considerably lower than that under other assumptions about the pattern of eclipse. $T_{\rm eff}$ = 5700 K for this component, which corresponds to the spectral type G2. These estimates of the spectral types for the primary and the secondary are in good agreement with the spectral types determined by fitting the stars' flux ratios (Figs. 8 and 9). Previously, the spectral types of the primary and secondary stars have been assumed to be B3 and F2, respectively (Vitrichenko 1996).

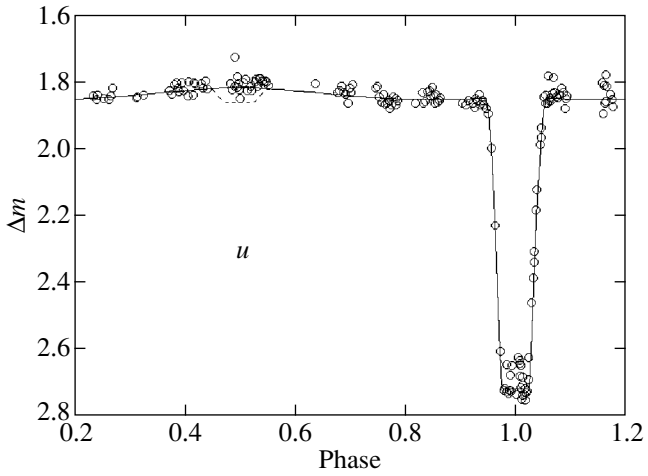

Fig. 2. The *u* light curve of BM Ori. The phase corrected for a systematic error of –0.003 is plotted along the *x* axis, and the magnitude difference relative to the comparison star Θ^1 Ori D is plotted along the *y* axis. The circles indicate our observations, and the solid line represents a theoretical light curve for the case where the secondary obscures the B star (total eclipse) and both the secondary and the third star emit radiation during totality. The dashed line near the secondary minimum indicates a theoretical light curve for the case where two stars are involved in the eclipse, while the third star is absent.

The radius for the third star is not known. Let us estimate it from formula (7) by assigning the temperature to this star that was obtained for V1016 Ori of the same spectral type (Vitrichenko and Klochkova 2000). The radius was found to be abnormally small, $R_3 = 1\ R_\odot$. This is difficult to explain, but this kind of problem has repeatedly been raised when studying BM Ori and V1016 Ori (Bossi *et al.* 1989).

Figure 10 shows the Hertzsprung–Russell diagram. It turns out that the primary star lies on the zero-age main sequence (ZAMS), and the secondary star is located near the birthline on the way to the main sequence in the region of giants. The third star falls within the region of hot subdwarfs. Such objects are commonly encountered at high Galactic latitudes. They were first discovered by Humanson and Zwicky (1947). In the opinion of Gurzadyan (1993), they are related to planetary nebula nuclei.

The figure shows the isochrone with $t = 3 \times 10^5$ years, which is taken as the age of the entire Orion Trapezium complex. The secondary's position closely coincides with this isochrone, while the primary's position slightly deviates from it. The stars' positions are not in satisfactory agreement with their evolutionary tracks. The reliably determined mass of the primary is $M_1 = 6.3(3)\ M_\odot$, while it lies well below the track for a mass of 5 $M_\odot$. The mass of the secondary is $M_2 = 2.5(1)\ M_\odot$, while it lies above the track for a mass of 3 $M_\odot$. The cause of this discrepancy should be sought in peculiar evolution of the binary star and in chemical anomalies (Vitrichenko and Plachinda 2000).

THE SURROUNDINGS OF BM Ori AND POSSIBLE SOURCES OF THE THIRD LIGHT

Three companions have been found near BM Ori in the last several years.

The first of them was discovered by McCaugrean and Staufer (1994) on the images obtained with the 3.5-m Calar Alto Observatory telescope (Spain) using a CCD array sensitive to the *K* band. Reduction of the observations yielded an angular resolution of $0\farcs35$ and a photometric accuracy in the range $0\fm01$–$0\fm05$. The authors designated this companion as B1. Petr *et al.* (1998) found B1 to be a binary star: another star lies $0\farcs14$ south of the brighter star. It was not named, its position was not given, and its brightness was not measured. For convenience, we retain the designation B1

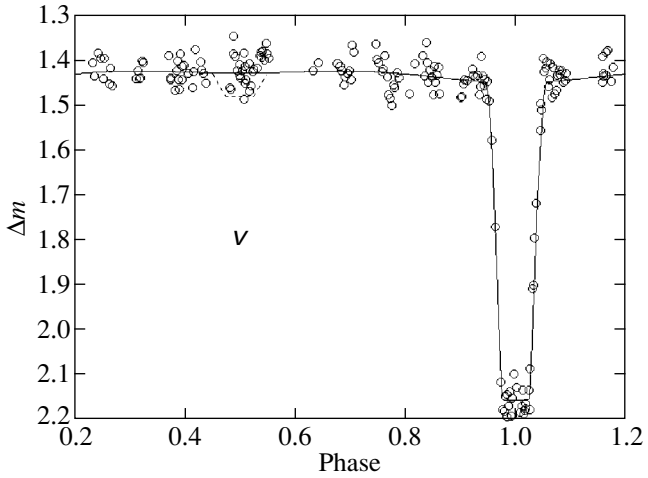

Fig. 3. Same as Fig. 2 for the *v* band.

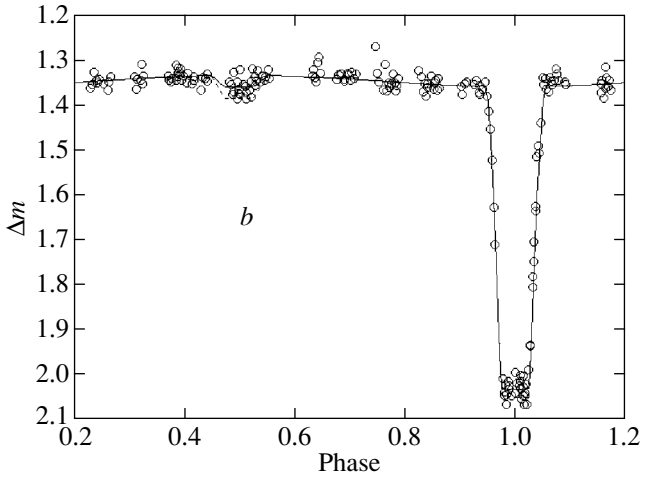

Fig. 4. Same as Fig. 2 for the *b* band.

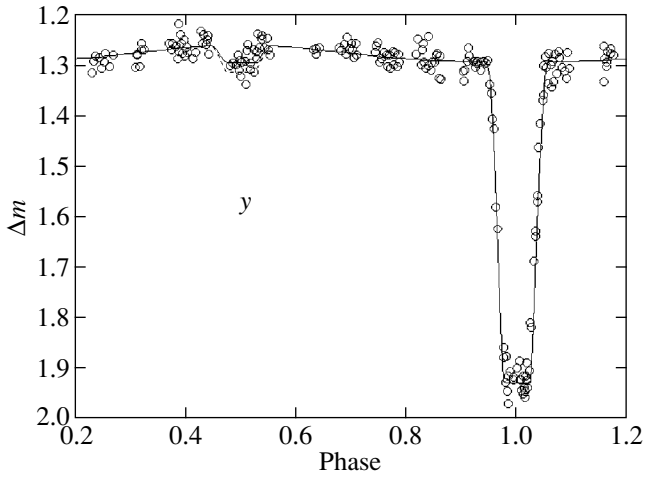

Fig. 5. Same as Fig. 2 for the *y* band.

for the brighter northern component and designate the southern component as B2, by analogy with the brighter star.

Simon *et al.* (1999) confirmed the binary nature of B1; its components were designated as *a* (the brighter northern component) and *b* (the fainter southern component). In our notation, *a* = B1 and *b* = B2. In addition, a third companion was found, which the authors designated as AO 116. By analogy with the first two companions, we designate it as B3. Simon *et al.* (1999) believe the third companion B3 to be seen in Fig. 5 from Petr *et al.* (1998), but the authors failed to notice it and did not include it in the star catalog.

Weigelt *et al.* (1999) resolved the stars B1 and B2 and measured their *HK* brightness relative to the star B. They designated the spectroscopic binary as B_1, B1 as B_2, and B2 as B_3. The star B3 was not detected.

Figure 11 shows the companions' positions relative to the spectroscopic binary. We plotted B1 and B2 and B3 on a map using the data from Weigelt *et al.* (1999) and Simon *et al.* (1999), respectively. The dashed circle in this figure schematically shows the companion B4, which is dealt with below.

Let us consider the possible nature of the third light.

The technique for determining the intensity L_3 of the third light is such [see equations (5)] that this quantity includes the fluxes from all the objects that fall within a photometer resolution element, except the fluxes from the two stars involved in an eclipse.

According to our results, the source of the third light is a B0 subdwarf; in the spectral range under study, this star is comparable in brightness to the stars involved in an eclipse. None of the stars B1, B2, and B3 can be the source of the third light, because they are much fainter than the eclipsing system, and because the *H–K* color for B1 and B2 corresponds either to a cool star or to a highly reddened star. Vitrichenko (1998b) obtained $H–K \approx 0^m.3$ for the binary system, and Weigelt *et al.* (1999) found $H–K \approx 0^m.9$ for B1. Thus, the companion B1 is much redder than the eclipsing system. Since the infrared excess observed in the binary star does not contribute to the spectral range under study (Vitrichenko and Larionov 1996), the cool emission from B1 definitely does not show up in this range; in that case, B1 cannot be the source of the third light.

The *H–K* colors cannot be used to estimate the spectral types of the stars B1 and B2, because the circumstellar extinction A_V for the Orion Trapezium stars ranges from 0^m to 5^m, while the excess in *K* ranges from

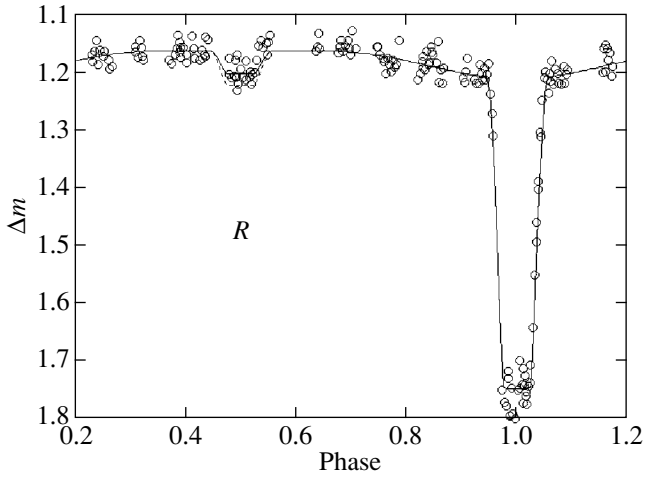

Fig. 6. Same as Fig. 2 for the *R* band in Cousins' photometric system.

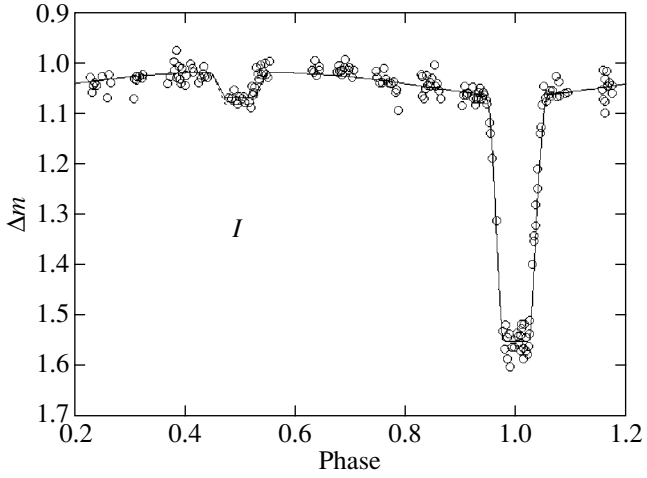

Fig. 7. Same as Fig. 2 for the *I* band in Cousins' photometric system.

0^m to 2^m (Simon *et al.* 1999). To solve the problem requires photometric observations of the companions over a wide spectral range, which are not available so far.

The above-color estimates are quite arbitrary, because none of the authors that observed the companions gave the epochs of their observations. Meanwhile, the probability of falling on the primary or secondary minimum by chance is 30%. Of the two series of observations by McCaugrean and Staufer (1994), one falls within the region of the secondary minimum, while the other falls within the region of the primary minimum (judging by the dates). Weigelt *et al.* (1999) obtained their observations near elongations. Simon *et al.* (1999) gave only the interval of observations, while Petr *et al.* (1998) made no mention of the dates. Meanwhile, the depth of the primary minimum is $0^m.85$ and $0^m.53$ in *H* and *K*, respectively (Vitrichenko 1998b). The depth of the secondary minimum is not known.

A close examination of Fig. 3 from Simon *et al.* (1999) reveals the "trace" of yet another companion. The shape of the star B (it is designated E in this figure) is noticeably elongated in a south-southeasterly direction. This is probably the effect of the presence of yet another companion, which a B0 subdwarf may be. Next, in Fig. 2 from Weigelt *et al.* (1999), a curvature of the primary's isolines is noticeable on the *H*-band map in the same south-southeasterly direction at approximately the same distance from the primary star ($\sim 0''.1$). This curvature can also be interpreted as the effect of yet another star. Thus, the traces of yet another companion are clearly seen in the two studies. In Fig. 11, this companion is designated as B4, and its position is schematically shown by a dashed circle.

McCaugrean and Staufer (1994) gave a list of objects whose positions agree, within the error limits, with the positions of B1.

A cloud of hot ionized gas is observed near the star Θ^1 Ori B1, which shows up in Hα emission (McCulough *et al.* 1995). It may well be that the emission from this gas rather than the B0 star is the third light. This emission cannot be estimated quantitatively, because we only know that it exists.

The position of Θ^1 Ori B1 coincides, within the error limits, with that of the radio source VLA 15 (Felli *et al.* 1993), whose radiation is nonthermal in nature. A total of 49 compact radio sources have been discovered in the Orion Trapezium region, 2/3 of which are variable. The gyrosynchrotron mechanism associated with intense atmospheric flares in young stars (Stein *et al.* 1988) is a possible energy source of the radio sources. Depending on the electron energy and magnetic-field strength, the gyrosynchrotron radiation can be observed in any spectral range, so it can be the source of the third light and can be responsible for stellar flares (Zheleznyakov 1997).

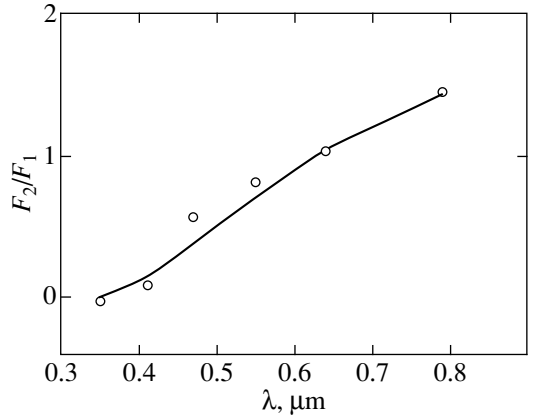

Fig. 8. Ratio of the fluxes from the secondary (F_2) and the primary (F_1) versus wavelength. The circles indicate the observed flux ratio, and the solid line represents a theoretical curve for the case where the secondary and primary stars are of spectral types G0 and B3, respectively. The flux ratio for the *y* band is 0.95.

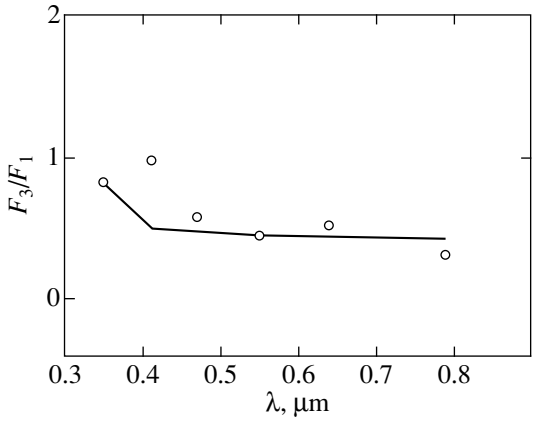

Fig. 9. Same as Fig. 8 for the third and primary stars. The theoretical curve was constructed for the case where the third star is of spectral type B0 and the flux ratio in *y* is 0.46.

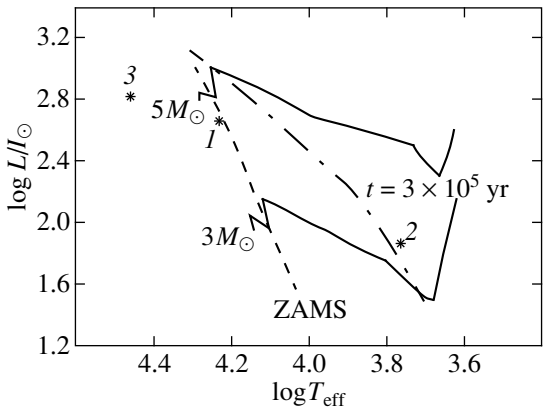

Fig. 10. Hertzsprung–Russell diagram. The asterisks indicate the primary (*1*), the secondary (*2*), and the third star (*3*). The dashed line represents the zero-age main sequence (ZAMS), as constructed by Straizis and Kuriliene (1981). The solid lines are the evolutionary tracks, as constructed by Iben (1965); stellar masses are indicated near the left edges of the tracks. The dashed–dotted line represents the 3×10^5-year isochrone.

Table 2. Characteristics of the components of BM Ori

Quantity	1	2	3
V_0	$8^m.1(1)$	$8^m.3(1)$	$9^m.1(1)$
Sp	B3–B4	G0–G2	B0
$T_{\rm eff}$, K	17000	5700	29000
BC	$-1^m.8$	$0^m.0$	$-3^m.2$
M_V	$-0^m.1$	$+0^m.1$	$+0^m.9$
M_b	$-1^m.9$	$+0^m.1$	$-2^m.3$
$\log L/L_\odot$	2.66	1.86	2.82
$R, R_\odot$	2.50(5)	8.4(2)	1.0

There is intense X-ray radiation in the Orion Trapezium region (Yamauchi *et al.* 1996), which has a fine structure and is variable with time (Gagne *et al.* 1995). The nature of this radiation is unclear, but its long-wavelength "tail" can be the source of the third light.

DISCUSSION

In the Introduction, we described the difficulties involved in obtaining high-quality photoelectric observations for BM Ori. These difficulties did not allow the observers to reliably determine the depth of the secondary minimum. Wolf's observations, which were first performed with a CCD photometer, make it possible to eliminate some of the difficulties and to obtain reliable depths of the secondary minimum in a wide spectral range. This enables us to estimate the secondary's surface brightness for several wavelengths and, hence, its temperature and relative luminosity (brightness). An analysis of these parameters shows that, for the light curve to be explained, we must assume that there is a third star in the system which is not involved in an eclipse, but whose contribution to the system's total light is significant.

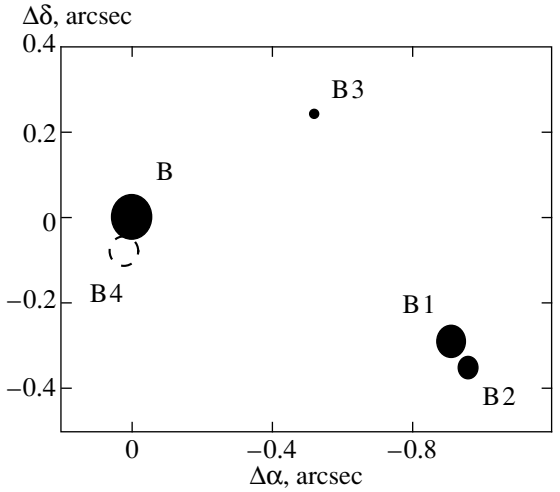

Fig. 11. A finding chart for BM Ori. North is at the top, and east is on the left. B is the spectroscopic binary and eclipsing system Θ^1 Ori B. B1, B2, and B3 are the companions. The dashed circle schematically shows the position of the system's sixth member B4, which is presumably the source of the third light and whose "trace" can be seen in the figures from Simon *et al.* (1999) and Weigelt *et al.* (1999).

We have shown that the eclipse model in which a G secondary obscures a B primary during a total eclipse, with a third B0 star emitting radiation, is in agreement with the observations. This hypothesis is consistent with the fact that, being less massive, the G star has not yet reached the main sequence, and its contraction is not complete; since it is a giant, its radius is considerably larger than that of the primary star.

The contribution of the third star to the system's total light is 20–30% in the photographic and red spectral ranges and reaches 50% in the ultraviolet. If this is the case, then the facts that have previously seemed incomprehensible can be explained. Zakirov and Shevchenko (1982) found the star's spectral type to becomes earlier with decreasing wavelength. In the model we propose, this is because the contribution of the earlier third star to the system's total light increases, while that of the secondary star decreases. There is ample evidence that the spectral type of the primary star is B3, but the hydrogen lines are weak (Vitrichenko and Tsymbal 1996). These authors failed to explain this phenomenon, but now it becomes understandable: the contribution of the B0 and G stars to the total light reduces the hydrogen-line intensity, because the hydrogen lines in these stars are weaker than those in the primary.

The eclipse model considered above is not the only possible one. It is consistent with observations, but previously considered eclipse models can be modified to achieve satisfactory agreement with observations.

The simplest model assumes the involvement of two stars in an eclipse. As was shown above, it is consistent with the light curves, except for the uv bands. In these bands, however, the contribution of flare activity is great, which may result in "flooding" of the secondary minimum. Another difficulty of this model is that the secondary proves to be brighter than the primary, and that primary lines are seen in the spectrum. This difficulty is removed if the secondary's chemical composition is abnormal: the metal abundance is several-fold lower than the solar one. Arguments for this possibility were given by Vitrichenko and Plachinda (2000).

The eclipse model in which a dust envelope around the secondary star is the eclipsing body satisfactorily accounts for the primary minimum. The difficulty of this model is that there must be no secondary minimum, while it is observed in four bands. However, this contradiction can be removed if the model parameters are adjusted in such a way that not only the envelope,

but also the secondary's disk are involved in an eclipse. Numerical simulations have confirmed this possibility.

Invoking a new eclipse model also creates new problems. In the model with a dust envelope around the secondary star, it was clear precisely where the dust producing an infrared excess is localized in the system. This dust surrounds the secondary (Vitrichenko 1996). It now turns out that there is no dust around the secondary, and it becomes necessary to determine its localization region. Vitrichenko and Plachinda (2000) adduce arguments for the fact that half the dust radiation originates near the binary system and the other half originates near Θ^1 Ori B1. It has recently been established that Θ^1 Ori B1 is a binary star (B1 + B2) with yet another companion B3 located at a distance of 260 AU from the binary (Simon *et al.* 1999; Weigelt *et al.* 1999). A chance projection of field stars within 1″ of BM Ori has a probability of less than 1% (Weigelt *et al.* 1999). As a result, BM Ori turns out to be a sextuple system, and to solve the problem of dust localization requires further studies.

The eclipse scheme considered here allows the region of the system's flare activity to be localized. Since flares are also observed near the maximum eclipse phase (Bondar' and Vitrichenko 1995), when the primary star is unobservable, only the secondary component and/or the third star can flare up in this case. However, there is agreement, within the error limits, between the four observations of Θ^1 Ori B1 on different dates. In that case, the secondary flares up. This conclusion is preliminary, because it is based on a small number of observations of Θ^1 Ori B1.

CONCLUSION

We have proposed an eclipse model for BM Ori in which a G0–G2 III secondary component obscures a B3 primary star during totality, but, at the same time, a B0 star, which produces a third light in the system, emits radiation. The model is based on an analysis of Wolf's (1994) observations. Using this model, we have solved the light curves and estimated the luminosities of all three stars, their temperatures, and spectral types.

According to the Hertzsprung–Russell diagram, the primary star lies on the ZAMS, while the secondary star is on the way from the birthline to the main sequence. Both stars are located near the $t = 3 \times 10^5$-year isochrone (Vitrichenko 1996). Their effective temperatures proved to be slightly lower than those in other eclipse models. The third star may be a hot subdwarf, but a nonstellar nature of the third light cannot be ruled out either.

ACKNOWLEDGMENTS

We wish to thank N.I. Bondar' and B.A. Burnasheva for helpful discussions. We are also grateful to the referees, A.A. Tokovinin and V.L. Khokhlova, for constructive remarks, which have improved the article.

REFERENCES

1. C. N. Arnold and D. S. Hall, Acta Astron. **26**, 91 (1976).
2. M. S. Bessel, Publ. Astron. Soc. Pac. **91**, 589 (1979).
3. N. I. Bondar' and É. A. Vitrichenko, Pis'ma Astron. Zh. **21**, 700 (1995) [Astron. Lett. **21**, 627 (1995)].
4. N. I. Bondar' and É. A. Vitrichenko, Pis'ma Astron. Zh. **22**, 257 (1996) [Astron. Lett. **22**, 229 (1996)].
5. N. I. Bondar' and É. A. Vitrichenko, Astron. Zh. **74**, 701 (1997) [Astron. Rep. **41**, 621 (1997)].
6. M. Bossi, A. Gaspani, M. Scardia, and M. Tadini, Astron. Astrophys. **222**, 117 (1989).
7. C. Doremus, Publ. Astron. Soc. Pac. **82**, 745 (1970).
8. M. Felli, G. B. Taylor, M. Catarzi, *et al.*, Astron. Astrophys. **101**, 127 (1993).
9. M. Gagne and L.-P. Cailault, Astrophys. J. **445**, 280 (1995).
10. G. A. Gurzadyan, *Planetary Nebulae. Physics, Dynamics* (Nauka, Moscow, 1993).
11. D. S. Hall, Bamberg Veroff. **9**, 217 (1971).
12. D. S. Hall and L. M. Garrison, Publ. Astron. Soc. Pac. **81**, 771 (1969).
13. M. Humanson and F. Zwicky, Astrophys. J. **105**, 85 (1947).
14. I. Iben, Astrophys. J. **141**, 993 (1965).
15. D. Ya. Martynov, *A Course in Practical Astrophysics* (Nauka, Moscow, 1977).
16. *A Course in Astrophysics and Stellar Astronomy*, Ed. by A. A. Mikhaĭlov (Fizmatgiz, Moscow, 1962), Vol. 2.
17. M. J. McCaugrean and J. R. Staufer, Astron. J. **108**, 1382 (1994).
18. P. R. McCulough, R. Q. Fugate, J. C. Christou, *et al.*, Astrophys. J. **438**, 394 (1994).
19. P. P. Parenago, Perem. Zvezdy **6**, 217 (1947).
20. M. G. Petr, S. V. W. Beckwith, A. Richichi, and M. G. McCaughrean, Astrophys. J. **500**, 825 (1998).
21. D. M. Popper and M. Plavec, Astrophys. J. **205**, 462 (1976).
22. M. Simon, L. M. Close, and T. L. Beck, Astron. J. **117**, 1375 (1999).
23. P. C. Stein, E. D. Feigelson, P. Andre, and T. Montmerl, Astron. J. **96**, 1394 (1988).
24. V. Straĭzhis, in *Multicolor Stellar Photometry* (Mokslas, Vilnius, 1977).
25. V. Straizis and G. Kuriliene, Astrophys. Space Sci. **80**, 353 (1981).
26. W. F. van Altena, J. T. Lee, J.-F. Lee, *et al.*, Astron. J. **95**, 1744 (1988).
27. É. A. Vitrichenko, Pis'ma Astron. Zh. **21**, 518 (1995) [Astron. Lett. **21**, 460 (1995)].
28. É. A. Vitrichenko, Pis'ma Astron. Zh. **22**, 587 (1996) [Astron. Lett. **22**, 523 (1996)].
29. É. A. Vitrichenko, Pis'ma Astron. Zh. **24**, 708 (1998) [Astron. Lett. **24**, 611 (1998)].
30. É. A. Vitrichenko, Preprint No. 1991, IKI RAN (Institute for Space Research, Russian Academy of Sciences, 1998b).
31. É. A. Vitrichenko and V. G. Klochkova, Pis'ma Astron. Zh. **26**, 133 (2000) [Astron. Lett. **26**, 104 (2000)].

32. É. A. Vitrichenko and V. M. Larionov, Pis'ma Astron. Zh. **22**, 178 (1996).
33. É. A. Vitrichenko and S. I. Plachinda, Pis'ma Astron. Zh. (2000) (in press) [Astron. Lett. (2000) (in press)].
34. É. A. Vitrichenko and V. V. Tsymbal, Pis'ma Astron. Zh. **22**, 132 (1996) [Astron. Lett. **22**, 116 (1996)].
35. É. A. Vitrichenko, V. S. Shevchenko, and V. A. Shcherbakov, Pis'ma Astron. Zh. **22**, 185 (1996) [Astron. Lett. **22**, 163 (1996)].
36. G. Weigelt, Y. Balega, T. Preibisch, *et al.*, Preprint No. 799, Max Plank Inst. (1999).
37. G. W. Wolf, Exp. Astron. **5**, 61 (1994).
38. S. Yamauchi, K. Koyama, M. Sakano, and K. Okada, Publ. Astron. Soc. Jpn. **48**, 719 (1996).
39. M. M. Zakirov and V. S. Shevchenko, Peremen. Zvezdy **21**, 629 (1982).
40. V. V. Zheleznyakov, *Radiation in Astrophysical Plasmas* (Yanus-K, Moscow, 1997).

Translated by V. Astakhov

Astronomy Letters, Vol. 26, No. 8, 2000, pp. 539–543. Translated from Pis'ma v Astronomicheskiĭ Zhurnal, Vol. 26, No. 8, 2000, pp. 624–629.

Penetration of Coronal Magnetic Fields into Solar-Wind Streams

N. A. Lotova[1]*, V. N. Obridko[1], K. V. Vladimirskiĭ[2], and V. Rušin[3]

[1] *Institute of Terrestrial Magnetism, Ionosphere, and Radiowave Propagation, Russian Academy of Sciences, Troitsk, Moscow oblast, 142092 Russia*

[2] *Lebedev Physical Institute, Russian Academy of Sciences, Leninskiĭ pr. 53, Moscow, 117924 Russia*

[3] *Astronomical Institute, Slovak Academy of Sciences, SK 059 60, Tatranska Lomnica, Slovakia*

Received February 17, 1999; in final form, February 23, 2000

Abstract—The formation of solar-wind stream structure is investigated. Characteristic features of the solar and coronal magnetic-field structure, morphological features of the white-light corona, and radio maps of the solar-wind transition (transonic) region are compared. The solar-wind stream structure is detected and studied by using radio maps of the transition region, the raggedness of its boundaries, and their deviation from spherical symmetry. The radio maps have been constructed from radioastronomical observations in 1995–1997. It is shown that the structural changes in the transition region largely follow the changes occurring in regions closer to the Sun, in the circumsolar magnetic-field structure, and in the solar-corona structure. The correlations between the magnetic-field strength in the solar corona and the location of the inner (nearest the Sun) boundary of the transition region are analyzed. The distinct anticorrelation between the coronal magnetic-field strength and the distance of the transition region from the Sun is a crucial argument for the penetration of solar magnetic fields into plasma streams far from the Sun. © *2000 MAIK "Nauka/Interperiodica"*.

Key words: *Sun, corona, magnetic fields, solar wind, transition region*

INTRODUCTION

In this paper, we make a comprehensive comparison of experimental data on the large-scale structure of circumsolar plasma and solar-wind streams. Considerable progress has been made previously in investigating the mechanisms that determine significant deviations from the previously used spherically symmetric model. It has been established that the passage from a subsonic flow in the immediate vicinity of the solar surface to a supersonic one at large distances occurs in an extended region. The accompanying changes in the flow mode largely determine the stream turbulence and the acceleration energetics (Lotova *et al.* 1985, 1995; Wang *et al.* 1990; Efimov *et al.* 1990; Schwenn and Marsch 1995; Kojima and Kakinuma 1990; Rickett and Coles 1991; Bird 1991; Efimov 1994; Rao *et al.* 1995; Tokumaru *et al.* 1995; Bird and Pätzold 1995; Woo 1996; Lotova and Vladimirskiĭ 1997). However, the basic problems of solar-wind physics, its sources and acceleration mechanisms have not been studied adequately. The irregular structure of circumsolar plasma streams is a major factor in the formation of a supersonic solar wind (Malara *et al.* 1992; Vladimirskiĭ *et al.* 1996), but the specific mechanisms of the phenomena in this region are virtually unstudied. The role of magnetic fields in the circumsolar plasma acceleration is also poorly understood. The problem as a whole is far more complex than any studies of laboratory-scale processes. The solar wind begins as a slow expansion of very dense plasma in a strong gravitational field; a stream of tenuous plasma moving radially at supersonic velocities arises far from the Sun. We therefore analyze here the correlations between circumsolar plasma stream parameters during the formation of a supersonic solar wind by using the specific experimental studies carried out in 1995–1997 at the epoch of solar minimum, which completes solar cycle 22. We use radioastronomical data on the scattering of radio emission from compact natural sources by circumsolar plasma, optical observations of the white-light solar corona, and data on the magnetic-field strength and structure at small distances from the solar surface. The distance from the Sun at which the passage to a supersonic flow occurs is used to estimate the acceleration rate. It is important that we also compare the morphological features of the solar corona with the solar-wind flow structure at large distances.

SOLAR MAGNETIC FIELDS

To ascertain the specific mechanisms governing the solar-wind flow, we studied the large-scale flow struc-

* E-mail address for contacts: nlotova@izmiran.troitsk.ru

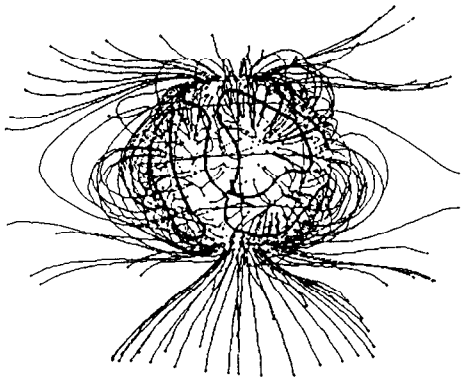

Fig. 1. Large-scale structure of the magnetic field on the solar surface on March 9, 1997.

tures in comparison with the magnetic fields at small distances from the Sun. We used the data on photospheric magnetic fields obtained at J. Willcox Observatory (Stanford, California, USA) and retrieved via Internet. Based on these data, we calculated the field strength in the region between the solar surface and a sphere of radius $R = 2.5R_s$ (Obridko *et al.* 1994; Kharshiladze and Ivanov 1994). The $R = 2.5R_s$ sphere was arbitrarily taken as the "source surface," above which the subsonic solar wind region extends. We performed our calculations in the potential approximation and disregarded the possible effects of the circumsolar medium inside the above region.

We calculated the magnetic fields for 1995–1997, which allowed us to establish the general features of the field structure for the epoch of solar minimum and to compare these structures with the solar-wind stream structure far from the Sun. The results of our calculations were obtained in two forms: we determined the structure of magnetic field lines in a spherical layer $R_s \le R \le 2.5R_s$; the magnitudes of radial magnetic-field component $|B_R|$ calculated for a radial distance of $2.5R_s$ were used to analyze the correlations.

The field-line structures were constructed by using initial conditions in the form of a uniform grid of points on the $R = R_s$ sphere (on the solar surface). On the source surface ($R = 2.5R_s$), structures with angular scale sizes from 3 to 10 arcmin emerge. The "traces" of these structures are transferred by the solar wind and can be diagnosed by the sounding method far from the Sun, $R \ge 40R_s$. Figure 1 shows the field-line structure calculated for the epoch of observation of the total solar eclipse on March 9, 1997. In the figure, we see a field pattern in the polar regions similar to a dipole field with an open structure of field lines, which is typical of the epoch of solar minimum. An appreciable N–S asymmetry is noticeable, with a stronger magnetic field in the southern polar region. On the solar surface ($R = R_s$), we plotted the neutral line of the magnetic field.

STRUCTURAL FEATURES OF THE WHITE-LIGHT CORONA

A comparison of the shape of the white-light corona with the above data on the structure of circumsolar magnetic fields is of great interest in studying the formation mechanism of the solar-wind stream structure. Individual features in the coronal structure extend to distances of up to several solar radii from the solar surface and allow a direct comparison with magnetic data (Rušin *et al.* 1992; Koutchmy and Livshits 1992).

Figure 2 shows the structure of the white-light corona reconstructed from the observations of the solar eclipse on March 9, 1997. We see helmet streamers extending to $5–6R_s$, considerable flattening at the poles, and polar coronal holes. We also used similar observations of the October 24, 1995 eclipse (Rušin *et al.* 1996; Pinter *et al.* 1997; Gulyaev 1998). Apart from the observations of total solar eclipses, we used SOHO photographs of the white-light corona retrieved via Internet. The dates were chosen in accordance with the time of our radioastronomical observations.

The shape and sizes of the corona (see Fig. 2) are typical of the epoch of solar minimum. The corona is modest in size; it is highly flattened at the poles. A persistent N–S asymmetry, the invariably larger flattening of the corona in the southern polar region, is also typical of the epoch of minimum of solar cycle 22. The latter circumstance is directly compared with the magnetic data: on the same days, enhanced magnetic-field strengths were obtained for the southern polar region. The same direct comparison can also be made for finer structural features.

RADIO-WAVE SCATTERING EXPERIMENTS

Regular experiments on the sounding of circumsolar plasma by radio emission from compact natural sources, quasars, and water-vapor maser sources have been carried out with large radio telescopes in Pushchino (Russian Academy of Sciences) since 1987. The cross-shaped DKR-1000 radio telescope, which operates at meter wavelengths, is used in interferometer mode to measure the apparent angular sizes of sources and the radio-wave scattering angle 2Θ. The RT-22 radio telescope is used for observing scintillations of maser sources at 1.35 cm. In both cases, long (of the order of a month) series of observations are carried out, allowing the radial dependence of the scattering of radio emission from sources passing near the Sun to be studied. The main result of these observations is the radial dependence of the radio-wave scattering, from which the locations of the inner (R_{in}) and outer (R_{out}) boundaries of the solar-wind transition region can be determined. Against the background of a general falloff of the scattering with increasing radial distance, the transition region shows up as a region of enhanced scattering. A study of the nature of this phenomenon shows that the change in scattering results from a change in

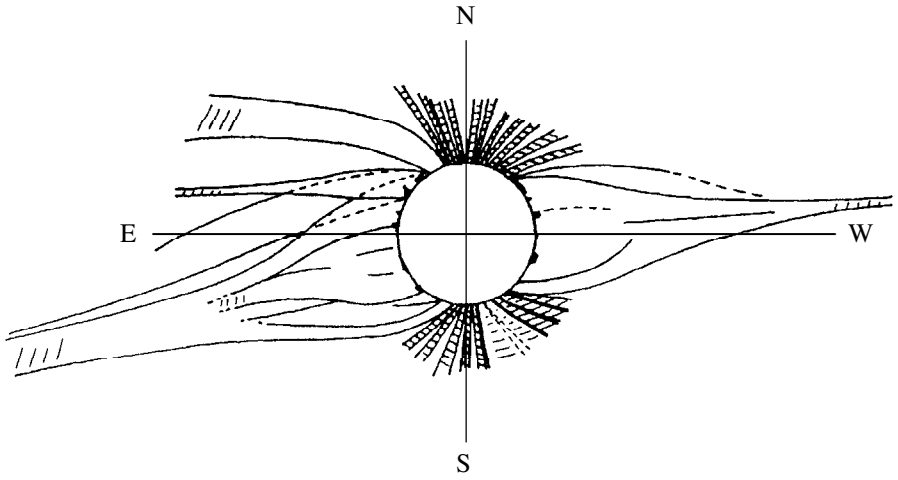

Fig. 2. Structure of the white-light corona reconstructed from photographs of the solar eclipse on March 9, 1997.

the flow mode (Lotova *et al.* 1985; Lotova 1992). In the transition region, the mixed flow mode is realized, where both subsonic and supersonic plasma streams coexist and interact. The enhanced scattering, the enhanced flow turbulence, is associated with the instability of discontinuities in such flows (Syrovatskiĭ 1954). It is important that the transition region is a region in which the main acceleration of solar-wind streams takes place. At $R > R_{out}$, the solar-wind stream structure is retained. Revealing the key parameters that can determine the retention of a considerable solar-wind flow irregularity is a research problem of great importance. In particular, as the data presented here indicate, the strength of the magnetic field frozen in solar-wind streams is such a parameter.

The techniques for scattering observations and for experimental data reduction, which allow the transition-region parameters to be studied, were described by Lotova *et al.* (1985) and Lotova and Nagelys (1988). Determination of the location of the transition-region inner boundary is considerably facilitated by using a characteristic feature of the flow in the subsonic region (Lotova and Vladimirskiĭ 1997). A "precursor" of the transition region, a narrow region of sharply reduced scattering whose distance from the transition region is small and is not subject to significant variations, is observed near the transition-region inner boundary.

In connection with the study of the formation of solar-wind stream structure, we compare here the heliolatitude dependences of the location of the transition-region inner boundary (R_{in}) and the coronal magnetic-field strength at a radial distance of $2.5R_s$ ($|B_R|$). In this study, as previously, the angular coordinates were reconciled with the times of observations. As the argument, we use the position angle φ ($0° \le \varphi \le 360°$), which is measured counterclockwise from the northward direction. The 1997 results are presented in Fig. 3. The 1995–1996 observations were used in a similar way. To improve the statistics in the dependence of $|B_R|$ on position angle, apart from the values calculated for the times of R_{in} determination (denoted in Fig. 3 by triangles), we used the values corresponding to the times of R_{out} determination (denoted by circles).

A clear anticorrelation between the magnetic-field strength and the radial distance of the transition region from the Sun is directly seen from Fig. 3: a location of the transition region closer to the Sun corresponds to large field strengths (~7 μT). Since such a location of the transition region suggests intense acceleration processes and the probable emergence of high-speed solar-wind streams (Lotova *et al.* 1995), Fig. 3 can be considered as direct evidence for a major role of solar magnetic fields in the circumsolar plasma acceleration mechanism. The structural features of the magnetic fields and plasma flows emerging at small distances from the Sun are retained during the subsequent acceleration at radial distances of $(10–40)R_s$; hence the retention of a considerable irregularity of the flow, the stream structure, in the supersonic region far from the Sun.

RADIO MAPS OF THE SOLAR-WIND TRANSITION REGION

To obtain maximum information about the state of the circumsolar medium, the largest possible number of sources is used in sounding experiments. Observations of sources passing near the Sun at various heliolatitudes are of greatest value. Using such sources allowed us to present the results of the observations in the form of radio maps, two-dimensional images of the solar-wind transition region on which the contours of the inner and outer boundaries of the transition region are plotted (Lotova and Korelov 1992; Lotova and Vladimirskiĭ 1997). The number of sources accessible in sensitivity that pass simultaneously or at close times is not enough to obtain images which can be directly compared with

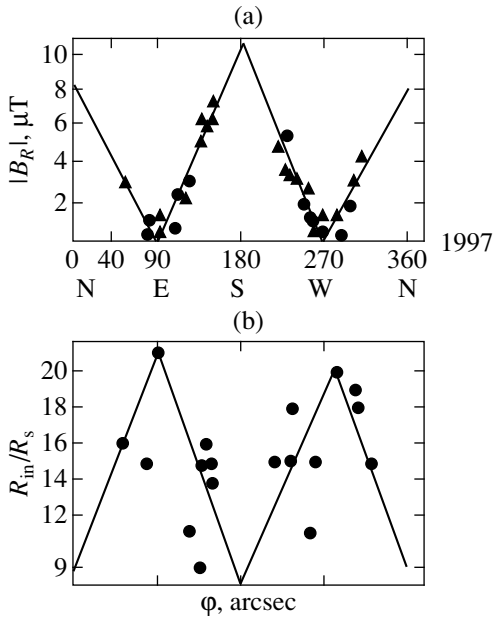

Fig. 3. Coronal magnetic-field strength $|B_R|$ at $R = 2.5R_s$ (a) and location of the transition-region inner boundary R_{in} (b) *versus* position angle φ.

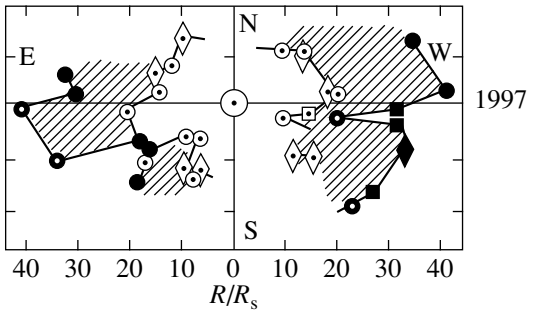

Fig. 4. Radio map of the solar-wind transition region as constructed from the 1997 observations. See the text for an explanation of the notation.

concurrent observations of the solar magnetic fields or the white-light solar corona. Nevertheless, accumulating information over a year, we can obtain radio maps that reflect the most important characteristic features of the processes taking place in the circumsolar medium. Such parameters of the transition region as the flattening in the polar regions and the overall asymmetry vary slowly; radio maps reproduce them quite reliably. The finer features, the raggedness of the transition-region boundaries, are directly comparable with the structural features of the white-light corona only if observations of sources passing at close times are used. However, even in those cases where this condition is not satisfied, the boundaries' raggedness suggests the presence of solar-wind stream structure and considerable deviations from a spherically symmetric flow.

Figure 4 shows the radio map constructed the 1997 observations. The open and filled symbols correspond to the locations of the transition-region inner and outer boundaries, respectively. We used several series of observations. The triangles represent the observations of the quasars 3C2 and 3C5 approaching the Sun in March, and the circles represent the observations of the compact source 3C144 in the Crab Nebula and the quasars 3C133, 3C152, 3C154, 3C162, 3C166, 3C172, 3C192, 3C208, 3C212, 3C215, 3C225, and 3C228 (June and August). The quasars 3C273, 3C275, and 3C279 pass in October and are denoted in the figure by squares. The maser sources GGD4, S252, U Ori passing in June, and IRC-20431, W31(2) passing in December are marked with diamonds.

The results presented in Fig. 4 and similar observations in 1995 and 1996 include the year of solar minimum (1996). The evolution of the transition region in previous years was studied by Lotova and Vladimirskiĭ (1997). Basically, this is an increasingly closer approach of the transition region to the Sun as the solar minimum is approached. The 1995–1997 results show that the transition region was closest to the Sun in 1995 rather than in 1996, the year of solar minimum. The years 1995–1997 are characterized by a flattening of the transition region at the poles and by its considerable asymmetry. As in the above results referring to small distances from the Sun, to the coronal region, a considerable N–S asymmetry is retained during all three years 1995–1997. The transition-region structure in 1995 inclined to the helioequator plane engages our attention. The region shape and the inclination closely match the results of solar-corona observations in the eclipse of October 24, 1995. The inclination of the transition region to the helioequator is unnoticeable in 1996 and small in 1997. A comparison of Fig. 4 with Fig. 2 shows that the transition-region shape also largely follows the corona shape here. In general, the study of the large-scale structure of the solar-wind transition region using radio maps suggests that the flow structural features emerging under the effect of coronal magnetic fields near the solar surface are retained during the solar-wind acceleration at distances of $(10–40)R_s$.

CONCLUSION

We have compared the parameters describing the state of circumsolar plasma and solar-wind streams at the end of solar cycle 22, at the epoch of solar minimum. We used data on the magnetic-field strength and structure, observations of the white-light solar corona, and radioastronomical observations of radio-wave scattering by circumsolar plasma. The magnetic-field structure at small distances from the Sun, in the coronal region, is shown to completely determine the plasma flow pattern near the Sun. The salient features of this pattern are retained during the subsequent solar-wind acceleration at radial distances of $(10–40)R_s$ from the Sun. The course of the acceleration itself is largely

determined by the magnetic-field strength at the base of the solar-wind streamlines, in the coronal region. A location of the inner boundary of the solar-wind transition region closer to the Sun, a low flow turbulence level, intense acceleration processes, and high supersonic-flow velocities far from the Sun correspond to enhanced magnetic-field strengths. The available experimental data indicate that the solar magnetic fields and their penetration into solar-wind streams determine the large-scale solar-wind structure and are a major factor in the solar-wind acceleration mechanism.

ACKNOWLEDGMENTS

The radioastronomical data were obtained with two radio telescopes: RT-22 (registration number 01-10) and DKR-1000 (registration number 01-09). We are grateful to the staff of the J. Willcox Observatory for the solar magnetic field data retrieved via Internet and to the SOHO staff for the image of the white-light corona also retrieved via Internet. The work of the Russian authors was supported by the Sate Science and Technology Program "Astronomy" (project no. 4-151), the Russian Foundation for Basic Research (project no. 97-02-16233), and RFBR-NNIO (project no. 96-01-00040G).

REFERENCES

1. M. K. Bird, J. Geomag. Geoelectr. Suppl. **43**, 71 (1991).
2. M. K. Bird and M. Pätzold, Geophys. Res. Lett. **22**, 329 (1995).
3. A. I. Efimov, Space Sci. Rev. **70**, 397 (1994).
4. A. I. Efimov, I. V. Chasheĭ, V. I. Shishov, and O. I. Yakovlev, Kosm. Issled. **28**, 581 (1990).
5. R. A. Gulyaev, in *Proceedings of the Guadeloupe Meeting ESA, 1998*, SP-421.
6. A. F. Kharshiladze and K. G. Ivanov, Geomagn. Aéron. **34**, 22 (1994).
7. Kojima and T. Kakinuma, Space Sci. Rev. **53**, 173 (1990).
8. S. Koutchmy and M. Livshits, Space Sci. Rev. **61**, 393 (1992).
9. N. A. Lotova, in *Proceedings of the Solar Wind Seven*, Ed. by E. Marsch and R. Schwenn (Pergamon, New York, 1992), p. 217.
10. N. A. Lotova, D. F. Blums, and K. V. Vladimirskiĭ, Astron. Astrophys. **150**, 266 (1985).
11. N. A. Lotova and O. A. Korelov, in *Proceedings of the Solar Wind Seven*, Ed. by E. Marsch and R. Schwenn (Pergamon, New York, 1992), p. 221.
12. N. A. Lotova and Ya. V. Nagelys, Solar Phys. **117**, 407 (1988).
13. N. A. Lotova and K. V. Vladimirskiĭ, Solar Phys. **172**, 225 (1977).
14. N. A. Lotova, K. V. Vladimirskiĭ, I. Yu. Yurovskaya, and O. A. Korelov, Astron. Zh. **72**, 757 (1995) [Astron. Rep. **39**, 675 (1995)].
15. F. Malara, P. Veltri, C. Chuderi, and G. Enaudi, Astrophys. J. **396**, 297 (1992).
16. V. N. Obridko, A. F. Kharshiladze, and B. D. Shelting, in *Solar Magnetic Fields and Helioseismology* (Bull. Phys. Tech. Inst., St. Petersburg, 1994), p. 71.
17. T. Pinter, M. Lorence, B. Lukac, *et al.*, Contrib. Astron. Obs. Skalnate Pleso **27**, 115 (1997).
18. A. P. Rao, S. Ananthakrishnan, V. Balasubramanian, and W. A. Coles, Am. Inst. Phys., 117 (1995).
19. B. J. Rickett and W. A. Coles, J. Geophys. Res. **96**, 1717 (1991).
20. V. Rušin, L. Klocok, M. Minarovjech, and M. Rybansky, Contrib. Astron. Obs. Skalnate Pleso **26**, 37 (1996).
21. V. Rušin, L. Klocok, P. Zimmermann, *et al.*, Contrib. Astron. Obs. Skalnate Pleso **22**, 117 (1992).
22. R. Schwenn and E. Marsch, in *Physics of the Inner Heliosphere* (Springer-Verlag, Berlin, 1990).
23. S. I. Syrovatskiĭ, Zh. Éksp. Teor. Fiz. **27**, 121 (1954).
24. M. Tokumaru, H. Mori, T. Tanako, and T. Kondo, J. Geomagn. Geoelectr. **47**, 1113 (1955).
25. K. V. Vladimirskiĭ, N. A. Lotova, and O. A. Korelov, Kr. Soobshch. Fiz. FIAN, Nos. 1–2, 12 (1996).
26. Y.-M. Wang, N. R. Sheely, and A. G. Nosh, Nature **347**, 439 (1990).
27. R. Woo, Astrophys. J. Lett. **464**, L95 (1996).

Translated by G. Rudnitskiĭ

Astronomy Letters, Vol. 26, No. 8, 2000, pp. 544–552. Translated from Pis'ma v Astronomicheskiĭ Zhurnal, Vol. 26, No. 8, 2000, pp. 630–640.

Quasi-Harmonic Faraday-Rotation Fluctuations of Radio Waves When Sounding the Outer Solar Corona

A. I. Efimov[1], L. N. Samoznaev[1], V. E. Andreev[1], I. V. Chasheĭ[2], and M. K. Bird[3]

[1] *Institute of Radio Engineering and Electronics, Russian Academy of Sciences, Mokhovaya ul. 18, Moscow, 103907 Russia*
[2] *Lebedev Physical Institute, Russian Academy of Sciences, Leninskiĭ pr. 53, Moscow, 117924 Russia*
[3] *Radio Astronomy Institute, Bonn University, Bonn, Germany*

Received September 10, 1999; in final form, January 15, 2000

Abstract—A statistical analysis of the Faraday-rotation fluctuations (FRFs) of linearly polarized radio signals from the Helios 1 and Helios 2 spacecraft shows that the FRF time power spectra can be of three types. Spectra of the first type are well fitted by a single power law in the range of fluctuation frequencies 1–10 mHz. Spectra of the second type are a superposition of a power law and two quasi-harmonic components with fluctuation frequencies of about $\nu_1 = 4$ mHz (fundamental frequency) and $\nu_2 = 8$ mHz (second harmonic). Spectra of the third type exhibit only one of the two quasi-harmonic components against the background of a power law. The spectral density of the quasi-harmonic components can be represented by a resonance curve with a fairly broad $[\Delta\nu \approx (0.5–1.3)\nu_{1,2}]$ distribution relative to the $\nu = \nu_{1,2}$ peak. The intensity of the quasi-harmonic FRF has a radial dependence that roughly matches the radial dependence for the background FRF, while their period at the fundamental frequency is approximately equal to the period of the well-known 5-min oscillations observed in the lower solar atmosphere. The fluctuations with 5-min periods in FRF records can be explained by the presence in the outer corona of isolated trains of Alfvén waves generated at the base of the chromosphere–corona transition layer and by acoustic waves coming from deeper layers. © *2000 MAIK "Nauka/Interperiodica"*.

Key words: *Sun, fluctuations, radio waves, spectra, magnetic fields, Alfvén waves*

INTRODUCTION

Faraday-rotation-fluctuation (FRF) measurements of the polarization plane of coherent radio signals from spacecraft can provide valuable information about magnetic-field irregularities in the outer solar corona. The FRFs were shown (Hollweg *et al.* 1982; Andreev *et al.* 1997a, 1997b) to be produced by Alfvén waves propagating away from the Sun. According to the estimates by Andreev *et al.* (1997a), Alfvén waves in the solar-wind acceleration region transfer outward an energy flux that considerably exceeds the flux of plasma kinetic energy and, hence, play a significant role in the solar-wind energetics. Observations show (Efimov *et al.* 1993; Andreev *et al.* 1996) that the FRFs have a broad time power spectrum. Of crucial importance in establishing the Alfvén-wave generation source and in diagnosing the outer corona by remote sounding methods is the search for possible quasi-monochromatic features in the FRF power spectra, which would be attributable to the presence of distinct periods in Alfvén waves propagating through the outer corona.

One of the authors (M.K. Bird) took part in the search for quasi-periodicities when the very first Helios FRF records were processed. Using the maximum-entropy method, Edenhofer *et al.* (1980) concluded that quasi-periodic variations with characteristic periods from 10 to 80 min are commonly found in FRF records. In order to detect large long-period variations, they averaged FRF records in a relatively long time interval of 3 or 4 h. In this approach, however, quasi-periodic features in the FRF power spectra can be dramatically smoothed out for a number of reasons, for example, because of the change in the distance between the Sun and the line of sight during a session, because of the changes in the direction of the regular magnetic field and the irregularity intensity. Besides, the sampling rate during the first FRF measurements was not high enough (approximately once in 20 s), which inevitably resulted in the loss of the spectral features associated with rapid processes. The first studies of the FRF spectra calculated from relatively short portions of records (1024–2048 s) at a high sampling rate (approximately once in a second) revealed quasi-periodic fluctuations with a characteristic frequency $\nu \approx 4$ mHz (Andreev *et al.* 1996).

Here, we present the results of a statistical analysis of the quasi-periodic components in FRF records obtained when analyzing a large number of FRF power spectra measured in 1983 in a series of experiments on sounding the outer solar corona by linearly polarized radio signals from the Helios 1 spacecraft. We provide

* E-mail address for contacts: aie114@ire216.msk.su

data on the frequency of occurrence, temporal evolution, and power characteristics of quasi-periodic fluctuations, as well as discuss a possible source of their generation and their correlation with the fluctuations described by a background spectrum.

EXPERIMENTAL DATA REDUCTION

The polarization-plane rotation angles for linearly polarized Helios signals in the *S* band (wavelength λ = 13 cm, frequency f = 2295 MHz) were measured every second at three large ground-based stations of the Deep Space Communications Network (Canberra, Madrid, and Goldstone). The measurements used here were carried out in 1983 when the spacecraft went behind the solar corona at heliocentric distances R (the distance from the impact point of the line of sight to the solar center) in the range 2.8 to $16R_\odot$ ($R_\odot$ is the solar radius). The Faraday-rotation angle ψ of a linearly polarized radio signal (in degrees) is given by

$$\psi = A_0 \int_s N(\mathbf{s}) \cdot \mathbf{B}(\mathbf{s}) d\mathbf{s}, \quad (1)$$

where $A_0 = 1.35 \times 10^{-6}/f^2$, f is the radio-wave frequency in MHz; $N(\mathbf{s})$ is the electron number density in cm^{-3}; and $\mathbf{B}(\mathbf{s})$ is the magnetic-field strength in G. The integration in (1) is performed along the line of sight s from the spacecraft to the observer; the Faraday rotation is associated only with the line-of-sight component of vector $\mathbf{B}(\mathbf{s})$. Since the global solar magnetic field is spherically symmetric, the line-of-sight components B_s for two neighboring segments of the propagation path adjacent to the impact point are approximately equal in magnitude and opposite in sign, so the resulting magnitude of $\mathbf{B}(\mathbf{s})$ is nearly zero. Studying the Faraday rotation of the polarization plane can therefore give information mainly about magnetic-field variations.

Strictly speaking, ψ represents the integrated effect along the propagation path of radio waves from a spacecraft to a ground-based station. However, since both quantities in the integrand abruptly decrease as one recedes from the Sun (the electron density decreases faster than the distance squared, while the decrease in magnetic field is proportional to the distance), the segment of the path adjacent to the impact point whose extent is $\Delta s \approx (0.5–0.7)R$ makes the largest contribution to the integral (1). Thus, the experiments analyzed here deal with values of Δs comparable to the solar radius $R_\odot$.

The Faraday-rotation angle ψ is calculated as the angle between the change in the location of the polarization plane of the received signal at a ground-based station and the known location of the polarization plane of radio waves on spacecraft. Since the spacecraft orientation relative to the Sun and the ground-based station was maintained with a high accuracy during the entire period of active operation, the instrumental polarization-plane rotation was negligible.

The technique for measuring ψ was described in detail by Volland *et al.* (1977). The duration of a single observing session at one ground-based station was several hours, and the sampling rate was 1 Hz.

We broke up the entire $\psi(t)$ record into 2048-s-long intervals and then removed the slowly varying component $\psi_0(t)$, which may be associated with large-scale electron-density and magnetic-field variations, in a given interval. The trend $\psi_0(t)$ was fitted by a third-degree polynomial. For the residuals $\delta\psi(t) = \psi(t) - \psi_0(t)$, we calculated the time power Fourier spectrum $G(\nu)$ in each interval. The time spectra $G(\nu)$ were calculated for successive intervals T_i containing 2048 discrete points. The beginning of each interval was shifted by 512 or 257 discrete points from the beginning of the preceding interval. This technique allows the temporal evolution of FRF statistical parameters to be traced closely. The duration of the intervals, each with 2048 discrete points, was chosen as an optimum one in the search for nonstationary quasi-periodic components. In our calculations of the time power spectra $G(\nu)$, the frequency smoothing was impossible because of the peculiar use of the data: such a smoothing during the entire session would inevitably suppress the possible contribution of nonstationary quasi-periodic fluctuations, while the smoothing within an individual interval would result in the loss of information about fluctuations with expected frequencies of the order of several millihertz. Since the statistical errors for calculations of the spectra $G(\nu)$ prove to be fairly large, the significance of possible spectral features can be confirmed only by their recurrence in various observing sessions. An analysis of the radial dependence of FRF time spectra shows that the fluctuation level decreases as one recedes from the Sun, but the main characteristic spectral features are retained up to heliocentric distances of $\sim 15R_\odot$; starting from these distances, the fluctuation level ceases to depend on distance from the Sun, while the spectra become flat, i.e., purely noise ones. This circumstance strongly suggests a circumsolar origin for the FRFs and a marginal contribution of the Earth's ionosphere.

From all the computed FRF time spectra, for our analysis we chose spectra with features in the form of "spectral lines" against the background of a power law. The number of spectra chosen in this way was ~25% of their total number, while most of the spectra are well fitted by power laws within the range of fluctuation frequencies under study. In order to trace the appearance and disappearance of spectral features, apart from spectra with quasi-harmonic components, we analyzed spectra measured on adjacent time intervals. We calculated the following statistical parameters for the measured FRF time power spectra:

(a) the FRF variance

$$\sigma_\psi^2 = \int_{\nu_{min}}^{\nu_{max}} G(\nu) d\nu, \quad (2)$$

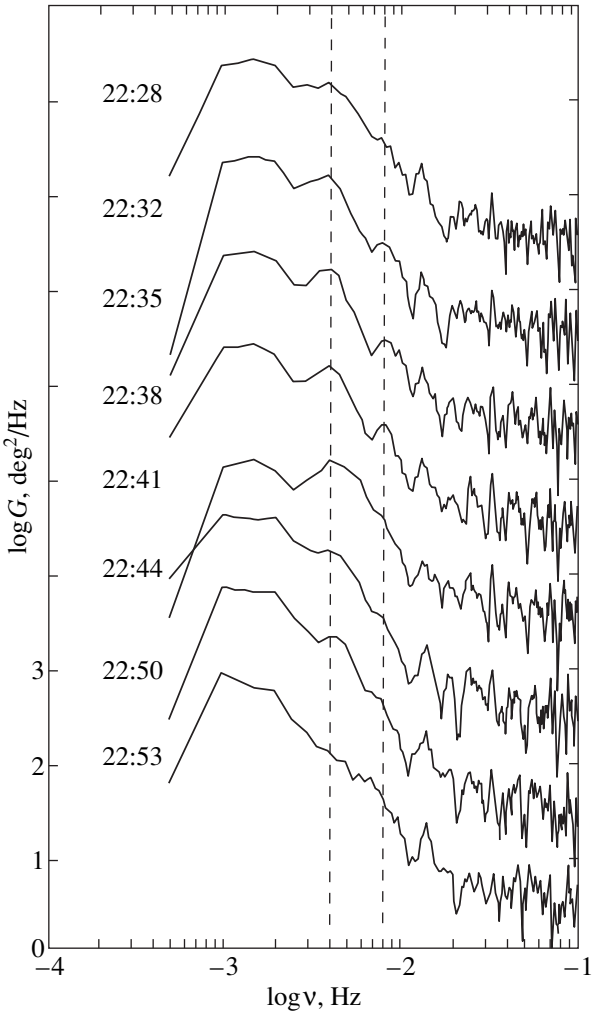

Fig. 1. Temporal evolution of the FRF spectra. The initial time of the measurement interval on which the spectrum was determined is indicated on the left.

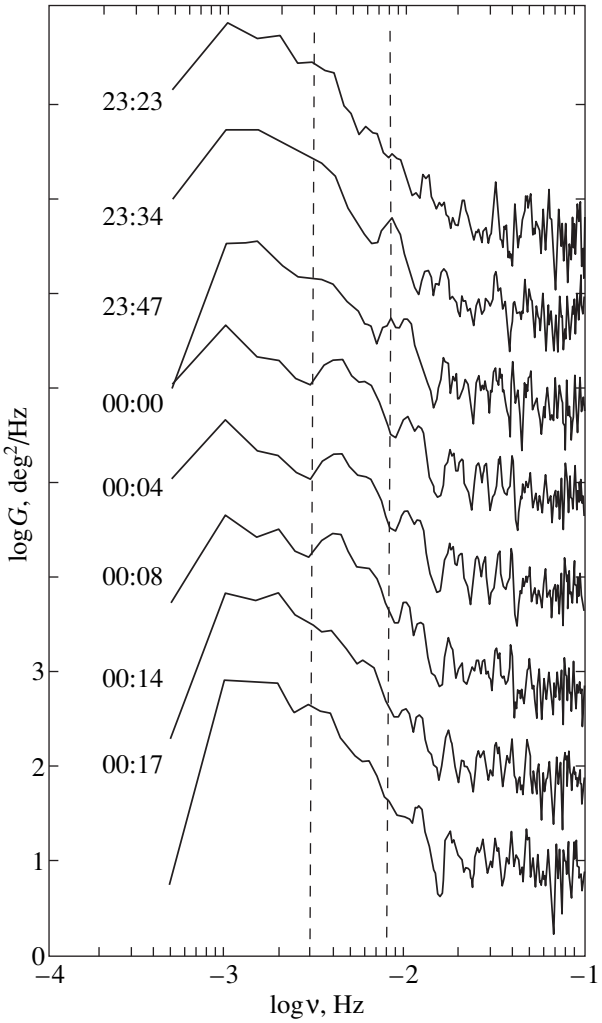

Fig. 2. Same as Fig. 1 for a different measurement interval.

where the fluctuation frequencies $\nu_{min} \approx 1$ mHz and $\nu_{max} \approx 10$ mHz are determined by the interval finiteness and the receiving-equipment noise, respectively;

(b) the spectral densities in the line center at the fundamental frequency of the quasi-harmonic component $G(\nu_1)$ and at the second harmonic $G(\nu_2)$, where $\nu_2 \approx 2\nu_1$;

(c) the difference between the spectral density of the quasi-harmonic components and the spectral density of the background spectrum $G_0(\nu)$, which was fitted by a power law,

$$\Delta G_1 = G(\nu_1) - G_0(\nu_1), \quad \Delta G_2 = G(\nu_2) - G_0(\nu_2); \quad (3)$$

(d) the ratio of the spectral densities at the frequencies of the quasi-harmonic components to the spectral densities of the background spectrum

$$g_1^2 = \frac{G(\nu_1)}{G_0(\nu_1)}, \quad g_2^2 = \frac{G(\nu_2)}{G_0(\nu_2)}; \quad (4)$$

(e) the ratio of the spectral densities at the frequencies of the quasi-harmonic components to the FRF variance

$$\xi_1^2 = \frac{G(\nu_1)}{\sigma_\psi^2}, \quad \xi_2^2 = \frac{G(\nu_2)}{\sigma_\psi^2}; \quad (5)$$

(f) the ratio of the differential spectral densities of the quasi-harmonic components to the FRF variance

$$(\Delta\xi_1)^2 = \frac{\Delta G_1}{\sigma_\psi^2}, \quad (\Delta\xi_2)^2 = \frac{\Delta G_2}{\sigma_\psi^2}, \quad (6)$$

which characterize the intrinsic intensity of the quasi-harmonic components.

Apart from a qualitative analysis, we used the parameters (2)–(6) for a quantitative description of the spatial–temporal dynamics of the FRF quasi-harmonic components.

THE EVOLUTION OF QUASI-HARMONIC COMPONENTS

Figures 1 and 2, which were constructed from the measurements at the Canberra station on January 7, 1983 (the impact parameter R of the line of sight was $5.6R_0$), give an idea of a typical temporal evolution of quasi-harmonic components. Figure 1 shows spectra for the observing intervals between 22:28 and 23:27 UT. The spectra in this figure (such as those in Figs. 2–4) are shown on a double logarithmic scale one under another from top to bottom, with the neighboring spectra being displaced along the y axis by one order of magnitude. Numerical values on the vertical axis refer to the bottom spectrum. The dashed lines correspond to the fluctuation frequencies of the fundamental component ν_1 and the second harmonic ν_2. The quasi-periodic component at the fundamental frequency $\nu_1 = 4$ mHz appears in the first interval. Its excess over the background power law $G_0(\nu)$ is characterized by $g_1 = 2.2$ and $\xi_1 = 8.05$. These coefficients increase to $g_1 = 3.8$ and $\xi_1 = 10.87$ at 22:41 UT. Subsequently, the quasi-harmonic component monotonically declines. At 22:53 UT, when the quasi-harmonic component completely disappears, the FRF time spectrum regains its original shape. The lifetime of the quasi-harmonic component, i.e., the time interval between its appearance and disappearance, is 56 min.

The quasi-harmonic component reappears at 23:34 UT (Fig. 2). The two successive spectra for the intervals beginning at 23:39 and 23:47 UT exhibit the second harmonic at $\nu = \nu_2 \approx 8$ mHz. The component at the fundamental frequency is enhanced in the next three spectra with $g_1 = 3.3$–3.8 and $\xi_1 = 10$–13. The FRF time spectrum again becomes a purely power-law one starting at 00:17 UT.

In general, the spectral density of quasi-harmonic components can be described by a fairly broad resonance curve with a line equivalent width $\Delta\nu \approx (0.5\text{–}1.3)\nu_{1,2}$. During a long continuous series of observations at the Canberra, quasi-harmonic components were present for 3 h, which accounts for 30% of the total duration of the series. In this case, the typical duration of the continuous presence of quasi-harmonic fluctuations was 50–60 min. Similar estimates were obtained for all the analyzed series of observations carried out at the three ground-based stations.

THE TYPES OF FRF SPECTRA

An in-depth analysis of the FRF spectra with quasi-harmonic components has revealed three types of spectra:

(1) those with the fundamental component alone;

(2) those with the second harmonic alone;

(3) those with both the fundamental and second harmonics.

The latter type of spectrum, which may be called a two-component one, is characterized by the simultaneous presence of two "resonance" perturbations against the background of a power law. Examples of such spectra at various heliocentric distances R are shown in Fig. 3. The dashed lines correspond to the fluctuation frequencies of the fundamental component ν_1 and the second harmonic ν_2.

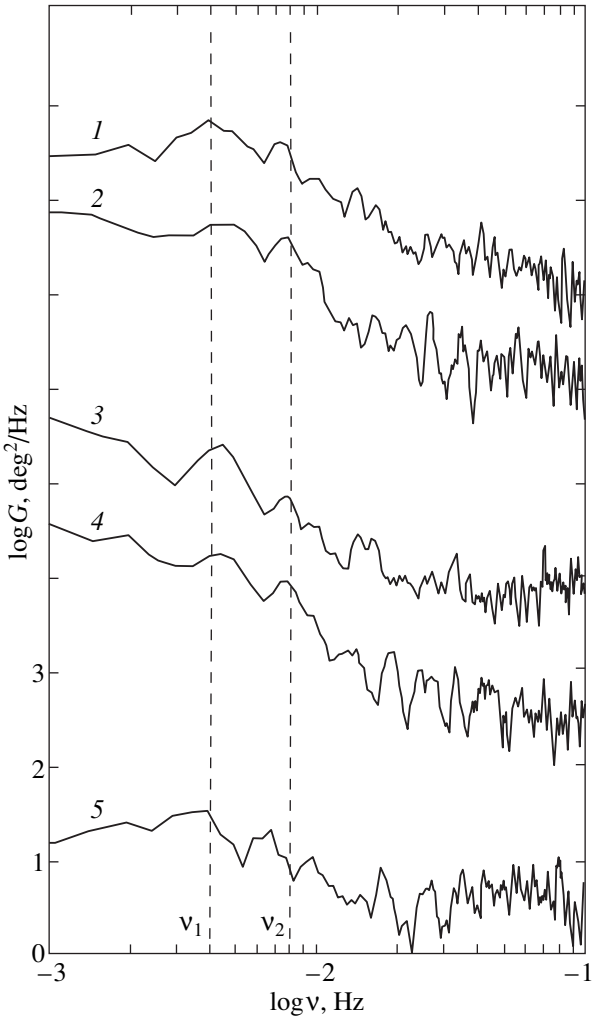

Fig. 3. FRF time spectra. Curves *1* and *2* were constructed from the simultaneous observations at the Goldstone (curve *1*) and Canberra (curve *2*) stations on January 9, 1983; the impact parameter is $R = 3.87R_\odot$. Curves *3* and *4* were constructed from the simultaneous observations at the same stations on January 7, 1983; $R = 5.6R_\odot$. Curve *5* is for January 10, 1983, the Madrid station; $R = 7.3R_\odot$.

Only one quasi-harmonic component at the fundamental frequency ν_1 or at the second harmonic ν_2 is present in spectra of the other two types. Examples of these types of spectrum are shown in Fig. 4. Two spectra (curves *1*, *2*) clearly exhibit a quasi-harmonic component at the fundamental frequency $\nu_1 = 4$ mHz. These spectra were computed from the simultaneous measurements at the Canberra and Goldstone stations. A comparison shows that the two spectra are virtually identical. Three spectra in Fig. 4 (curves *3*, *4*, *5*) contain a quasi-harmonic component only at the second harmonic $\nu_2 \approx 2\nu_1$. It should be noted that the second har-

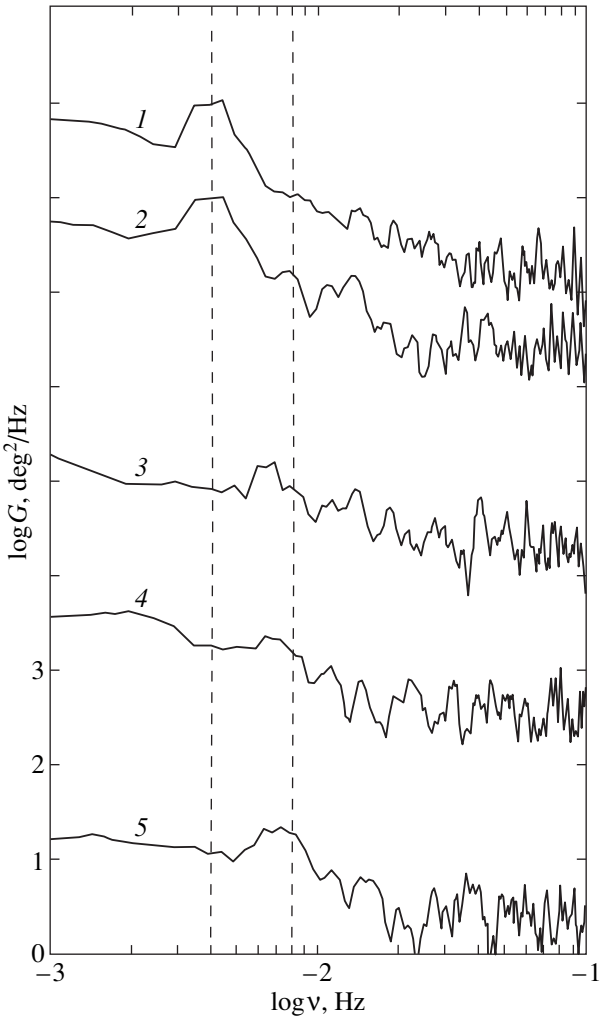

Fig. 4. FRF time spectra. Curves *1* and *2* were constructed from the simultaneous observations at the Goldstone and Canberra stations on January 9, 1983; $R = 4.1R_\odot$. Curve *3* is for January 10, 1983, Canberra; $R = 5.07R_\odot$. Curve *4* is for January 10, 1983, Goldstone; $R = 8.76R_\odot$. Curve *5* is for January 6, 1983, Canberra; $R = 11.18R_\odot$.

monic was observed at various heliocentric distances, including relatively large ones, $R > 11R_\odot$.

TEMPORAL AND RADIAL VARIATIONS OF FRF SPECTRA

Figure 5 shows variations in FRF spectral parameters during the session of simultaneous observations at the Canberra and Goldstone stations on January 7, 1983, in a narrow range of heliocentric distances, $5.65R_\odot > R > 5.4R_\odot$. For a better comparison of the data from the two stations, we introduced a small time shift (ΔT = 100 s) between them, which corresponds to the relative delay of spectral features. Figure 5a shows temporal variations for the rms values σ_ψ of the FRFs. We see that the FRF intensity can vary significantly on a time scale of the order of several minutes. Figure 5b

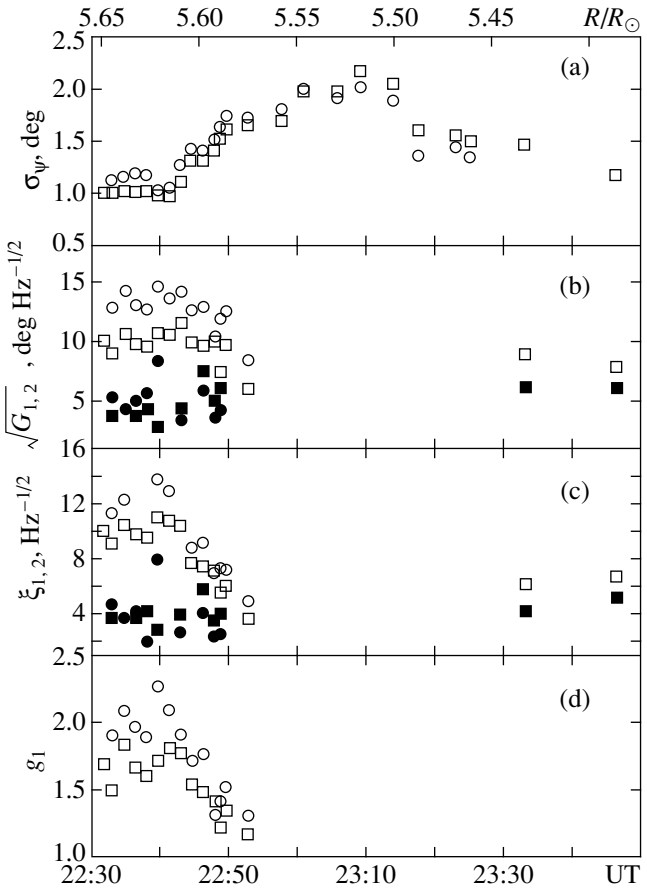

Fig. 5. Temporal evolution of the FRF spectral parameters as inferred from the simultaneous observations in Canberra (squares) and Goldstone (circles) on January 7, 1983.

shows the time dependence for $\sqrt{G(\nu_1)}$ (open symbols) and $\sqrt{G(\nu_2)}$ (filled symbols), which characterize the absolute fluctuation level at the fundamental frequency and at the second harmonic, respectively. The lack of data after 22:53 UT reflects the fact that no quasi-harmonic component was observed during this period. Figure 5c shows $\xi_{1,2}$; i.e., the quantities $\sqrt{G(\nu_1)}$ and $\sqrt{G(\nu_2)}$ normalized to the rms values σ_ψ of the FRFs. Finally, Fig. 5d show similar data for the coefficient g_1 (4), i.e., for the relative excess of the observed spectral density at the fundamental frequency over the spectral density expected for a purely power-law fit to the FRF spectrum. It follows from Figs. 5b–5d that $\sqrt{G_1}$, ξ_1, and g_1 can also undergo large variations on time scales of the order of several minutes. The typical values of g_1 for the data of Fig. 5 are 1.5–2.3, which correspond to a relative power excess $2.5 < g_1^2 < 5.3$.

A similar set of parameters is shown in Fig. 6 for a different series of measurements on January 9, 1983. The line of sight during this series passed slightly closer to the Sun, $4.4R_\odot > R > 3.8R_\odot$. Figures 6a and 6b

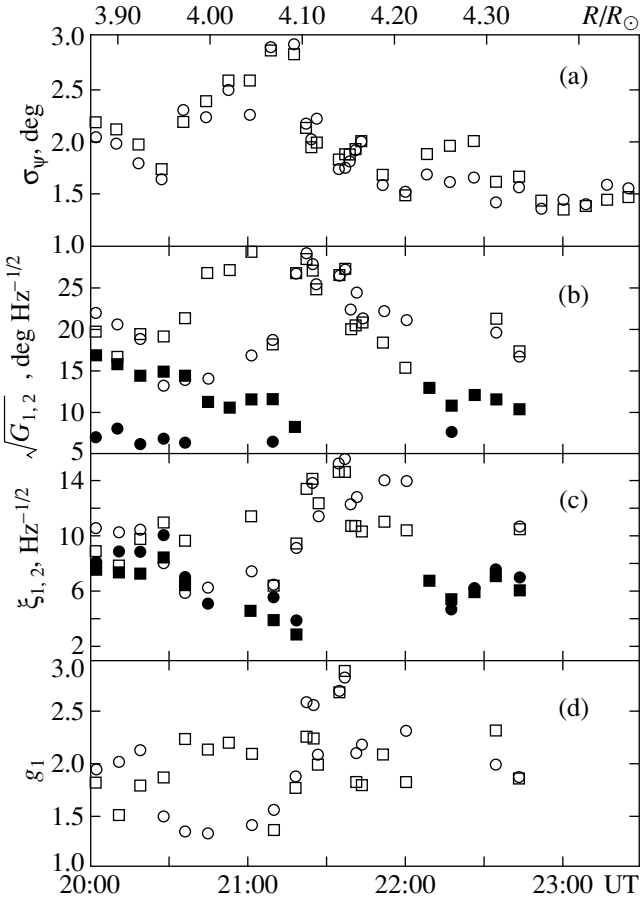

Fig. 6. Same as Fig. 5 for the simultaneous observations in Canbera and Goldstone on January 9, 1983.

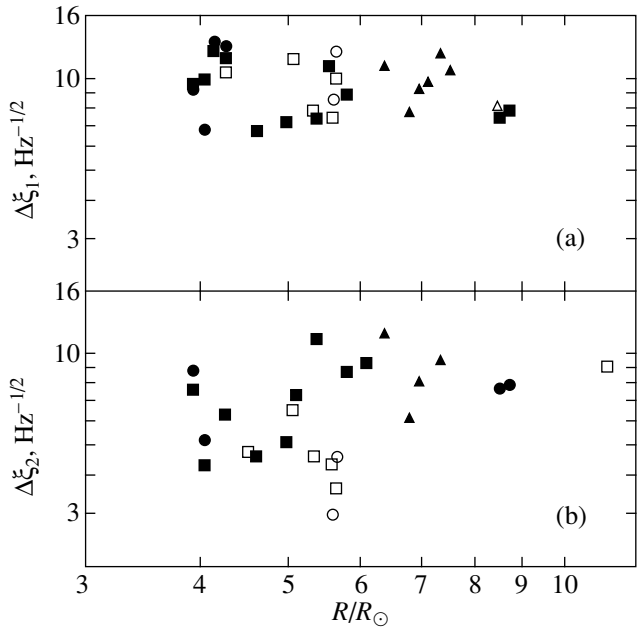

Fig. 7. Ratio of the spectral density of the quasi-harmonic component to the background FRF intensity versus impact parameter R: (a) fundamental component; and (b) second harmonic. The Goldstone, Canberra, and Madrid data are represented by circles, squares, and triangles, respectively. The open and filled symbols indicate the data obtained when the spacecraft went behind the solar corona and emerged.

clearly show a tendency for the absolute values of σ_ψ and $\sqrt{G_1}$ to decrease as the line of sight recedes from the Sun. In this case, however, we see that all quantities in Fig. 6 have a local maximum between 21:20 and 22:00 UT. Since there is no tendency for the relative quantities ξ_1 (Fig. 6c) and g_1 (Fig. 6d) to decrease with increasing heliocentric distance, using these parameters seems convenient when studying the evolution of quasi-harmonic FRFs. In Fig. 7, $\Delta\xi_{1,2} = (\Delta G_{1,2}/\sigma_\psi^2)^{1/2}$ are plotted against heliocentric distance R. The typical scatter of values for $\Delta\xi_1$ (Fig. 7a) does not exceed 20% of the mean, which, as we see from the figure, shows no tendency to vary with distance. We can therefore assert that $\Delta\xi_1$, within the error limits, does not depend on R, i.e., the intensity of quasi-periodic FRFs $G(\nu_1)$ and the intensity of background FRFs $\Delta G_0(\nu_1)$ at the fundamental frequency have the same dependence on R. The scatter of points in Fig. 7b referring to the FRFs at the second harmonic exceeds appreciably their scatter for the fundamental frequency, as we see from a comparison with Fig. 7a. The intensity of quasi-harmonic fluctuations at the second harmonic therefore has a radial dependence which also matches the radial dependence of the background FRF intensity.

THE POSSIBLE NATURE OF QUASI-PERIODIC FRFS

As we see from the above results, FRFs with a broad power-law power spectrum are observed in the inner regions of the solar wind. During some measurement sessions, quasi-periodic fluctuations with a fundamental period of about 4–5 min (the corresponding frequency is $\nu_1 = 4$ mHz) are seen against the background of a power-law spectrum. The fact that the radial dependences of the amplitudes of quasi-periodic and background fluctuations are identical suggests that they have the same physical nature. As Andreev *et al.* (1997a) showed, the FRFs are produced by Alfvén waves propagating freely, i.e., without substantial absorption through linear or nonlinear processes, away from the Sun. In this interpretation, the background FRF spectrum is determined by an ensemble of Alfvén waves with random phases generated under the conditions of developed turbulence, while the quasi-periodic fluctuations are attributable to isolated trains of quasi-monochromatic Alfvén waves. As follows from the above data, the typical length of an individual train is ~10 oscillation periods. It follows from our estimates of $\Delta\xi_1^2 = \Delta G(\nu_1)/\sigma_\psi^2$ (Fig. 7) that the level of the fluctua-

tions associated with isolated trains is comparable to the spectrum-integrated level of the background fluctuations. This circumstance, as well as the nonstationary nature of the trains at their repeating frequency, leads us to conclude that the frequency of the quasi-periodic fluctuations is similar to the characteristic power-containing frequency in the Alfvén-wave spectrum. Having analyzed the background FRFs, Andreev *et al.* (1997a) estimated the energy flux densities of Alfvén waves at the corona base, $H_a \geq 3 \times 10^4$ erg cm^{-2} s^{-1}. It follows from the above values of $\Delta G(\nu_1)/\sigma_\psi^2$ (Fig. 7) that the wave flux density in the quasi-periodic component at ν_1 is of the same order of magnitude.

Let us consider the conditions under which isolated Alfvén trains can show up against the background of the FRFs attributable to turbulent magnetic-field fluctuations. Assume that the magnetic-field fluctuations responsible for the background FRFs are associated with an ensemble of Alfvén waves with random phases propagating away from the Sun. In this case, the spatiotemporal fluctuation spectrum for the line-of-sight component of magnetic-field perturbations is (Andreev *et al.* 1997a)

$$\begin{aligned}&\langle \delta\mathbf{B}_{s,\mathbf{k},\omega}\delta\mathbf{B}^*_{s,\mathbf{q},\Omega}\rangle\\ &= k_y^2 k_\perp^{-2}\langle \delta B_k^2\rangle \delta(\omega-\Omega)\delta(\mathbf{k}-\mathbf{q})\delta(\omega-\mathbf{k}_\parallel(\mathbf{v}_a+\mathbf{v})),\end{aligned} \tag{7}$$

where ω, Ω, $\mathbf{q}$, and $\mathbf{k}$ are the frequencies and wave vectors of the Alfvén waves; $\langle \delta B_k^2\rangle$ is the trace of the spectral matrix $\langle \delta B_{k,ij}^2\rangle$; $\mathbf{v}$ and $\mathbf{v}_a$ are the solar-wind and Alfvén velocities; $\mathbf{k}_\parallel$ and $\mathbf{k}_\perp$ are the longitudinal and transverse (to the regular magnetic field) components of $\mathbf{k}$; k_y is the component of $\mathbf{k}$ perpendicular to the line of sight and to the regular magnetic field, which below is assumed to be radial: the polarization factor $k_y^2 k_\perp^{-2}$ identifies the line-of-sight component of $\delta\mathbf{B}$; * denotes a complex conjugate quantity. We choose the coordinate system in such a way that the *OZ* axis coincides with the line of sight and assume that the spatial spectrum $\langle \delta B_k^2\rangle$ follows a power law:

$$\begin{aligned}\langle \delta B_k^2\rangle &= C(\zeta^2 k_\parallel^2 + k_\perp^2)^{-\alpha/2};\\ L_T^{-1} &< (\zeta^2 k_\parallel^2 + k_\perp^2)^{1/2} < l_m^{-1},\end{aligned} \tag{8}$$

where C is the structural constant, which can be determined from the condition of normalization of the spectrum (8) to the variance of magnetic-field fluctuations; $\zeta > 1$ is the irregularity anisotropy parameter.

For the subsequent estimates, we take the exponent $\alpha = 3$, typical of our data. Based on (1), (7), and (8) and assuming that $v < v_a$, we can obtain (Andreev *et al.*, 1997a) the following estimate for the spectral density of turbulent FRFs:

$$G_T(\nu) = A^2 N_0^2(R) v_a(R) R(16\pi\nu^2\zeta\ln(L_T/l_m))^{-1}, \tag{9}$$

where σ_B^2 is the variance of the magnetic-field fluctuations; the values of N_0, v_a, and σ_B^2 are taken at the impact point of the line of sight located at heliocentric distance R; l_m and L_T are the inner and outer turbulence scale lengths; and A is the Alfvén-wave amplitude. When calculating $G_T(\nu)$ (9), we took a spherically symmetric model of the medium with $N_0 \sim R^{-4}$ and $\sigma_B^2 \sim N_0^{1/2}$; the factor R corresponds to the thickness of an effectively modulating layer. Note that the mean Faraday-rotation angle for this model is zero.

Let us now consider the quasi-periodic FRFs associated with a isolated quasi-harmonic Alfvén wave packet (train) bounded in space and time. We specify the wave packet in the form

$$\begin{aligned}&\delta\mathbf{B}(\mathbf{r}, t)\\ &= \frac{1}{2}[\mathbf{k}_1\mathbf{n}]k_{1\perp}^{-1}\delta B_0 \exp(-i2\pi\nu_1 + i\mathbf{k}_1\mathbf{r}) + \text{c.c.};\\ &0 < x < L_x, \quad 0 < y, z < L_\perp,\\ &2\pi\nu_1 = \mathbf{k}_{1x}\cdot\mathbf{v}_a, \quad k_{1x}L_x \gg 1,\end{aligned} \tag{10}$$

where $\mathbf{n}$ is the unit vector along the regular magnetic field, and c.c. means complex conjugation; the wave packet is assumed to be localized near the impact point with $\mathbf{n} \parallel OX$. When calculating the FRF spectral density $G_n(\nu)$ associated with the wave packet, we first set up the FRF spaciotemporal correlation function (1) and then determine its time Fourier spectrum by taking into account the fact that the wave packet is spatially bounded. As a result, we obtain

$$\begin{aligned}G_n(\nu) &= \frac{1}{2\pi}A^2 N_0^2 \delta B_0^2 L_\perp^2 \frac{L_x}{v_a} F_z F_x(\nu)\frac{k_{1y}^2}{k_{1y}^2 + k_{1z}^2},\\ F_z &= \sin^2\frac{k_{1z}L_\perp}{(k_{1z}^2 L_\perp)^{-2}},\\ F_x(\nu) &= v_a \sin\left[\pi(\nu-\nu_1)\frac{L_x}{v_a}\right][\pi(\nu-\nu_1)L_x]^{-1}.\end{aligned} \tag{11}$$

The spectral density at the packet carrier frequency $\nu = \nu_1$ can be determined from (11):

$$G_n(\nu_1) = \frac{1}{2\pi}A^2 N_0^2 \delta B_0^2 L_\perp^2 \frac{L_x}{v_a} F_z. \tag{12}$$

Let us now compare the levels of the FRFs associated with the wave packet $G_n(\nu_1)$ (12) and with the background turbulence $G_T(\nu)$ (9):

$$\eta = \frac{G_n(\nu_1)}{G_T(\nu)} = 8L_\perp^2(\lambda_\perp R)^{-1} F_z \frac{T_0}{T_1}\delta B_0^2 \ln\left(\frac{L_T}{l_m}\right)\sigma_B^{-2}, \tag{13}$$

where $\lambda_\perp$ is the characteristic transverse wavelength of the turbulent fluctuations; $\lambda_\perp = \frac{v_a}{\nu_1 \zeta}$, $T_0 = \frac{L_x}{v_a}$ is the packet duration; and $T_1 = \nu_1^{-1}$ is the Alfvén-wave period. If we assume that the packet-oscillation amplitude does not differ much from the rms value of the turbulent magnetic-field fluctuations, i.e., $\delta B_0^2 \sim \sigma_B^2 \ln^{-1}\frac{L_T}{l_m}$, then it follows from (13) that

$$\begin{aligned} \eta &\sim 8L_\perp^2(\lambda_\perp R)^{-1}\frac{T_0}{T_1} \quad \text{for} \quad k_{1z}L_\perp < 1, \\ \eta &\sim 8(k_{1z}^2\lambda_\perp R)^{-1}\frac{T_0}{T_1} \quad \text{for} \quad k_{1z}L_\perp > 1. \end{aligned} \tag{14}$$

The contribution of the wave packet to the FRFs will exceed the contribution of background turbulence if $\eta > 1$. Such conditions are realized at sufficiently small projections of the packet wave vector onto the line of sight and at sufficiently large packet sizes:

$$\begin{aligned} T_0 L_\perp^2 &> T_1 \lambda_\perp R \quad \text{for} \quad k_{1z}L_\perp < 1, \\ T_0 L_\perp^2 &> T_1 \lambda_\perp R \quad \text{for} \quad k_{1z}L_\perp > 1. \end{aligned} \tag{15}$$

If we take $\zeta \approx 10$, $v_a \approx 6 \times 10^7$ cm s^{-1} (Andreev *et al.*, 1997a), $\lambda_\perp \approx 2 \times 10^9$ cm, and $R \approx 3 \times 10^{11}$ cm, then we obtain the following numerical estimate from (15) at $T_0 \approx 10T_1$:

$$\min(k_{1z}^{-1}, L_\perp) > 3 \times 10^9 \text{ cm}. \tag{16}$$

The estimate (16) shows that the line-of-sight component k_{1z} cannot exceed 3×10^9 cm^{-1} at any value of $k_{1z}L_\perp$. If the Alfvén perturbations are assumed to be generated mostly at the corona base, then, given that $k_{1z} = k_{zs}(R_\odot/R)$ because of the spherical symmetry of the medium, we obtain from (16) an estimate of the scale size for the initial perturbations generating Alfvén wave packets, $l_z > 10^9$ cm. This estimate corresponds to the scale sizes of the supergranulation chromospheric network [see p. 38 in Kaplan *et al.* (1977)]. Such a match between the scale sizes suggests that the observed wave packets are generated by nonstationary processes in anisotropic magnetic structures of the upper chromosphere and the transition layer. Note that k_{1y} may be arbitrary, in particular, $k_{1y} \gg k_{1z}$. In this case, it should be borne in mind that, because of the polarization factor in (11), the line-of-sight component of the packet magnetic field is nonzero if $k_{1y} \neq 0$ (at $k_{1z} \neq 0$) or $k_{1y} = k_{1z} = 0$. For wave packets satisfying the conditions (15) and (16), the magnetic-field perturbations lie predominantly in the plane of the solar equator, while the projection of the wave vector onto this plane is fairly small. The conditions (15) and (16) are not too stringent and may well be satisfied for actual conditions in the outer solar corona. The sporadic nature of the quasi-periodic FRFs most likely stems from the fact that only wave packets with the peculiar orientation of the wave vectors and magnetic-field perturbations noted above can be observed against the background of turbulent FRFs. Wave packets that do not satisfy (15) and (16) will not show up in FRF observations as individual events. Although the model outlined above is rough, it qualitatively illustrates the possibility of observing isolated Alfvén wave packets and allows quantitative requirements which the wave packets must meet to be formulated.

The emergence of quasi-periodic FRFs suggests that there are Alfvén waves with periods of about 4–5 min in the inner regions of the solar wind. These periods of isolated Alfvén trains roughly match the period of the well-known 5-min oscillations, which are observed near the photosphere. These oscillations are acoustic ones, and their characteristic frequency matches the cutoff frequency, which is determined by plasma temperature and gravitational acceleration [see p. 38 in Kaplan *et al.* (1977)]. Since periods of ~5 min are not physically characteristic of Alfvén waves, it seems quite natural to assume that the original source of Alfvén waves is associated with acoustic waves at the photospheric level. At the same time, the estimates by Chasheĭ and Shishov (1986) show that, when Alfvén waves are generated directly in the photospheric layers, the coronal Alfvén fluctuation level and the corresponding energy flux will be insignificant, $H_a \leq 10^2$ erg cm^{-2} s^{-1}. The source of the Alfvén waves passing to the corona, including quasi-periodic ones, is most likely located at the base of the transition layer separating the chromosphere and the corona, where the Alfvén waves are generated in a strongly turbulent mode by acoustic waves coming from deeper layers (Chasheĭ and Shishov, 1984). The energy flux of the Alfvén waves passing to the corona in this model for moderate magnetic fields in the generation zone ($B_0 \geq 2$ G) is $H_a \sim 10^5$ erg cm^{-2} s^{-1} (Chasheĭ and Shishov, 1984, 1986), in agreement with the estimates obtained by analyzing FRFs. Given the transparency of the quiet corona for Alfvén waves with periods ≥5 min (Chasheĭ and Shishov, 1984), the assumption that the Alfvén waves are generated at the base of the transition layer also qualitatively explains the sporadic emergence of isolated trains with periods of ~5 min against the background of a turbulent wave flux in the solar-wind acceleration region.

Taking into account the above estimates referring to the train geometry, we can assert that the 5-min Alfvén fluctuations in the generation zone and the corona have a broad spectrum by wave numbers.

Note that interpreting the quasi-periodic fluctuations at the second harmonic requires invoking more complex models for the following two reasons: first, the absorption of Alfvén waves with $\nu_2 = 2\nu_1$ in the inner corona is stronger than the absorption of waves with $\nu = \nu_1$ (Chasheĭ and Shishov, 1984), which makes it difficult for them to escape from the corona base into the outer layers; and, second, since the Alfvén spectrum is

stationary, the local generation of Alfvén waves with $\nu = \nu_2$ during nonlinear mergers of waves with $\nu = \nu_1$ also seems unlikely.

CONCLUSION

A spectral analysis of successively shifted intervals of the FRF records of radio signals from the Helios spacecraft shows that the statistical parameters and spectral composition of the FRFs can undergo significant variations on time scales of the order of several minutes. Applying a high-time-resolution technique reveals the sporadic presence of typical peaks in the FRF spectra at frequencies of 4 and/or 8 mHz, which correspond to quasi-harmonic fluctuations at the fundamental frequency and its second harmonics. Quasi-harmonic oscillations were detected in all series of measurements in 1983 at various heliocentric distances $R \geq 3.4R_\odot$. So far we have failed to detect quasi-periodic components at smaller distances $R < 3R_\odot$.

There are three types of spectra with quasi-periodic components. Spectra of the first type contain fluctuations only at the fundamental frequency $\nu_1 \approx \nu \approx 4$ mHz. Spectra of the second type are characterized by the presence of quasi-harmonic fluctuations only at frequency $\nu_2 \approx 2\nu_1$. Spectra of the third type simultaneously contain quasi-harmonic components at both frequencies ν_1 and ν_2.

As the main quantitative criterion for the presence of quasi-periodic components, we used the factor $g_{1,2}$, which characterizes the excess of the spectral density at $\nu = \nu_{1,2}$ over its background value calculated for a power-law fit to the FRF power spectrum. The values of $g_{1,2}$ in the analyzed measurement sessions generally lie in the range 2–8.

An analysis of observational data for the series of radio sounding experiments in 1983 shows that the spectral density of the quasi-periodic component at the fundamental frequency ν_1 decreases with increasing distance from the Sun in the same fashion as the spectral density in the FRF background spectrum. The same conclusion, though with a lesser degree of confidence, can also be reached for the spectral density at the second harmonic. The qualitative dynamics of the quasi-periodic component at ν_1 and its quantitative parameters can be explained in terms of the model with the simultaneous generation of quasi-periodic and background Alfvén perturbations at the base of the chromosphere–corona transition layer.

This paper provides the first evidence for the presence of Alfvén waves with periods of ~5 min in circumsolar plasma, i.e., outside the corona. Given the importance of such waves for the physics of circumsolar and coronal plasma, of indubitable interest is the study of quasi-periodic FRFs on the basis of more extensive observational data, including measurements at a different phase of the solar cycle and the sounding of regions at higher heliolatitudes, where the role of Alfvén waves is currently believed to be even more significant than that near the equatorial plane.

ACKNOWLEDGMENTS

This study was supported by the Russian Foundation for Basic Research (project nos. 97-02-16035 and 00-02-17665), the official research project within the framework of collaboration between the RFBR and DFG (Germany), and the State Science and Technology Program “Astronomy.”

REFERENCES

1. V. E. Andreev, M. K. Bird, A. I. Efimov, *et al.*, Astron. Zh. **74**, 263 (1997a) [Astron. Rep. **41**, 227 (1997a)].
2. V. E. Andreev, M. K. Bird, A. I. Efimov, *et al.*, Pis’ma Astron. Zh. **23**, 222 (1997b) [Astron. Lett. **23**, 194 (1997b)].
3. V. E. Andreev, A. I. Efimov, L. N. Samoznaev, and M. K. Bird, in *Solar Wind Eight*, Ed. by D. Winterhalter *et al.* (AIP, Woodbury, New York, 1996), AIP Conf. Proc., No. 382, 34 (1996).
4. I. V. Chasheĭ and V. I. Shishov, Astron. Zh. **61**, 474 (1984) [Sov. Astron. **28**, 279 (1984)].
5. I. V. Chasheĭ and V. I. Shishov, Astron. Zh. **63**, 542 (1986) [Sov. Astron. **30**, 322 (1986)].
6. P. Edenhofer, M. K. Bird, H. Volland, and J. V. Hollweg, Mitt. Astron. Ges. **50**, 42 (1980).
7. A. I. Efimov, I. V. Chasheĭ, V. I. Shishov, and M. K. Bird, Pis’ma Astron. Zh. **19**, 143 (1993) [Astron. Lett. **19**, 57 (1993)].
8. J. V. Hollweg, M. K. Bird, H. Volland, *et al.*, J. Geophys. Res. **87**, 1 (1982).
9. S. A. Kaplan, S. B. Pikel’ner, and V. N. Tsytovich, *Physics of the Solar Coronal Plasma* (Nauka, Moscow, 1977).
10. H. Volland, M. K. Bird, G. S. Levy, *et al.*, J. Geophys. **42**, 659 (1977).

Translated by V. Astakhov